AD_____

Award Number: W81XWH-07-1-0428

TITLE: Nanotechnology-Enabled Optical Molecular Imaging of Breast
Cancer

PRINCIPAL INVESTIGATOR: Rebekah Drezek, Ph.D.

CONTRACTING ORGANIZATION: Rice University
Houston, TX 77005

REPORT DATE: July 2008

TYPE OF REPORT: Annual

PREPARED FOR: U.S. Army Medical Research and Materiel Command
Fort Detrick, Maryland 21702-5012

DISTRIBUTION STATEMENT: Approved for Public Release;
Distribution Unlimited

REPORT DOCUMENTATION PAGE

Form Approved
OMB No. 0704-0188

Public reporting burden for this collection of information is estimated to average 1 hour per response, including the time for reviewing instructions, searching existing data sources, gathering and maintaining the data needed, and completing and reviewing this collection of information. Send comments regarding this burden estimate or any other aspect of this collection of information, including suggestions for reducing this burden to Department of Defense, Washington Headquarters Services, Directorate for Information Operations and Reports (0704-0188), 1215 Jefferson Davis Highway, Suite 1204, Arlington, VA 22202-4302. Respondents should be aware that notwithstanding any other provision of law, no person shall be subject to any penalty for failing to comply with a collection of information if it does not display a currently valid OMB control number. **PLEASE DO NOT RETURN YOUR FORM TO THE ABOVE ADDRESS.**

1. REPORT DATE	2. REPORT TYPE	3. DATES COVERED
14-07-2008	Annual	15 JUN 2007 - 14 JUN 2008

4. TITLE AND SUBTITLE

Nanotechnology-Enabled Optical Molecular Imaging of Breast Cancer

5a. CONTRACT NUMBER

5b. GRANT NUMBER
W81XWH-07-1-0428

5c. PROGRAM ELEMENT NUMBER

6. AUTHOR(S)

Rebekah Drezek, Ph.D.

Email: drezek@rice.edu

5d. PROJECT NUMBER

5e. TASK NUMBER

5f. WORK UNIT NUMBER

7. PERFORMING ORGANIZATION NAME(S) AND ADDRESS(ES)

Rice University
Houston, TX 77005

8. PERFORMING ORGANIZATION REPORT NUMBER

9. SPONSORING / MONITORING AGENCY NAME(S) AND ADDRESS(ES)
U.S. Army Medical Research and Materiel Command
Fort Detrick, Maryland 21702-5012

10. SPONSOR/MONITOR'S ACRONYM(S)

11. SPONSOR/MONITOR'S REPORT NUMBER(S)

12. DISTRIBUTION / AVAILABILITY STATEMENT
Approved for Public Release; Distribution Unlimited

13. SUPPLEMENTARY NOTES

14. ABSTRACT
This project focuses on development of nanotechnology-enabled optical molecular imaging technologies for applications in breast cancer diagnosis and monitoring of therapeutic response. The project consists of two major efforts: (1) optical instrumentation technology development and (2) development of complementary engineered nanomaterials for use in conjunction with the instrumentation created to provide molecular specificity. A particularly significant effort is underway to develop needle-compatible fiber optic probes to enable in vivo imaging of tumors with micron resolution in order to provide a new microscopic, high resolution imaging modality to complement the low resolution, macroscopic imaging modalities already in common clinical use. Nanoengineered materials including shaped and layered gold nanoparticles and cadmium-free luminescent dots targeted to molecular signatures of breast cancer are being developed with properties optimized for the specific optical imaging strategies created.

15. SUBJECT TERMS
nanotechnology, molecular imaging, optical imaging

16. SECURITY CLASSIFICATION OF:

a. REPORT	b. ABSTRACT	c. THIS PAGE	17. LIMITATION OF ABSTRACT	18. NUMBER OF PAGES	19a. NAME OF RESPONSIBLE PERSON USAMRMC
U	U	U	UU	93	19b. TELEPHONE NUMBER *(include area code)*

Standard Form 298 (Rev. 8-98)
Prescribed by ANSI Std. Z39.18

Table of Contents

Introduction

There is a critical need to develop new imaging technologies which bridge the gap between our rapidly developing fundamental molecular understanding of breast carcinogenesis and our ability to rationally harness this understanding to develop more effective diagnostic and treatment strategies. Bridging that gap requires developing new tools which can rapidly detect, diagnose, and at times, intervene in the disease process based on recognition of specific molecular signatures of breast cancer *in vivo*. In this project, we focus on the development of miniaturized photonics-based imaging technologies (SOW, Project 1) and complementary nanoscale molecular-targeted imaging agents for detection and monitoring applications (SOW, Project 2 and Project 3) in order to provide a new approach to molecular imaging of breast cancer. Medical imaging plays a prominent role in all aspects of the screening, detection, and management of breast cancer today. A variety of imaging methods including screening and diagnostic x-ray mammography and resonance imaging (MRI) are currently used to evaluate and monitor breast lesions. Although existing imaging technologies provide a useful approach to delineating the extent of tumors, these methods offer only low resolution, non-specific issues of tissue and cannot provide a detailed picture of the molecular profile of a tumor. In addition, techniques such as x-ray imaging and MRI are not able to detect small early cancers or pre-cancerous breast lesions and are difficult to use in settings such as the operating room where near real-time dynamic images are required. Thus, there is a substantial clinical need for novel imaging methods for the detection and monitoring of breast cancers which offer improved sensitivity, specificity, portability, and cost-effectiveness. In this project we develop portable optical technologies which promise high resolution, noninvasive functional imaging of tissue at competitive costs. Optical approaches can detect a broad range of morphological, biochemical, and architectural tissue features directly relevant to characterizing breast lesions including sub-cellular physical parameters such as nuclear size and nuclear to cytoplasm (N/C) ratios and biochemical indicators such as hemoglobin concentration, metabolic rate, and collagen cross-linking levels. To make these technologies even more powerful we expand the current capabilities of photonics-based imaging approaches with the additional capacity to quantitatively and dynamically detect molecular markers of breast cancer *in vivo* without tissue removal (SOW, Project 2). Developing the optical molecular imaging tools and agents for breast cancer which will allow us to accomplish this goal is the focus of this project.

Progress Report Body

This progress report is arranged to follow the Statement of Work (SOW). The Statement of Work is divided into three sub-projects and a series of tasks. We describe efforts during months 1-12 of the award on each of the three sub-projects below.

Project 1:   Needle-Based Biopsy System Development

In the section which follows we provide background on our motivation for developing a needle-compatible fiber optic system (Figure 1.0) for breast cancer diagnostic and monitoring applications, information regarding the optical techniques and image analysis strategies we will use, and a description of how our system would interact with the technologies which are standard of care today. We then present our results to date. As described in the Statement of Work, Year 1 plans focused on design of this system and beginning initial construction. It was expected that the first system would be completed approximately 20 months after the design phase. We are
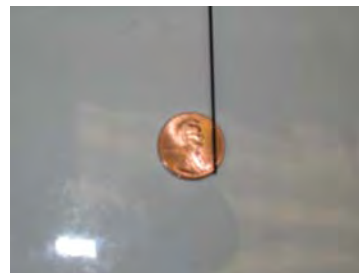

Figure 1.0. First generation needle compatible fiber probe (next to penny to demonstrate size). Imaging resolution using the system has been experimentally demonstrated to be < 10 um.

significantly ahead of schedule on this project. In this section we present initial data for the system which is already providing micron resolution imaging capability through a needle probe. As we are ahead of schedule of Project 1, in Year 2 we will seek permission to modify our program of work to include much more extensive clinical evaluation of this instrument than originally anticipated. Plans which note tissue studies and other clinical efforts below will only proceed presuming these modifications to our SOW are accepted and regulatory paperwork is approved.

Background

The survival rate of cancer increases significantly with earlier diagnosis; the 5-year survival rate of breast cancer, for example, is greater than 90% when it is diagnosed and treated while still localized but drops to 25% after metastasis. However, an accurate diagnosis often requires an invasive procedure that is sufficiently unpleasant that sometimes patients and even doctors are reluctant to undergo it. This coupled to the fact that early signs of cancer are frequently difficult to distinguish from benign lesions by routine examination lead to delayed diagnosis that cost lives. As a result, new techniques in cancer diagnosis have traditionally sought a balance between accuracy and invasiveness. Nevertheless, the gold standard for cancer diagnosis remains the biopsy slides read by a trained pathologist. Not surprisingly, this is also the most invasive diagnostic procedure available.

Recent advances in miniaturized optics and electronic systems have opened the way to a new kind of cancer diagnosis: optical biopsy. Optical biopsy permits a direct examination of the tissue of suspicion without any invasive tissue removal while maintaining much of the sensitivity and specificity that make biopsy reading the gold standard for cancer diagnosis. Such

advancement is possible because the diagnosis of cancer from surgical biopsy focuses on a few key observations: the greatly enlarged nucleus of uncontrollably dividing cells and the visibly disrupted tissue morphology of unregulated cell expansion. Although the miniature optics used for optical biopsy sacrifices some resolving power for smaller size, they retain sufficient resolution and field of view to image the key features that make surgical biopsy work. This technique therefore makes the gold standard of cancer diagnosis much more accessible and much less unpleasant.

On the other hand, research into alternative methods of cancer diagnosis that rely on spectroscopic information has also progressed at a robust pace. Recent publications have reported significant differences in the fluorescence and reflectance spectra of normal versus dysplastic tissue. Although the analysis of these spectra require the aid of computers and spectroscopy has not proven itself equal to biopsy, the ability to probe chemical and structural information that are not available for visualization offers an entirely new set of diagnostic tools that can at the very least compliment the visual information from biopsies.

Starting from the development of physical imaging hardware that can produce images of sufficient quality for optical biopsy, efforts will be directed to the subsequent development of a complimentary software system that can at the minimum accentuate the key visual characteristics that indicate cancer; every effort will be made to move a step further from simply enhancing the images to automated analysis. The whole system will then be packaged for clinical testing. After the optical biopsy system has been largely completed, the second major thrust of the project will involve the integration of optical biopsy information with spectroscopy information. Ultimately, this project hopes to produce an automated system that uses both optical biopsy and spectroscopy to diagnose breast cancer. It will have sensitivity, specificity, and minimal invasiveness that surpass or rival the diagnostic tools available to doctors today.

To that end, the following tasks will be accomplished in sequence:

Development and testing of an optical biopsy system for breast cancer applications with digital image enhancement and analysis

This part of the project focuses on the development and testing of the optical biopsy system. Appropriate hardware will be selected to test the feasibility of the physical system to generate an image of sufficient quality for the software to process. Specifically, the hardware development will be considered a success if (1) the system clearly demonstrates sufficient resolution to image cellular features relevant to cancer diagnosis and (2) there is clear evidence that the images contain information about those relevant cell feature (though it need not be clear enough for a diagnosis as is). After the hardware has been successfully developed, a software system will be designed that can extract relevant information from the hardware images to generate a pseudo image

useful to pathologists for diagnosis and to make an automated diagnosis based on that information.   Specifically, the software development will be considered a success if (1) the relevant cellular information can be extracted from the hardware image and (2) the information can be used to generate a useful pseudo image to accentuate the relevant features.   If an automated diagnostic algorithm can be developed, it will be considered a major success.   This stage will be deemed successful if the two specific criteria for both hardware and software are met.

Development and testing of an optical biopsy system for use with molecular imaging agents in either reflectance or fluorescence mode (to be completed in conjunction with Project 2)

This part of the project focuses on the development and testing of an optical biopsy system specifically designed to take advantage of contrast agents for improved imaging capability.   There are two distinct areas where efforts will be focused.   One area of research will focus on the development of a contrast agent suitable for the imaging of breast tissue.   Two specific goals have been set: (1) the contrast agent can be used to improve the visibility of key cellular features in breast tissue including but not limited to the cell membrane and the nucleus; (2) the contrast agent can specifically target cancer cells and distinguish them from normal cells by color or other means.   If either goal can be met in reflectance or fluorescence mode, this area would be considered a success. The other area compliments the first by focusing on the development of a hardware system that can deliver contrast agents directly to the imaging site.   There are also two goals specific to this area: (1) the optical biopsy system has a mechanism to deliver precise amounts of contrast agents directly to the imaging site without adversely affecting the imaging capability of the system; (2) if necessary, the optical biopsy system has a mechanism to remove either unbound or excess contrast agent from the imaging site without inflicting additional pain and suffering on the patient.   The first goal is considered the more important and feasible; however, if the situation arises where the second goal becomes necessary, all efforts will be spend to achieve it.

Evaluation: Investigation of combining structural information with spectroscopic information for improved cancer diagnosis

Although it has not yet show sufficient quality to rival the gold standard of biopsy, spectroscopy has been shown to distinguish normal and dysplastic cells based on non-visual information in many experiments.   Efforts at this stage will focus first on validating the diagnostic value of spectroscopy in breast tissue.   Should the validation be positive, structural information such as the nuclear-to-cytoplasmic ratio will be manually extracted from a tissue sample that will also be probed spectroscopically.   A statistical software algorithm will be developed to combine the structural and

spectroscopic information, and its sensitivity and specificity will be evaluated.   A suitable spectroscopic component will be added to the optical biopsy system and integrated in such a way that the data from both can be acquired and analyzed in the same setting. Specifically, the integrated system will be considered a success if (1) the spectroscopic component of the system can acquire spectroscopic information from breast tissue and distinguish them with sensitivity and specificity comparable to published results and (2) the final integrated system can stage breast cancer with higher sensitivity and specificity than is possible with either method in isolation.

Background on biopsy and fiber optical imaging

Excisional biopsy, core needle biopsy, and fine needle aspiration biopsy

To this day, biopsy slides read by a pathologist remain the gold standard for cancer diagnosis. The most informative type of biopsy is excisional biopsy.   During this procedure, the piece of tissue containing the entire suspect lesion is removed.   The removed tissue is then cut into very thin slices, stained with dyes, and examined under the microscope by a pathologist [1].   The pathologist looks for structural and morphological abnormalities when assessing whether cancer is present in the tissue.   The most prominent structural feature associated with cancerous cells is an enlarged cell nucleus, which may occupy as much as 80% of the total cell area when observed under the microscope.   In addition, the rapid and unregulated division of cancer cells creates distinctive morphological characteristics in a cancerous lesion that separate it from normal tissue.   Although a single cell could potentially be observed during cell division, a cancerous lesion will contain many more dividing cells than normal tissue.   Furthermore, cancerous lesions will show a clear breakdown in cell organization because the regulators that controls cell organization in normal tissue do not correctly affects cancer cells. (Fig. 1.1) These structural and morphological changes are the primary symptoms that pathologists use to diagnose cancer in a biopsied tissue.
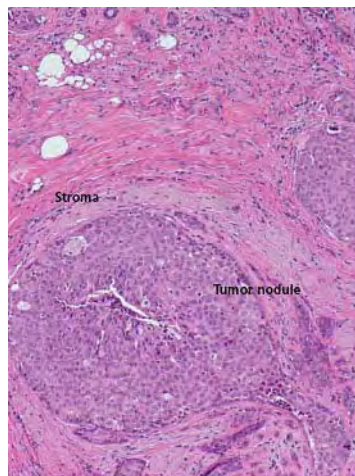

Figure 1.1 [2]: Dye stained breast tissue slide showing cancer cells (blue-purple, labeled "Tumor nodule") surrounded

by normal cells (pink, labeled "Stroma").   The cancer cells show a high density of nucleus stained blue-purple.   They are also rounded and crowded.   The normal cells are elongated, striated, and have much lower nucleus visibility.

Besides being the gold standard for cancer diagnosis, excisional biopsy is also the primary method for monitoring the surgical margin, the region of normal tissue surrounding the cancerous lesion in the removed sample, in breast conservation surgery.   Primarily a gauge for the success of breast cancer resection surgery, a clear margin means there is no cancerous tissue bordering the edges of the tissue sample, indicating a high probability that the entire cancerous lesion has been removed.   The traditional method for mapping the surgical margins in an excisional biopsy sample is the paraffin-embedded histology method; this requires a lengthy preparation in which the tissue is embedded in paraffin and sectioned into thin slices with a microtome. The slices are then examined for clear surgical margins [3].

In order to better visualize the various structures in a tissue sample, the tissue is normally stained with dyes that add artificial color to different structures.   The most common dyes used are hematoxylin and eosin (H&E).   The hematoxylin stains the nucleic acid-rich regions of the cells, primarily the nucleus, blue-purple and the protein-rich regions, mainly the cytoplasm and extracellular matrix, pink [4].   It is uncommon for a diagnosis to be based on raw tissue.

Despite the powerful diagnostic value of the excisional biopsy, its high cost compels a simpler and cheaper alternative in cases where only the diagnosis of disease, not the mapping of surgical margins, is necessary.   The magnitude of the operation to remove a piece of tissue containing the entire suspect lesion ranges from a minor to a major surgery.   The pain and suffering of the patient, the time and medical resourced consumed, and the monetary cost necessary for such procedures are imposed on patients and doctors alike.   Because the diagnosis of cancer is based on cellular and morphological features present even in a limited sample, it is frequently sufficient to remove only a small piece of suspect lesion for examination by a pathologist.

One of the most widely used alternatives to excisional biopsy is core needle biopsy. Although needle core biopsy had been performed on other organ sites, the procedure for successfully applying it to breast cancer diagnosis was first established by Parker et al. in 1990 [5].   In that study, commercial core biopsy needles ranging in size from 14-gauge to 18-gauge were used to remove tissue samples from suspect lesions identified by mammography. The mammography system also served as the stereotactic mapping system for the guided core biopsies.   The biopsied tissues were prepared for standard pathological evaluation.   A total of 103 patients underwent stereotactic breast core biopsy followed by surgical biopsy at the same site.   In all, the histology results from the core biopsies agreed with that of the surgical biopsies in 89 of the 103 cases (87% agreement).   For the 29 cases in which a 14-gauge needle was used, the histology agreement between core and surgical biopsies reached an impressive 97%.   Parker et al. subsequently reported in 1993 a study of breast core biopsies using 14-gauge needles

guided by ultrasound [6]. In that setup, both the ultrasound transducer and the biopsy needle were positioned by hand. The 14-gauge needle was also established as having most suitable size for core needle biopsy of breast tissue. Of the 181 biopsies performed in that investigation, the core biopsy results agreed 100% with surgical biopsy results in the 49 cases in which surgical biopsy was performed after the core biopsy. Among the other 132 cases that had a benign core biopsy result, patients were followed-up for 12-36 months after the core biopsy, and no patient was diagnosed with breast cancer during that period. The success of the simpler ultrasound-guided core biopsy continues to this day. As recently as 2008, Schueller et al. reported a study involving 1352 US-guided needle core-biopsies, of which 1061 case were followed by surgical biopsy and the other 291 benign results were followed up for at least two years [7]. The agreement between the needle core biopsy results and either the surgical or follow up results agreed 95.8% of the time. Needle core biopsies have been validated over the past 20 years as a viable but cheaper and simpler alternative to surgical biopsy.

The other widely used needle-based alternative to excisional biopsy is the fine needle aspiration biopsy. This technique was introduced to the US earlier than core needle biopsy [8]. FNAB uses a much smaller needle, 18-27 gauge depending on position and size of lesion, compared to the 14-gauge needle used for reliable CNB. Such a small needle size is possible because FNAB is based on cytopathological (cell-level) instead of histopathological (tissue level) examinations. Cells gathered from FNAB is typically smeared directly on slides and stained for better visualization. Different smearing methods can be used; the most common are alcohol-fixed Papanicolaou/H&E stains and air-dried Romanowsky-type stains. However, the success rate of this technique is heavily dependent on user proficiency. The reported sensitivity of FNAB varied widely from trial to trial until a uniform approach was adopted as during a FNAB conference in 1996 [9]. The conference concluded that by properly correlating FNAB with initial physical examination and imaging of suspect lesion, the sensitivity and specificity of FNAB in diagnosing breast cancer can reach 97%-100% and 98%-100%, respectively.

Barra et al. reported in a 2007 study that by employing both the ultrasound-guided CNB technique established by Parker et al. in 1993 and the uniform approach to FNAB recommended by the 1996 FNAB conference, FNAB still performed poorly compared to CNB [10]. Of 264 suspect lesions that were biopsied using both CNB and FNAB in the same setting and then excisional biopsy, FNAC results had an absolute sensitivity and specificity of 68.5 and 66.7, respectively, compared to the excsional biopsy results. CNB results had an absolute sensitivity and specificity of 88.3 and 95.2, respectively. The result of this study resembles that of a seminal investigation more than 15 years earlier, in which Dowlatshahi et al. reported FNAB having a sensitivity of 32% compared to 41% for CNB [11]. These results indicate that despite having a uniform guideline for maximizing the performance of FNAB, this method remains more challenging than CNB. The user's ability to follow the guidelines influences the results much more than in for CNB.

It is not surprising that FNAB is more challenging than CNB. FNAB results are based on cytopathology, whereas the CNB results are based on histopathology. While it is relatively easy to acquire cellular information from a tissue sample; the reverse is not true. When suctioning out cells, FNAB cannot preserve the morphological features of the tissue that contained those cells. The subsequently cytopathology relies on cellular information only. Although this is sufficient in some cases, the range of disease to which FNAB is applicable is less than CNB because it inherently possesses less information.

Fiber optical imaging systems
Based on existing trends in making the diagnosis of cancer as un-invasive as possible, one logical next step could be to perform pathological examination without physically removing the suspicious tissue: an optical biopsy. Trying to look inside the body is an age-old goal of physicians; one of the first successful medical endoscopes was developed by Desormeaux in 1853, although physicians from much earlier times have tried to probe into various orifices of the body [12]. Since those early days of crude endoscopes, advances in miniaturized optics and optical fibers have enabled tremendous advances in the field of in-vivo optical imaging, especially in the last 20 years [13]. Today's fiber optical in-vivo imaging systems can penetrate solid tissue, employ a wide variety of contrast agents, and visualize their target using techniques ranging from physical image formation to interferometry.

The first fiber optical imaging systems were single fiber scanning confocal microscopes designed to extend the reach of confocal microscopy to otherwise inaccessible sites [14, 15]. This single fiber approach has one severe limitation: in order to form an image the distal tip of the fiber needs to scan across the surface of interest. The light it gathers at each point is re-assembled into an image of that surface. Therefore, a scanning mechanism is needed at the distal end of the fiber. Over the years, numerous techniques and mechanisms have been developed to allow a single optical fiber to scan a surface, including microfabricated mirrors [16-18], piezoelectric transducers [19], and electromagnetic actuators [20-22]. However, due to current limitations in microfabrication technology, the smallest of these probes that produce an image suitable for pathological analysis is several mm in diameter [18]. Yelin et al. have proposed a spatial encoding scheme using different wavelengths of light to remove the need for a scanning mechanism [23]. However, this technology has only been tested in the imaging of peritoneum surface topology in mouse. It is unclear whether a spectrally divergent beam of light possesses sufficient sensitivity to distinguish the small difference in reflectivity between cell nucleus and cell cytoplasm without significant variation in surface topology. Such is the case of imaging suspicious lesion inside bulk tissue using an inserted probe that is pressed against the tissue. Despite their limitations, however, single fiber optical imaging systems remain a promising tool for in vivo imaging because of the simple fact that the fiber itself can as small as a few hundred micrometers in diameter.

Until the scanning challenge is solved, fiber optical imaging systems are better served by a

coherent fiber bundle instead of a single fiber. Although a fiber bundle is in general larger than a single fiber, it can transfer an image directly from its distal surface to its proximal surface because each individual fiber images a distinct point [24]. This capability removes the need for a scanning mechanism on the distal end of the fiber bundle so the fiber bundle becomes the limiting factor in miniaturization of the probe. Current manufacturing technology allows several thousand single fibers to be packaged in a fiber bundle with a diameter of only a few hundred micrometers [25]. This approaches the practical operational size of a single fiber because a single fiber requires sufficient size to transmit enough light for imaging and to maintain structural stability. This setup has been used successfully in both reflectance based imaging systems [26, 27] and fluorescence based imaging systems [28, 29]. These systems generally still employ a scanning system made of mirrors on the proximal side of the fiber bundle and detect the light from each fiber in the bundle using an avalanche photodiode. The advantage of the APD is its high sensitivity, so even low signals can be detected. The disadvantages of this method include the need for scanning mechanism, which is frequently complex, and the time needed for the scanning. To decrease the time required to scan a complete image, Sabharwal et al. have developed a slit scanning mechanism that scans a whole line of the image at once [30]. Despite their many benefits, the current fiber bundle based fiber optical imaging systems still suffer from an often complicated scanning mechanism at the proximal end. Although the scanning mechanism no longer affects the size of probe tip and the speed of scan has been gradually increasing, the need for moving parts decreases the robustness and increases the size of final system. This makes packaging the system into a device suitable for clinical applications in harsh environments difficult.

In a direct effort to make a fiber optical imaging device that is robust, fast, and suitable for routine clinical use in a variety of settings, Muldoon et al. have developed a fiber bundle fluorescence imaging system that has no scanning components [31]. (Fig. 1.2) Image from the fiber bundle is directly acquired by a commercial CCD camera and displayed on a computer screen using commercial image capture software. The system is capable of imaging 4.4 um-wide bars on the USAF resolution target and human oral mucosal cells with visible nuclei after application of medical grade acriflavin. The promising results of this setup in in-vivo human cell imaging and its targeted application for clinical use makes it the ideal inspiration for the hardware aspect of an optical biopsy system for breast cancer diagnosis and monitoring. A complete optical biopsy system, however, will require simultaneous development in image processing and analyzing software and very likely a contrast agent delivery system suitable for use in bulk tissue.
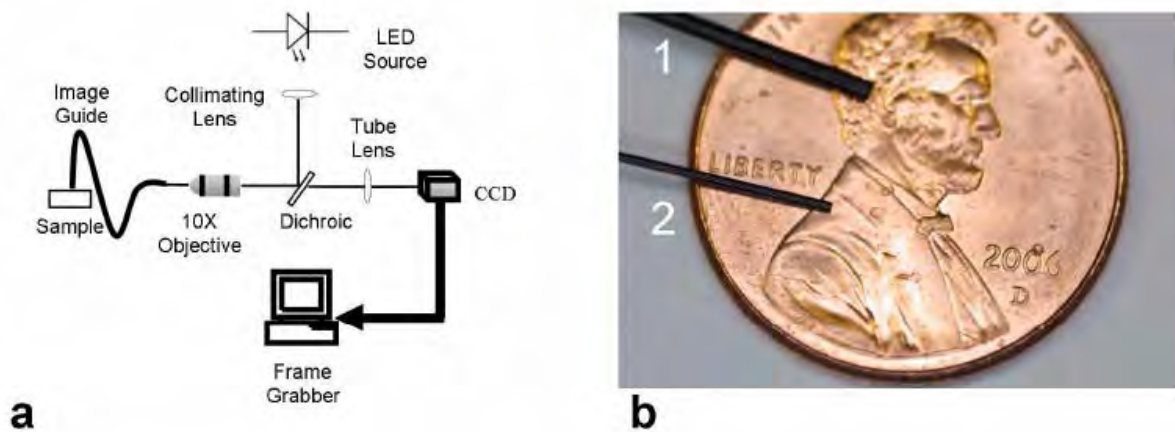
Figure 1.2 [31]: (a) System diagram of a CCD-based non-scanning fiber bundle optical imaging system. (b) Potential 1 mm and 0.5 mm diameter commercial fiber bundles that can be used.

Digital image processing and analysis

Digital image processing and thresholding

Concurrent to the development of hardware systems for in vivo fiber optical imaging, software algorithms to process and analyze the raw images from hardware are also a major area of research. The ultimate motivation for the high amount of interest is two-fold. If optical biopsy is to become a viable alternative to incisional or perhaps even excisional biopsy, the quality of the image produced by the system must convey the same level of information available from physical biopsy slides examined under the microscope. This is challenging from a purely hardware point of view because despite the advances made in miniaturized optics and imaging electronics during recent years, these components still lag behind high precision microscopy optics in performance. Compounding the problem is the fact that the staining agents used in many pathological examinations cannot be readily applied inside in bulk tissue in vivo. Therefore, imaging using optical fiber systems benefit from and sometimes require digital enhancements to accentuate structural features essential for pathological assessment. The other factor that motivates the development of digital processing and analyzes of medical images is the drive for quantitative analysis. Despite being the gold standard in cancer diagnosis, pathology today remains predominantly a qualitative process. The human brain can quickly survey a large area of cells and make an almost immediate estimation of quantitative characteristics such as the overall nuclear-to-cytoplasmic ratio and the proportion of cells undergoing cell division. However, for a human being to precisely quantify this information is nearly impossible due to the sheer # of cells involved and the difficulty of calculating the area of irregularly shaped objects. On the other hand, both challenges are easily solved digitally provided that dividing and non-dividing cells can be accurately segmented and counted. Therefore, development of the software component is an important part in making an optical biopsy system.

One of the first problems encountered in the images from a fiber bundle optical imaging system is the pixilation artifact created by individual fibers in the bundle [31].   However, this is not a difficult problem to solve because the artifact is highly localized in the spatial frequency domain. By transforming the image into the Fourier domain, removing the frequency band corresponding to the pixilation artifact and transforming back to the spatial domain, the artifact can be reduced with minimal distortion to the other features of the image [32].   This basic signal processing method can be easily implemented digitally [33].   Application of this type of image processing has already been reported [34, 35].

Unfortunately, beyond removing the pixelation artifacts, subsequent processing of the image becomes much more challenging.   In particular, finding the appropriate threshold to accentuate the cell membrane and the nuclear boundary, two features essential for cytopathological analysis, does not yet have an ideal solution [36] despite the fact that numerous techniques have been investigated since the 1980s [37].   The fundamental assumption of thresholding is that the features of interest in an image can be assigned numeric values that are significantly different from values in the background without or without first undergoing a mathematical transform. Furthermore, should such a significant difference exist, a suitable threshold value must be found to separate the feature values from the background values.   One of the most common problems for accurate thresholding is non-uniform background; this can easily caused by non-uniform illumination or different tissue types in an optical fiber image.   A threshold value suited for one part of the image is unlikely to be suitable for another part, particularly for the two extremes of the variation.   Global background correction schemes exist [38, 39].   However such correction schemes usually either require a priori knowledge of the kind of non-uniformity that can occur, so the proper correction filter can be designed, or distort the interesting features of the image during correction in such a way that renders subsequent thresholding difficult.   Adaptive thresholding has been proposed as a possible solution to non-uniform background without the adverse effects of global background correction [40].   Although a suitable local region size still needs to be manually defined, the algorithm automatically computes the most likely threshold value in that region by assuming the background is uniform.   Therefore, as long as a reasonable region size is chosen, the exact nature of global background non-uniformity need not be known. Furthermore, because no correction is applied, there is no risk of feature distortion.   Despite these techniques, straightforward thresdholding is still unsuitable to process an image for which a suitable threshold value cannot be found, a common problem when trying to detect edges in an image that show gradual instead of sharp edges [36].

The watershed algorithm
Because gradual edge detection is such a widely demanded application of image processing and analysis, one popular method has evolved over the years specifically to perform this task without using any thresholding: the watershed algorithm, first proposed by Beucher and Lantuejoul in 1979 [41]. The watershed method works in a way analogous to water filling a landscape. (Fig. 1.3)

The starting point of the algorithm is the image as an intensity map; this can be the intensity of the image directly or the intensity of a transform of the image, e.g. its gradient. If we imagine a 3D graph of the intensity map, regions of high intensities will be ridges and hills while low intensities will be represented by valleys and pits. Starting from the lowest points, we gradually fill up the valleys and pits with water; in actual terms, lowest intensities are successively discarded as background. A condition is imposed on the filling of water: no two pools of water that started separately can be joined. The intensity map will be gradually filled until it cannot be filled anymore without violating the condition just described. The remaining ridge tops will be the boundaries that need to be detected. This analogy is slightly misleading because if the water were rising uniformly throughout the map, some ridges will drown before the tips of others were approached. This is where the analogy ends; at each intensity, all points whose discarding does not violate the no-joining condition will be discarded as background. So intensities discarded as background in some parts of the map are preserved in other parts. Since it as proposed, the watershed algorithm has been used in a wide variety of image processing applications [42, 43].
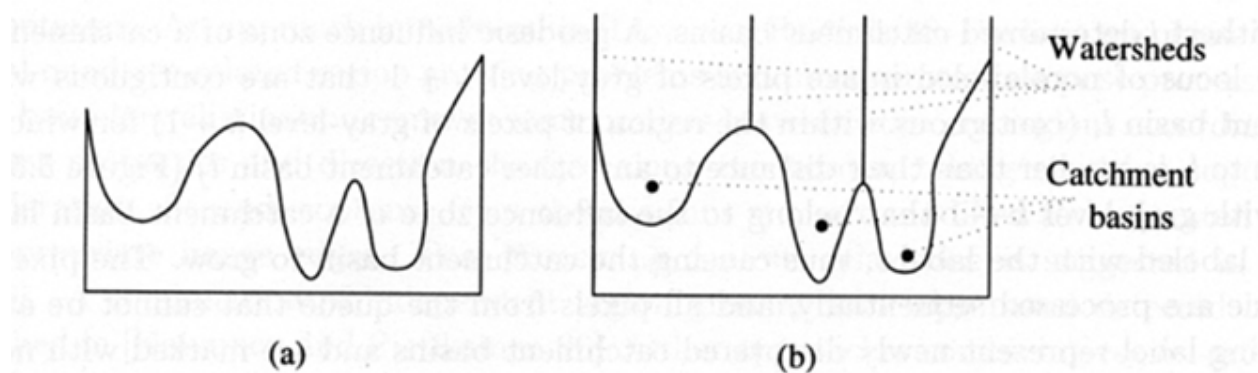

Figure 1.3: Conceptual representation of a 1D watershed algorithm. The local minima in the image (a) can be viewed as catch basins in which water accumulate. As the water rises, the highest point between two catch basins is a watershed (b), or a boundary to be detected. (Image and caption from http://iria.pku.edu.cn/~jiangm/courses/dip/html/node139.html)

However, directly applying the basic watershed algorithm to a complex image such as that of tissue would cause significant over-segmentation. Due to the large variation present in these images, there may be many intensity local minima in a single object: a cell, a nuclei, or the background. To overcome this problem, various efforts to develop a seeded watershed algorithm have been reported [42-47]. The basis of the seeded watershed algorithm is to fill the intensity map starting from only designated locations, or seeds. All other local minima will be disregarded, and only pools that started from seeds should not touch. This method creates its own problems. Automated seeding algorithms are imperfect, frequently putting more than one seeds in one object of interest, e.g. a cell, and none in others, leading to incorrect segmentation [42]. Manual seeding, on the other hand, is an extremely laborious process for images

containing a large number of objects [45]. Despite these difficulties, the watershed algorithm remains a useful image processing method because of its robustness in accurately detecting boundaries given correctly placed seeds. A useful direction of research, then, seems to be to develop a competent automated seeding algorithm to be used with the watershed algorithm for boundary detection.

Dynamic programming and the optimal path problem

While a reliable automated seeding algorithm is being developed, alternative means of boundary detection without thresholding have emerged. One of the most promising techniques employ dynamic programming to solve a optimal path problem along the boundary of interest that would otherwise be computationally intractable. Baggett et al. reported one implementation of this technique in 2005 [48]. The problem can be broadly separated into two sub-problems of design—formulation of an optimal path problem—and implementation—solving the optimal path problem using dynamic programming. For the design sub-problem, Baggett et al. first manually designates a point near the center of the object of interest, e.g. a cell, and another point on the boundary to be detected. To detect the entire boundary, a region of the around the center point is transformed from polar coordinates to Cartesian coordinates with the designated boundary point simultaneously on both edges of the transformed image. (Fig. 1.4) The optimal path is the path of highest average intensity between the two points on the edges. In other words, in the original image, start from the boundary point and proceed either clockwise or counterclockwise and find the path of maximum average intensity until the path forms a loop and returns to the boundary point.
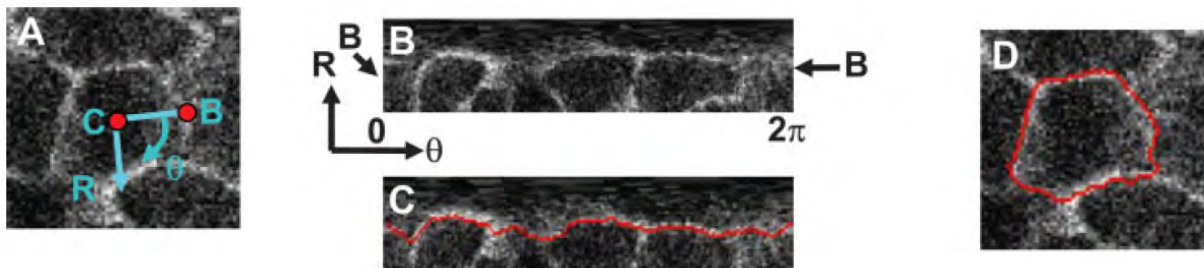

Figure 1.4 [Figures and caption from 48]: The optimal path problem to detect boundary of a cell in an image involves (A) selecting a point central to the cell and another point on the cell boundary, (B) transforming an area around the central point from polar to Cartesian coordinates, (C) finding the path of maximum average intensity in the transformed image, and finally (D) performing an inverse transformation.

To solve the optimal path problem, a gray-weighted distance transform is used to find the path of highest average intensity between the two boundary points on the edges of the polar-to-cartesian transformed image. This method is employed because it is amenable to dynamic programming. A simple example illustrates this method. (Fig. 1.5) In a simple MxN image, designate one pixel on the edge as the starting pixel. First, generate a MxN map A

14

containing the distance of each pixel in the image from the starting pixel; map A is completely filled first. Then, generate a 2nd map MxN B containing optimal cumulative intensities of each pixel. To starting filling B, the pixels with the highest values in A have B values equal to their original intensity in the image. The we move on to pixels with A values of one less. For each of these pixels (call it P), find all adjacent pixels with A values of exactly one more; then, from those adjacent pixels find the one with highest B value; then add that B value to P's intensity in the original image; finally, set P's B value equal to that sum. After that, go to pixels with A values of one less still and iterate until the starting pixel is reached. To find the path of highest average intensity from the starting pixel to any destination pixel, simply start from the destination pixel and trace backward, in strictly decreasing A value, along adjacent pixels of highest B value until the starting pixel is reached. To prove why this method always gives the maximum average intensity, a detailed study of the theory of dynamic programming [49-51] and its application in optimal path finding [52, 53] is required.
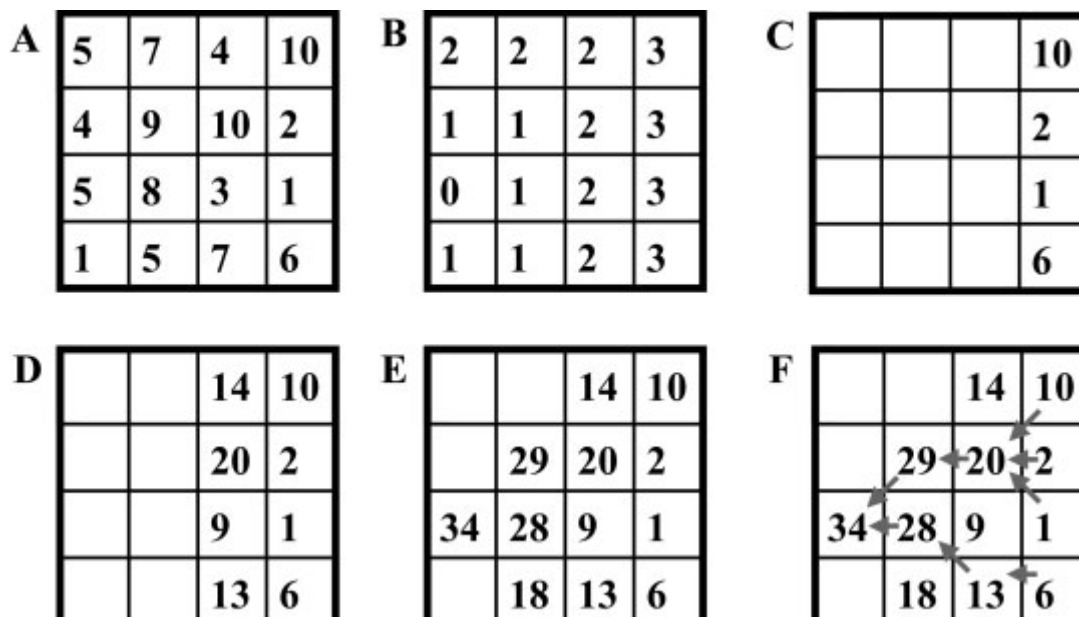

Figure 1.5 [Figures and caption from 48]: A simple figure depicting the steps in gray-weighted distance transform from (A) the intensities in the original image, (B) a map of pixel distance from the starting pixel, and (C) the optimal cumulative intensity map, through successive iterations (D) and (E) to fill the cumulative intensity map until the optimal path from the starting pixel to any non-trivial pixel can be found by backtracking through the highest adjacent cumulative intensities (F).

Since its introduction to image processing, dynamic programming has been used in a variety of projects to segment both 2D [54, 55] and 3D [56, 57] images. The main limitation of formulating cell boundary detection as an optimal path problem solved by dynamic programming, at least using the aforementioned method, is the need for manual placement of two points: one at the cell center and one on the cell boundary. To segment a large number of cells in a tissue image, the amount of user interaction can be significant. A major benefit of this technique is that given a

complex image of cells, individual cells can be marked and segmented in isolation. Such high degree of control is impossible for the watershed method because to place only two seeds in a complex image, even if one is inside a cell and one is out, there is no guarantee that when the seeds begin to form pools and fill the image, the highest remaining ridge separating the two will be the correct cell boundary, especially for tissue images in which cell boundaries appear as a interconnected network of high intensity ridges. On the other hand, dynamic programming methods require a substantial amount of computation to segment just one cell, and cells need to be process individually. This requires considerably greater computational resources than the watershed method, which processes the entire image at once until only the boundaries remain.

It is clear that both the watershed algorithms and the dynamic programming methods have their benefits and limitations; however, one limitation that exists in both methods is the need to place marks in the image to indicate objects of interest, such a cell. For either method to work in an automated or fast image enhancement or analysis software package, the placement of such marks (seeds or central/boundary points) needs to be automated yet reliable. One possibility to solve this problem is by using a Hough Transform to identify the center of cells.

The Hough Transform is a technique to extract generalized features from a data set that may contain imperfections or significant noise [58, 59]. One example would be to extract a circle from an image of a circle made up of broken arcs. In the simplest terms, the Hough transform works by first defining the feature of interest using a parameter space, followed by investigating every point in the dataset for possible sets of parameters that define an acceptable feature that includes that point and adding a count to the appropriate bin in the parameter space for each set that is found, and finally picking the appropriate bins in the parameter space that has the highest number of counts. A simple case for detecting the line formed by three points is illustrated in Figure 1.6. For circles, the Hough transform typically uses three parameters: the coordinates of the center and the radius. Some groups have reported studies incorporating the Hough transform in software algorithms to segment biological images [60-62]. However, applying the Hough transform to the analysis of biological images is very challenging because (1) biological structures such as cells are frequently irregular in shape and cannot easily be parameterized and (2) biological images frequently contain too much information for Hough transform to be performed in reasonable time without a highly optimized software algorithm. Despite these limitations, the ability of the Hough transform to penetrate imperfection and noise is very attractive. With research and development, it may be possible to adapt the Hough Transform as a tool to reliably mark the cells/nuclei in a tissue so that either the watershed algorithm or a dynamic programming technique can be employed for boundary detection.
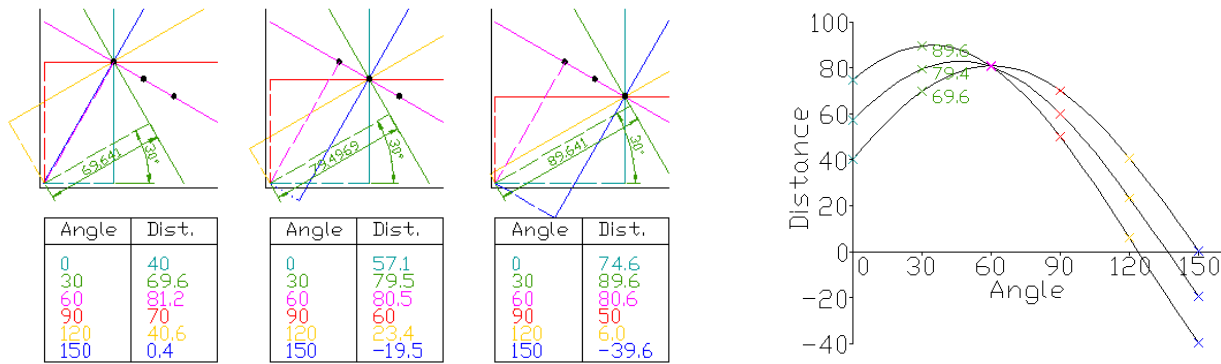
Figure 1.6: To start the Hough transform, the line to be detected (target line) is described by two parameters: (1) the slope of another line (parameter line) that is both perpendicular to the target line and passing through the origin, and (2) the distance between the origin and the intersection of the parameter line with the target line. The two parameters form a two-dimensional parameter space (figure, right), called a Hough space in this case. For each of the three points, a number of potential target lines that contain that point are considered (solid lines, left top). For each of the potential target lines, the two parameters of its parameter line (dashed lines, left top) is recorded (table, left bottom). Assume that for each point, a substantial number of potential target lines are investigated and the parameters associated with each record in the parameter space, the parameter space eventually looks like the figure on the right with three lines. The intersection of the three lines represents the parameters associated with the target line that includes all three points. (Image and accompanying caption from http://en.wikipedia.org/wiki/Hough_transform)

Results Achieved in Months 1-12

Development and testing of a needle compatible optical biopsy system with digital image enhancement and analysis

Preliminary work: hardware system

We have built and tested a prototype setup in order to investigate the hardware capabilities of the optical biopsy system. (Fig. 1.7) The setup maximizes simplicity and minimizes the cost while meeting the core design criteria essential to minimally invasive optical biopsy. The intentional open-air layout permits easy replacement of various components and modifications to the optical pathway. This approach allows continuous optimization of the design—to balance performance, size, cost, and robustness—while adhering to a set of pre-determined requirement.
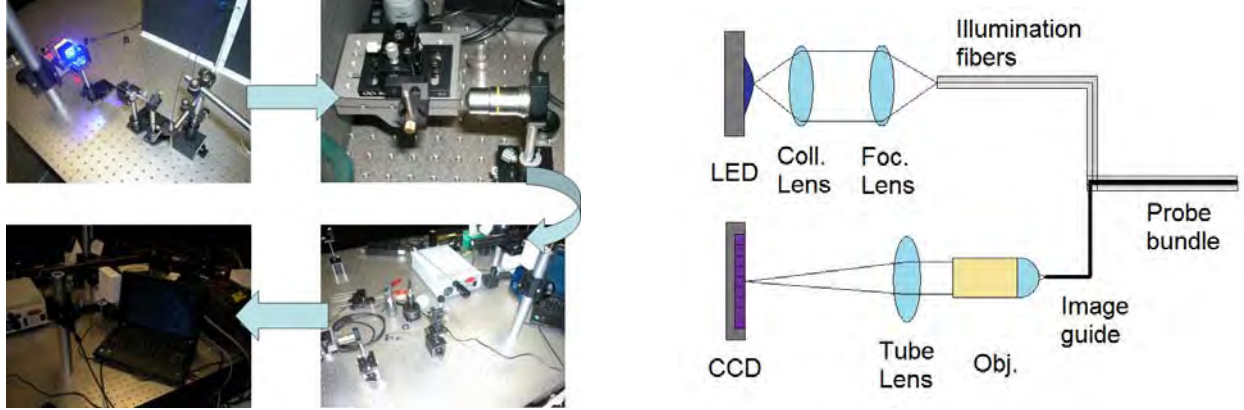
Figure 1.7: Photos (left) and schematic (right) of the optical biopsy system hardware prototype.

The optical train starts at a 455 nm peak-wavelength, 20 nm HWHM LED (Luxeon III Star, Philips). This light source was chosen because it was demonstrated in a previous study that this wavelength of excitation light is suitable for fluorescence imaging using acriflavin as contrast agent [31]. It is useful to build a prototype that possesses the flexibility to image in both reflectance and fluorescence mode to enable testing of all the agents developed in Project 2. The viability of using a single light source for both modes can then be assessed.

Light from the LED is collected by a planar-convex collimating lens (f = 25.4 mm, Newport) and transmitted to a planar-convex focusing lens (f = 62.9 mm, Newport), which focuses the light onto the proximal tip of a bundle of two illumination fibers (NA = 0.22, 200 um diameter; Thorlabs). The collimating-focusing lens pair was chosen to transmit the maximum amount of light from the LED to the illumination fibers. 25.40 mm is the shortest focal length available in a standard Newport lens set. The LED is purposely placed one focal length away from the front principle plane of the collimating lens to ensure light exiting the collimating lens is essentially parallel. Using a collimating lens with the shortest focal length means the collimating lens is as close to the LED as possible, capturing the maximum amount of light.

The focusing lens was chosen so to have the shortest focal length while keeping the light within the acceptance cone of the illumination fibers. Given NA = 0.22 for the illumination fibers, their maximum half angle θ of light acceptance in air (n = 1) can be calculated as

$$\sin^{-1}(NA/n) = \theta$$
$$\sin^{-1}(0.22) = 0.222 \text{ rad}$$

To keep the angle of light from the focusing lens with diameter d and focal length f within the acceptance angle of the illumination fibers, it is necessary that

$$\tan^{-1}(d/2f) < \theta \text{ or } f > d/2\tan(\theta)$$

We used standard Newport lenses with diameter of 25.4 mm, so

$$f > 25.4/2\tan(0.222) \text{ [mm]}$$
$$f > 56.3 \text{ mm}$$

The smallest focal length greater than 56.3 mm in the lens set was 62.9 mm. So this was chosen to be the focusing lens. The separation between the collimating and focusing lenses were based purely on setup convenience and in this particular instance measured 140 mm.

The distal ends of the illumination fibers are positioned co-axially with an image guide (3000 single fibers, 240 um outer diameter, 200 um picture area diameter, NA = 0.35; Sumitomo Electric). Both the illumination fibers and the image guide were chosen for their small size; each illumination fiber has an outer diameter of approximately 150 um after buffer stripping. Together, the two illumination fibers and the image guide were inserted into the bore of a 20-gauge needle with (584 um inner diameter, 902 um outer diameter; Sigma-Aldrich). This ensured that the needle probe of our optical biopsy system is on the large end of FNAB needles, some of the least invasive biopsy needles available.

While we paid close attention to the size of the needle probe, we also made sure that the image guide met minimum resolution and field of view requirements. Based on its picture area diameter and the number of fibers, we estimated the center-to-center spacing between the fibers to be approximately 3.7 um--200 um/sqrt(3000)—giving a Nyquist limit resolution of 7.4 um; this meets the requirement of imaging at the 10 um size scale of human blood and epithelial cells. At the same time, the field of view of the image permits simultaneous examination of some 300-400 cells—$\pi(100um)^2/\pi(5um)^2$, a reasonable size to examine even tissue morphology; the needle probe also has the advantage of being movable while imaging. As a consequence of these calculations, we expect the system to image at least at the cellular level while still permitting tissue morphology to be examined.

The proximal tip of the image guide is located at the focal plane of an infinity corrected objective (f = 18.2 mm, Newport). The infinity corrected objective is beneficial in a couple of ways. Because the light exiting the objective is collimated, the tube lens after the objective can be placed at an arbitrary distance from the objective, either saving space or permitting other optical components to be added. Furthermore, the image formed at the focal plane of the tube lens is magnified relative to the image at the focal plane of the objective by a factor K.

$$K = f_{tube}/f_{obj}$$

So the magnification can be adjusted by switching tube lenses with different focal lengths. In the prototype, the tube lens (f = 300 mm, Newport) was chosen to have the longest focal length within the space constraint of the setup.

A commercial CCD camera (AxioCam MRc5, Zeiss) is placed at the focal plane of the tube lens to capture the final image. The camera has 5 megapixels on an 8.7 mm x 6.6 mm CCD with single pixel detector size of 3.4×3.4 um^2. The camera is controlled by its associated software (AxioVision, Zeiss). The camera has a Nyquist limit resolution of 6.8 um, smaller than the 7.4 um resolution of the image guide even without image magnification by the tube lens. So the camera introduces no limiting factor to the prototype system.
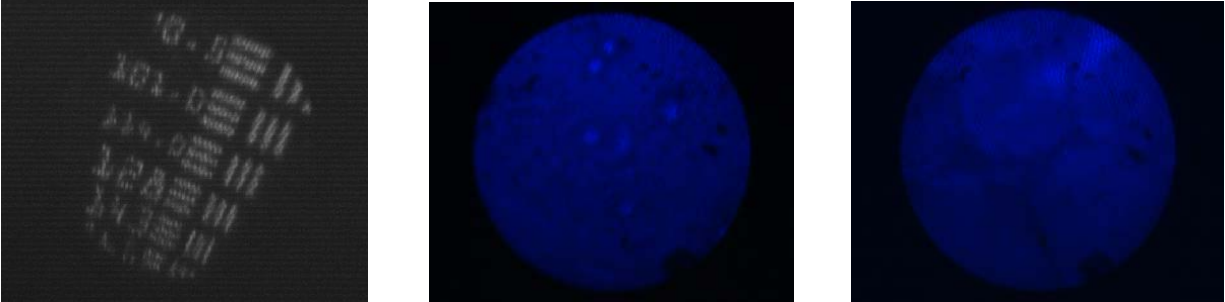
Figure 1.8: (left) Image of USAF resolution targets shows that the 128 cycles/mm bars are clearly distinguishable (grayscale done using Matlab); (center) image of SkBr3 breast cancer cells in culture; (right) image of adipose cells in bulk tissue.

Prior to the start of the project, two specific goals were set for the hardware aspect of the optical system: meeting minimum resolution requirement and acquiring cell structure information. Imaging results from the prototype indicate that the hardware accomplishes both goals. (Fig. 1.8) Imaging of the USAF resolution target showed that the system could achieve a resolution of at least 7.8 um and perhaps as high as 7 um, which is slightly better than even the estimated theoretical limit of 7.4 um. The center and right images further demonstrate the capability of the system to image both cancer cells in culture and adipose cells in bulk tissue (we are using chicken tissue from the grocery store until we receive regulatory approval and SOW modification for breast tissue protocols). The present investigation does not include the introduction of chemical agents to visualize sub-cellular structures, but the prototype system can image at the cellular level with confidence. For sub-cellular structures larger than the resolution limit of the system, such cancer cell nuclei that can occupy up to 80% of cell area, we expect no problem for our system to image them.

Preliminary work: software program
The software program development is in some ways more challenging than for the hardware system. Unlike the hardware, for which cheap and reliable components exist commercially, most of the algorithms for the software are still being developed. However, we have identified several very promising algorithms to perform specific functions in the program: the Hough transform for cell localization, the watershed algorithm for broad feature extraction, and dynamically programmed optimal path finding for specific feature extraction. As we research

and develop these techniques for the optical biopsy system, new ideas and results will continually be reported by us and many others.   We are confident that like the hardware, the software program will shape up to be exactly the tool we need to perform breast optical biopsy.

As a first step, raw images from the hardware are first processed in the Fourier domain to investigate the efficiency with which pixelation artifacts caused by fibers can be removed. (Fig. 1.9) The Fourier transform of the raw images clearly shows a clearly define frequency band corresponding to the pixelation artifact, which occurs regularly in space.   By removing that narrow range of frequency components using a band-stop filter, the artifact can be largely removed without significantly distorting other features of the image.   By further changing the color map of the image and implementing simple histogram stretching, the raw image can be made much more visually clear with minimal effort.
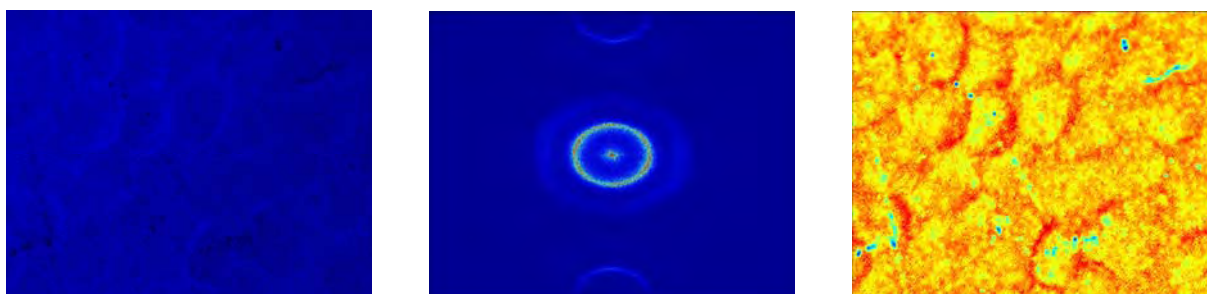

Figure 1.9: (left) A raw image of adipose cells in bulk tissue from the prototype setup using a larger image guide more suitable for software development; (center) the Fourier transform of the raw image shows a clear and bright ring (red-yellow) corresponding to the pixelation artifact; (right) the processed image using a different color map after band-stop filtering and histogram stretching.

Because we want minimize the burden on the physician when using the optical biopsy system, we started the algorithm development with the Hough transform.   During our review of existing image processing methods, we noticed that both the watershed algorithm and the optimal path finding method suffer from the need for manual marking of cells in a tissue image.   It is therefore logical to try and solve that problem first.   We performed an initial investigation of applying the Hough transform for circles to the analysis of cells in a tissue image. (Fig. 1.10)
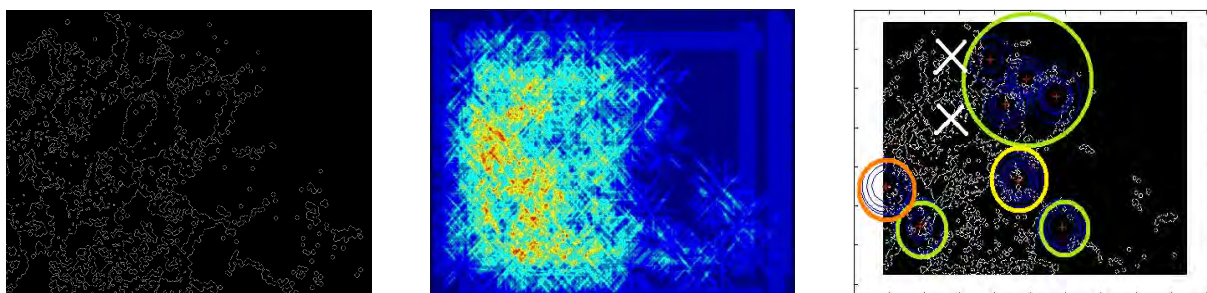

Figure 1.10: (Left) To perform the Hough transform on a tissue image, the set of points roughly corresponding to the cell boundaries must first be identified. (Center) The parameter space requires an adaptive local thresholding

algorithm to identify bins with the highest counts that are most likely to represent actual cells. (Right) A simple Hough transform for detecting circles extracted 8 cells from the image, of which 6 could be confirmed as correct by visual correlation between the program output and the original image (green) and 2 could not be confirmed with one more likely to be correct (yellow) and one more likely to be incorrect (orange).   At least two cells visible in the original image were missed by the algorithm (white cross).   The original image is the same one in Fig. 1.9.

Before the Hough transform can be used, it is necessary to first identify the set of points that has a reasonable probability to be the cell boundaries.   This set needs not be comprehensive or completely accurate.   The only requirement is that the points roughly represent where the cell boundaries are located without too much noise.   We chose to use a gradient map plus thresholding approach for the initial testing because it is simple to implement and suits well the wide cell boundaries in the image.   This technique is a poor choice if we wanted a precise extraction of size information because more than one boundary surrounds a cell; however, since we care mostly about locating the cells, having an extra boundary is actually helpful.

The Hough transform is subsequently performed on the set of boundary points.   The boundary point plot (Fig. 1.10, left) showed a great deal of noise in the lower left region.   Comparison with the source image showed that area to have some sharp edges without clearly discernable cells. This phenomenon was more trouble than the right region of the image that has no discernable cells or edges because edges not part of a cell contributes to noise.   Because the boundary point plot showed a great deal more noise in the left bottom region, an adaptive local thresholding algorithm was used to pick out the most likely centers of circles from the parameter space (Fig. 1.10, center), representing cells in this case.   A local thresholding method prevents high noise areas from affecting low noise areas.

In the end, the simple test algorithm we used extracted a total of eight cells, six of which have correct cell locations—judged as having the cell center mark inside the actual cell—after correlation with the original image; two extracted cells cannot be confirmed by correlation with image because there is insufficient detail in the image. (Fig. 1.10, right) At least two visible cells near the top left of the original image were missed by the algorithm.   However, given that this was an initial attempt to assess how a straightforward Hough transform for circles would perform on a difficult image, the result was very encouraging.   Just by testing a simple Hough transform without any modifications to account for irregularities in cell shapes or distortions in the image, we extracted most of the visibly identifiable cells fro the image with an accuracy of 75%.   Most importantly, we have established that the Hough transform is a viable tool to locate the cells in a complicated tissue image.

Next steps: hardware

The testing of the hardware has shown that the goals we set at the beginning of the project have been largely accomplished.   Both the resolution of the imaging system and the ability of the

system to image biological structures have been demonstrated.   There remains, however, much that can to be done on the development of the hardware.   Because the successful completion of Project 1 depends on the achievement of both software and hardware goals, improvements to the hardware can continue at least until the software has achieved its goals; every improvement in hardware makes the software's job that much easier.

The most logical place to start improvement is in the needle probe.   So far, we have tested just one probe size based on the smallest components available.   However, should smaller probes be possible, how small becomes too small?   Background studies revealed that despite its superiority in size, FNAB is more challenging to use correctly because it sacrifices the ability to perform histopathology in order to employ the smallest possible needles.   There is no doubt that an optical biopsy system also has a lower size limit beyond which it loses performance, which can be caused by overly small field of view or too little light being transmitted.   As the needle gets smaller, safety may also become a concern; although it does not seem probable that structural failure can happen before performance reduction.   In any event, a fuller investigation on the optimal size for the needle probe is a worthwhile endeavor.

While considering different needle sizes, the question of light transmission naturally comes up. The present setup uses separate illumination fibers even though the image guide is capable of simultaneous transmitting light in both directions.   This was done to avoid specular reflection from the various optical-air interfaces in the optical pathway.   There are certainly methods to minimize the specular reflection—index matching, polarity control, angled optics, just to name a few—but the possibilities extend further.   For example, the image guide has many individual fibers.   It is potentially possible to design a precise enough optical pathway that delivers light through only some of fibers, say those on the outside, and use only the inner fibers for image transmission.   To accomplish this without fiber bifurcation is both an impressive challenge and very rewarding because the needle probe size in the present setup can be reduced by 50% if the illumination fibers are removed.   To go smaller, these modifications are worth testing.

On the other hand, going smaller is not the only option.   CNB using a 14-gauge needle remains more widely used in the US today than FNAB.   If biopsies with the same quality as CNB could be performed without tissue removal , even if the same 14-gauge needle were used, that would be a positive development in itself.   It would improve the lives of all CNB patients.   If the quality of the optical biopsy can be made higher than CNB, then it's even better.   Given this possibility, an investigation toward the larger end appears just as worthwhile as going small; on top of that, bigger is easier in optics.

These are just some of the possible ways in which our prototype optical biopsy system can be improved.   Even if the current setup by some miracle performs just perfectly, investigations into the limits of the system design and the various ways different components can be modified will yield invaluable insight into the design of future medical imaging equipment, say an optical

biopsy system for the brain, a very dangerous procedure today.   Finally, after both the hardware and software objectives have been accomplished and the desired investigations made, the system will be packaged.   While the prototype system benefits from an open and easily modifiable setup, the system must be made portable, compact, and robust for clinical testing.   It must also have a clean and intuitive user interface.   In short, the system should perform all the difficult tasks on its own to make the clinician's life as easy as possible.

Future work: software

Unlike the hardware side, many challenging tasks remain on the road of software development. Although there are alternative techniques in consideration that will be investigated, these efforts are for the most part critical to the success of the optical biopsy imaging system.   The best approach is to take one step at a time and gradually build up the software program until every algorithm in the sequence falls into place.

The first task in software development is the adaption of the Hough transform to a algorithm that can mark the location of cells in an image so that subsequent processing and analysis by either the watershed algorithm or the optimal path problem can be performed.   Hot on the heels of a successful initial test, there is every reason to believe that a suitably modified Hough transform can accurately identify the majority of cells in a tissue image.   Because the initial test resulted in two extracted cells that could not be confirmed by the original image, there is even the possibility that the Hough transform can help in the identification of important structures that are otherwise difficulty to visualize by the human eye.   However, to develop a Hough transform algorithm is also best done one step at a time.

Before the Hough transform can even be applied, it is necessary to extract the cell boundaries from an image.   The initial investigation showed that through pre-processing, the intensity of boundaries in the image can be greatly increased.   This leads to the possibility of an adaptive local thresholding algorithm, which was used successfully in the initial testing to pick out most likely cell centers from the parameter space of the Hough transform.   This method is more powerful for overcoming noise in an image, the source of difficulty with identifying the cell boundaries in our first attempt.   Reducing the noise in the cell boundary plot goes a long way toward performing a successful Hough transform.

To improve the situation even more, a way to extend cell boundaries will be investigated.   It is clear from Figure 1.9 that cells in a tissue image are sometimes partially blocked.   So instead of a circle or an oval, they show up as a partial elliptical shape.   Using geometric computation and pattern recognition, it is possible to detect a significant arc in the image and then extend that arc into an ellipse by adding false boundary points.   For the cases where the detect arc really is a partial boundary of a cell, the pseudo boundary points greatly increases the chance that cell will be correctly detected by the Hough transform.   In addition to the localization of cells, adding

pseudo boundaries in the analysis could also aid in size estimation of structures; however, that direction of research has the risk of misleading results, and will be pursue separately and with great caution.

In the meantime, the modifications in the preprocessing have given way to the development of the Hough transform itself. One of the assumptions in the initial test was the circularity of cells. Although some cells and cells in culture are often round, cells in tissue are generally not. This is especially true for epithelial cells in highly hierarchical tissue, where they are often flattened ovals with pinching ends. Developing a Hough transform that most accurately parameterizes the shape of the cells to be detected is an important goal in the software development.

Perhaps even more importantly, there is a possibility here to aid the diagnosis of cancer using the tissue image. Because cancer cells lose tissue level control, their morphological structure often differs significantly from normal tissue, especially for cancer of otherwise highly striated cells. As seen in Figure 1.1, cancer in the breast can manifest visually as a concentration of generally round cells surrounded by largely elongated stromal cells. By employing two Hough transforms, each specifically designed to identify cancer or normal cells of the breast, it is possible that some information about the pathology of the tissue under examination can be gathered even at this early stage of image process/analysis. By having two Hough transforms, the localization of cells for subsequent algorithms may also be improved.

The previous proposed investigations are just some of the possible ways in which the image processing/analysis can be improved. As work on the Hough transform progresses, other ideas will likely reveal themselves. After the Hough transform algorithm has been satisfactorily developed, work on either the watershed method or the optimal path problem or perhaps some other new technique will commence. Because these are highly sophisticated image analysis methods, it is not resource efficient to simultaneously develop all of them. Instead, as indicated by the background study, one method will be superior to the other depending on the proportion of cells identified by the Hough transform. It is better to hold off on formulating the specifics until the Hough transform portion has been completed.

After all the above algorithms have been developed and the cells in the image segmented, the techniques to extract the relevant structural data, such as size, morphological score, etc. will be pursued. These are even further out into the future. Unlike the hardware portion, where everything can be planned ahead at once, the software development is best done in stages with the best method chosen at each stage based on the result of the stage before.

Project 2

This project develops the nanoprobes which will be used along with the optical systems created in Project 1 to enable molecular specificity. As our SOW describes, we are developing two

types of materials: (1) non-cadmium luminescent dots and (2) shaped and layered gold nanoparticles. Our first year effort on this project has been focused on the basic materials chemistry development aspects as indicated the SOW. We are ahead of schedule on this project and in Year 1 provide results for both Task 1 and Task 2 rather than just Task 1 as originally anticipated. We also provide preliminary results for Task 3 which encompasses biological evaluation of several different nanoengineered probes including luminescent dots and gold-based nanoparticles (both nanorods and nanoshells). Please refer to the Appendix section for copies of one submitted and three published papers on development of molecular imaging agents for breast cancer applications.

Background

The success of an optical biopsy system that uses contrast agents will depend largely on finding the appropriate agents. Even though gold nanoshells have been the most promising candidates based on our preliminary research, other contrast agents will be evaluated. To ensure that these evaluations proceed in a thorough and consistent manner, a set of guidelines will be used to direct all investigations involving potential contrast agents to be used in the optical biopsy system.

As with all chemicals used in the human body, the foremost question about the contrast agents is whether they are safe to use. Once safety of the contrast agents has been reasonably established, factors relevant to performance will be evaluated. Based on our preliminary study of biopsy staining agents, one of the major questions will deal with time (see Task 3 results for our own work in this area). As revealed by preliminary research, current biopsy staining methods can at best work on a time scale of minutes to hours. While this is not an unreasonable reaction time, indeed appearing fast for use on physical biopsy slides, the optical biopsy system has a much higher demand on reaction efficiency. Since one goal for a contrast agent-using optical biopsy system is site-specific delivery, the imaging needs to occur quickly after the delivery of the contrast agent so that the needle probe does not need to be removed. Therefore, the time it takes for the contrast agent to begin working after delivery will be a prominent factor in evaluating its efficacy.

The other major issue related to contrast agent performance is simplicity. While the need to introduce eosin after hematoxylin in H&E staining already poses a problem for in vivo delivery of contrast agent during optical imaging, the numerous steps in the Papanicolaou stain are outright impossible. The delivery system will be too complex if it has to delivery several chemical agents into the breast with washing steps in between. Fortunately, all the nanotechnology contrast agents under investigation work by themselves. Nevertheless, it is necessary to explicitly specify all steps in applying a particular contrast agent and finding one that is facile to use clinically.

Finally, it is perhaps obvious that the optimal imaging conditions for each candidate contrast agent be thoroughly described.   Some contrast agents work best in fluorescence mode; others work better in reflectance mode.   Still others work well under both conditions.   It is necessary to characterize the optimal imaging conditions so that the feasibility of adapting the imaging system can be assessed and the modifications made prior to testing.   Naturally, the system setup is not the only condition that needs evaluation.   The optimal condition of the contrast agent also needs to be clarified.   It is known that pH, temperature, concentration, and even fluid mechanics can significantly affect the behavior of chemicals or nanoparticles in solution.   The chemical environment and the imaging environment are both important for optimal contrast agent performance.

Other as of yet undiscovered issues may arise during the investigation of best contrast agents. They will be incorporated into the study as they arise.   The aforementioned factors, however, are known questions of relevance based on the preliminary study.   Whether or not other issues arise, the characterizations noted above will be performed for each contrast agent evaluated to ensure a uniform standard.   However, because some factors are more important than others, e.g. safety, if a contrast agent fails a test of higher significance, subsequent tests will not be conducted because agent is no longer relevant.   When at least one suitable contrast agent for clinical use has been found, the contrast agent-based optical biopsy system will be made suitable for clinical testing even while other promising agents continue to be studied.

Once a suitable contrast agent has been identified, the other major research objective is no doubt the delivery mechanism to bring the contrast agent to the imaging site inside the breast. Because our optical biopsy system uses a needle probe, it is very intuitive and logical to build the initial prototype delivery mechanism using a syringe with the needle as both the probe casing and contrast agent delivery channel.   A conceptual drawing of such system is shown in Figure 2.0.   This system has at least two promising benefits.   The first benefit is using the same needle for the imaging probe and the delivery mechanism.   This ensures that the contrast agent is always delivery right where the imaging is happening.   The second benefit is that a syringe, when coupled with a mechanical pump, can deliver very precise volumes of solution at highly regulated rate.   This is crucial for the proper operation of contrast agents that require precise concentrations to balance signal strength and specificity.   It is very possible that the needle syringe will end up being a suitable delivery mechanism.
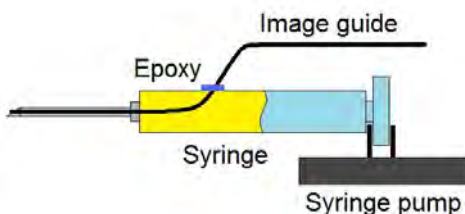

Figure 2.0: a syringe controlled by a syringe pump could be a very suitable contrast agent delivery tool.   The imaging

fibers (illumination not shown) are partly inserted in the syringe.

While the delivery of contrast agent is a straightforward process; the removal of excess contrast agent could be very challenging. Using a needle, there is no easy way to specifically remove excess contrast agent once it is delivered. Pulling back on the syringe with the needle tip inside the breast is simply not appropriate given that the purpose of the optical biopsy system is to minimize pain and suffering of the patient. However, one potential non-mechanical solution is to delivery just the right amount of contrast agent using the precision injection scheme described before. Under delivery is preferable to over delivery because adding additional agent is easy. Mechanical draining may not be necessary.

Another possibility to avoid having excess contrast agent distorting the image lies in molecular specific binding and activation (work underway in portions of SOW Project 2 and Project 3). There are contrast agents activated only after binding a specific molecular target. If such a contrast agent were used, then there is no problem associated with delivering excess agents into the tissue. A further modification of this strategy could involve an activating agent. It is sometimes the case that making as a single chemical that activates specifically is hard, but if a separate agent is introduced later to activate the first, the design of the two agents is easier. The syringe delivery mechanism can be modified to selective inject two different chemicals either together from separate chambers or in sequence. In any case, there are strategies available which employing a custom made delivery mechanism to help remove excess contrast agent without resorting to pulling on the syringe. If mechanical removal really is necessary, capillary action may prove to be helpful. Plants are able to pull water from their roots up to the highest branches through capillary action in special interconnected cells. By custom creation of a needle to have this kind of small channel that connects to a collecting reservoir, it may be possible to remove some contrast agent solution from the imaging site. Because no external mechanical force is applied, the chance that any cells would be severely disturbed is minimal.

Results Over Months 1-12

Our work to date on SOW Project 2 has continued development of layered gold nanoparticles for breast imaging applications and initiated development of two additional classes of agents (cadmium-free NIR luminescent dots, Task 1, and gold nanorods, Task 2 of Project 2). We describe results of these two efforts below.

Synthesis and Hydrophilic Modification of PbS NIR Quantum Dots: We have recently developed methods for synthesis and water solubilization of NIR nanodots described briefly here. These cadmium-free NIR emissive nanodots are appealing not only due to tunable NIR emission but also because the materials are broadly excitable from the UV through NIR. To prepare PbS nanodots, a mixture of 90 mg of PbO (0.40 mmol), 0.25 g of oleic acid (0.80 mmol), and 1-octadecene (ODE) (total weight = 5.0 g) is heated to 150°C. Upon turning colorless, the mixture is further heated to 260°C. 2mL sulfur solution (0.2 M) in ODE is then quickly injected.
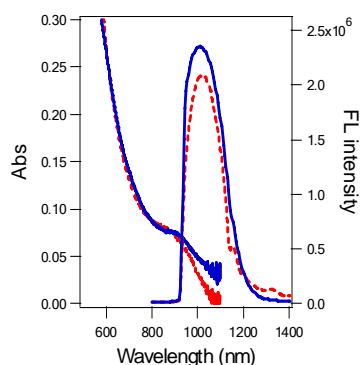
Figure 2.1. Absorption and emission data for NIR PbS quantum dots before (red) and after (blue, measured in PBS) hydrophilic modification. Optical absorption and emission properties are not significantly altered.

The temperature of the reaction mixture is allowed to cool to 200°C to allow growth of the PbS semiconductor nanocrystals. All steps in the reactions are carried out under argon. For imaging applications, the surfaces of the PbS materials must be rendered hydrophilic. The first step in this process is pretreatment with mercapto-propylmethyldimethoxysilane (MPS) and methacryl-ethylenetrimethoxysilane (Si-MA). The reaction is carried out in a 3-necked flask assembled using condenser under argon protection. 1.0 nmol of QDs is dissolved in 1.0 mL toluene followed by dropwise addition of 100 nmol of MPS and 1000 nmol of PEGS at 110°C. After 12 hrs, aminopropyldiethylethoxysilane (AES) is added under argon. The reaction is continued overnight at 100°C. After the reaction is stopped, the QDs are precipitated against n-hexane and redispersed in water. The as-prepared QD aqueous solution can then be transferred to PBS. As shown in Figure 2.1, the process to aminate the surface does not appreciably alter the optical properties.
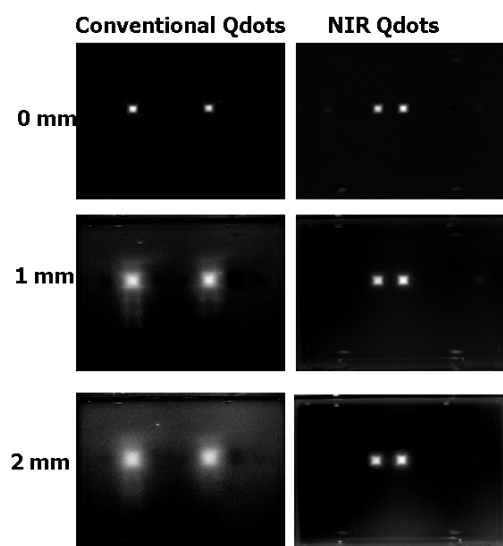

Figure 2.2. Imaging of visible (left) and NIR (right) containing tumor phantom embedded in a tissue mimic. All images were generated using the same silicon CCD with quantum dots synthesized in the Drezek lab.

Imaging with PbS Quantum Dots: As a preliminary demonstration of the imaging advantages of the NIR qdots as compared to those with visible emission and to demonstrate sufficient signal for imaging these particles using a silicon CCD, we embedded tumor phantoms containing identical concentrations of visible or NIR qdots in a mouse tissue mimic and imaged the tumor phantoms as the top surface of the tumor phantom was moved deeper into the mouse tissue phantom (Figure 2.2). Decreased blur due to less scattering of NIR light is clearly apparent. After verifying signal levels were sufficient for imaging using nM concentrations, immunotargeted NIR qdots were developed and evaluated. Following quantum dot synthesis and solubilization, the surface may be conjugated to antibodies using a heterobifunctional cross-linker such as N-[p-Maleimidophenyl]isocyanate (PMPI) or (N-[ß-Maleimidopropionic acid]hydrazide•TFA) (BMPH) which reacts with the hydroxyl or carboxyl group respectively and provides a maleimide functional group on the quantum dot. The quantum dots synthesized are stable in the reagent buffer used for the cross-linker chemistry. The maleimide group is reactive to free sulfhydryl

groups on antibodies.   Prior to conjugation of quantum dot to antibodies, the antibody disulfide bonds are reduced to free sulfhydryls using dithiothreitol, also known as Cleland's reagent. Alternatively, we can utilize a carbodiimide such as EDC and activate carboxyl groups to react with an amine-terminus of an antibody.   The quantum dots are conjugated to the antibody and isolated from unbound quantum dots and unbound antibodies by gel chromatography.   In addition, antibodies may be immobilized via polymer tethering chains.   This can be accomplished with difunctional polyethylene glycol derivatives.   This immobilization scheme may increase the biological activity of the immobilized antibodies by enhancing their mobility and thus their ability to interact with their target ligand.

Cytotoxicity Studies*:*   It is worth noting that the quantum dots agents we propose are cadmium-free, and the lead dose we expect would be required should these particles be considered for human use in diagnostic applications is lower than the average incidental Pb daily exposure in urban environments.   Initial cytotoxicity screens (Figure 2.3) of the NIR qdots have been promising.   Any new formulations of conjugated NIR quantum dots developed for this project will first be evaluated for biocompatibility.   Preliminary screens will determine LC50 values in cultured human dermal fibroblasts with calcein AM/ethidium homodimer staining (Molecular Probes Live/Dead Assay, lactate dehhydrogenase release, and MTT assays.   Changes in proliferation rates will be monitored by staining for proliferating cell nuclear antigen (PCNA) and evaluating growth rates.   Changes in adhesion, spreading and migration will be measured.   TUNEL assays will also be performed to assess apoptosis.   We have recently published (January 2008, *Small*) an extensive review of approaches to assessment of nanoparticle cytotoxicity which provides more detailed explanations of these methods.
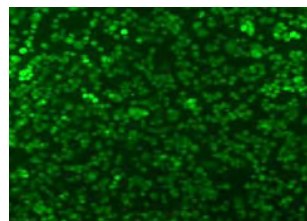

Figure 2.3.   Preliminary cytotoxicity screening of PbS qdots.   Green = live cells (calcein AM).

Project 2, Task 2

It is conceivable that the cadmium-free qdots described above still are ultimately deemed not suitable for in vivo applications. In Task 2 we focus on materials that are gold-based nanoparticles (AuNPs) which are the nanomaterials closest to clinical translation in particular gold nanorods.   To facilitate future applications, it is necessary to synthesize complex AuNPs with high yield and without secondary separation steps to remove spherical or triangular contaminants.   Such synthesis is particularly challenging for long nanorods.   Methods for nanorods synthesis include electrochemical, photochemical, and seed-mediated approaches. In seed-mediated approaches the concentration of gold growth solution is highly dilute (0.01-0.25mM) and further purification steps are required.   We are developing a modified seed-mediated synthesis approach for gram scale synthesis of *NIR* nanorods (as opposed to short nanorods readily produced using standard methods and available long nanorods methods requiring subsequent purification). To demonstrate feasibility (Figure 2.4), a seed solution was

synthesized by adding freshly prepared NaBH$_4$ solution (0.3mL, 0.01M) to a solution composed of HAuCl$_4$ (2.5mL, 0.0005M) and CTAB (2.5mL, 0.2M).
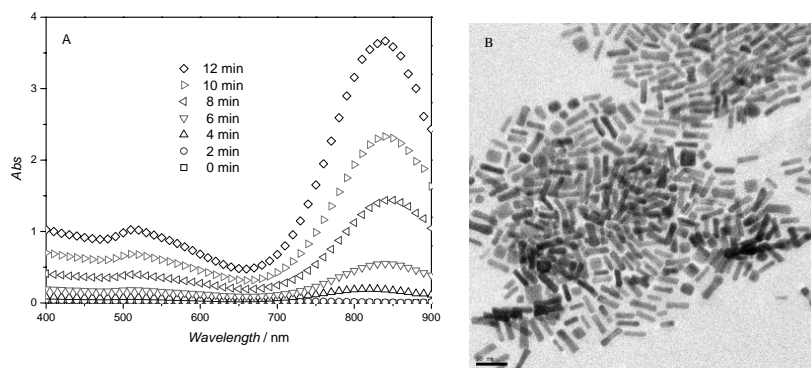

Figure 2.4. Preliminary results demonstrating synthesis of concentrated high aspect ratio (>800 nm peak) gold nanorods. In optimal synthetic conditions, the yield of gold nanorods is up to 0.1 g as compared to 0.02 g using conventional methods. Typical TEM image using the proposed approach *without* any further purification steps is shown on the right.

The seed solution was kept in a 40°C water bath for 15 min to decompose excess NaBH$_4$. Gold nanorod growth solution was prepared adding ascorbic acid (AA, 0.046mL, 0.1M) into a solution composed of HAuCl$_4$ (0.3mL, 0.01M), AgNO$_3$ (0.06mL, 0.01M), and CTAB (3mL, 0.2M). Nanorod growth was initiated by adding the seed solution (0.2mL) into the growth solution. After initial optimization (Figures 2.5 and 2.6), results indicate increasing the concentration of gold growth solution to 1.0mM (current reports do not exceed .25mM) and optimizing AgNO$_3$ can yield gram-scale gold nanorods with concentrations as high as 0.1g/L, a significant improvement over figures reported using standard methods (<0.02g/L). In continued work on Task 2 we will focus on further optimization of seed-mediated approaches to generate improved yields and larger quantities of NIR nanorods.

There are advantages as well as limitations to the use of gold nanorods as compared to gold nanoshells or other gold nanomaterials as in vivo imaging agents. Advantages in size, delivery, and linewidth are accompanied by disadvantages in signal strength. The biological evaluation (SOW Project 2 Task 3+) which will enable rigorous comparisons of all the material classes we are considering. Such direct comparisons of material classes are a present gap in the existing literature in molecular specific imaging agents because nanomaterial groups tend to focus on individual classes of materials within their own research labs.
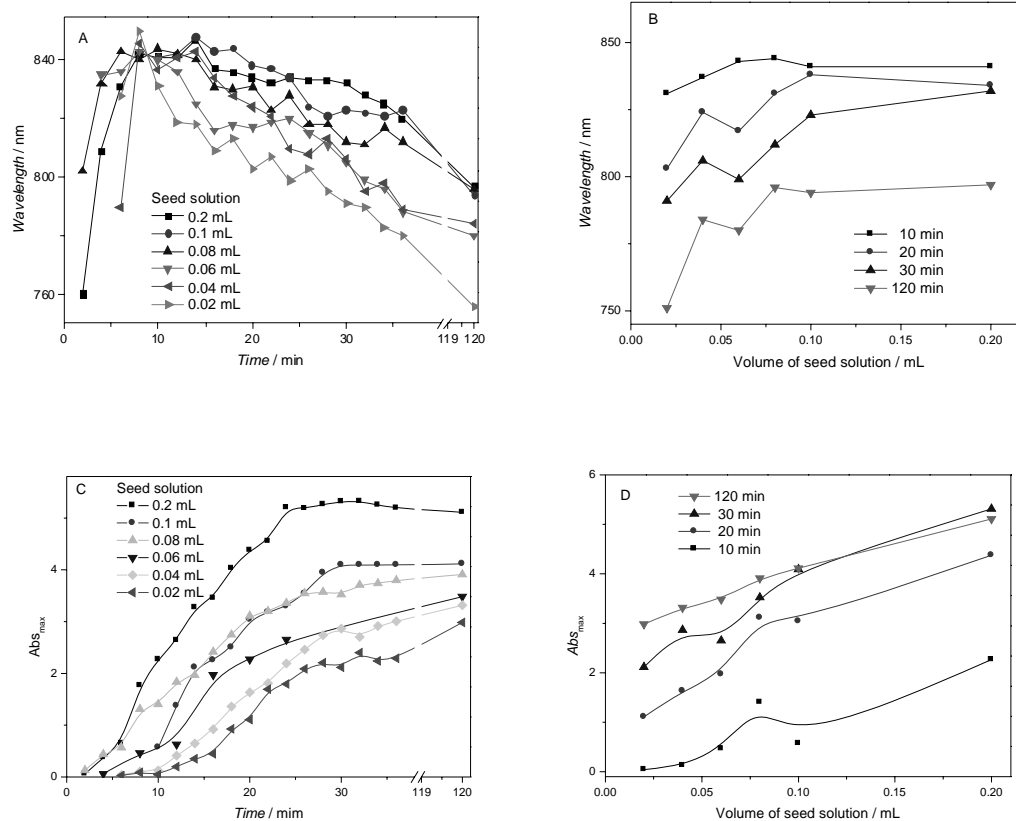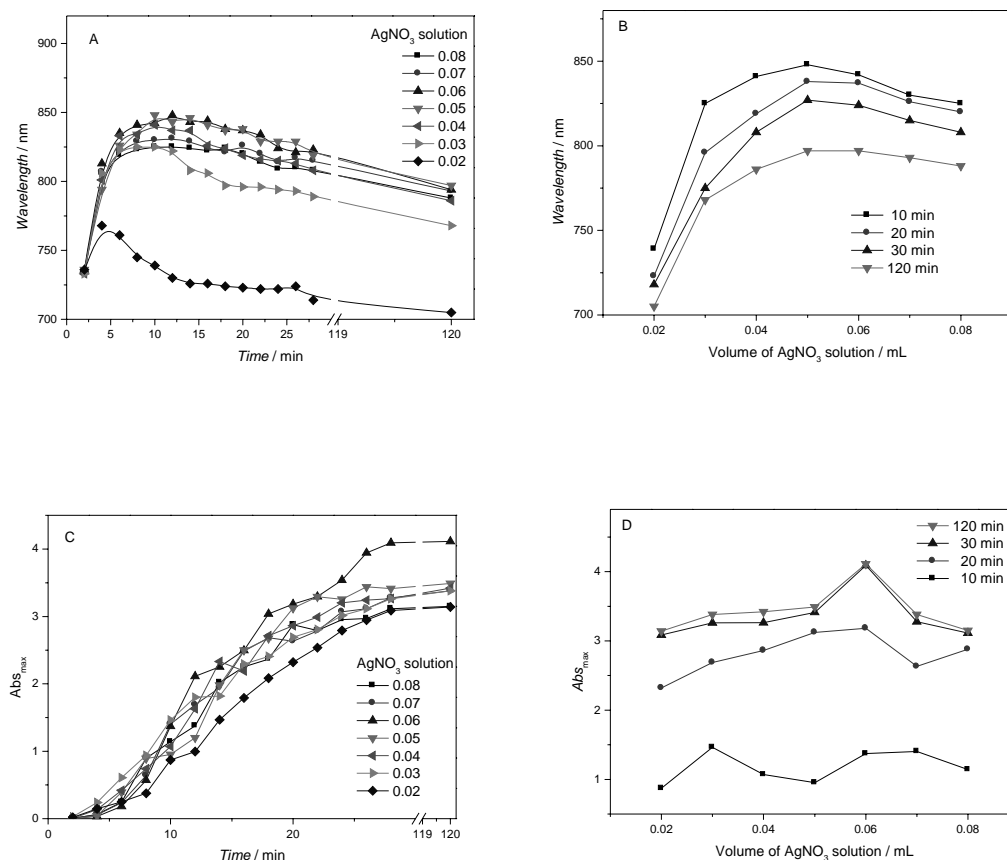
Figure 2.5. Preliminary results: effect of seed concentration. (a) Fluctuation of peak wavelength of Au nanorods with time under Au seed initiation. (b) Correlation between seed amount and wavelength at max absorbance. (c) Absorbance of Au nanorods with time under Au seed initiation. (d) Correlation between seed amount and absorbance. Gold nanorod growth solution: CTAB 3ml x 0.2M, AgNO$_3$ 0.01M x 0.06mL, HAuCl$_4$ 0.01M x 0.3mL, AA 0.1M x 0.046mL.

Figure 2.6. Preliminary results: effect of AgNO₃ concentration. (a) Fluctuation of peak wavelength of Au nanorods with time under Au seed initiation. (b) Correlation between AgNO₃ amount and wavelength of gold nanorods at maximum absorbance. (c) Absorbance of Au nanorods with time under Au seed initiation. (d) Correlation between AgNO₃ added and absorbance of gold nanorods. Gold nanorod growth solution: CTAB 3ml x 0.2M, add AgNO₃ 0.01 M x 0.06mL, HAuCl₄ 0.01M x 0.3mL, AA 0.1M x 0.046mL. Seed solution: 0.2mL.

Project 2, Task 3

Because we are ahead of schedule in imaging agent development, we have also initiated work on Task 3 which is the biological assessment aim of the imaging agent development project. This work is conducted together with MD Anderson Cancer Center and several papers co-authored with Dr. Kuan Yu, leading the MDACC efforts on this project, have resulted.   Those papers may be found in the Appendix of this report which begins on Page 45.   We highlight those results below.

In work published in *Nanotechnology* in January 2008, we developed a polarized light scattering method to quantify gold nanoparticle bioconjugate binding.   To continue development of clinical

applications using gold nanomaterials, it is critical that analytical strategies for quantification are developed. The previous method used to characterize nanoparticle binding requires the measurement of extinction spectra of cells labeled with nanoparticles. This does not result in accurate measurements of bound nanoparticles since particle-particle interaction effects are neglected using such an approach. To avoid the influence of interactions between nanoparticles when they are in close proximity to each other, we have developed a "negative" method of characterizing the binding concentration of antibody/nanoshell bioconjugates targeted specifically to breast cancer cells. Unlike previous methods, we collect unbound nanoshell bioconjugates and measure light scattering from dilute solutions of these nanoshells to achieve quantitative binding information. The interaction effects of adjacent bound nanoparticles on the cell membrane can be avoided simply by measuring light scattering from the unbound nanoshells. Specifically, we have compared the binding concentrations of anti-HER2/nanoshell and anti-IgG/nanoshell bioconjugates targeted to HER2-positive SK-BR-3 breast cancer cells using nanoshells of different sizes. The results indicate that, for anti-HER2/nanoshell bioconjugates, there are approximately 800-1600 nanoshells bound per cell. For anti-IgG/nanoshell bioconjugates, the binding concentration is significantly lower at nearly 100 nanoshells bound per cell. To the best of our knowledge this is the first paper which attempts to rigorously quantify gold nanoparticle binding.
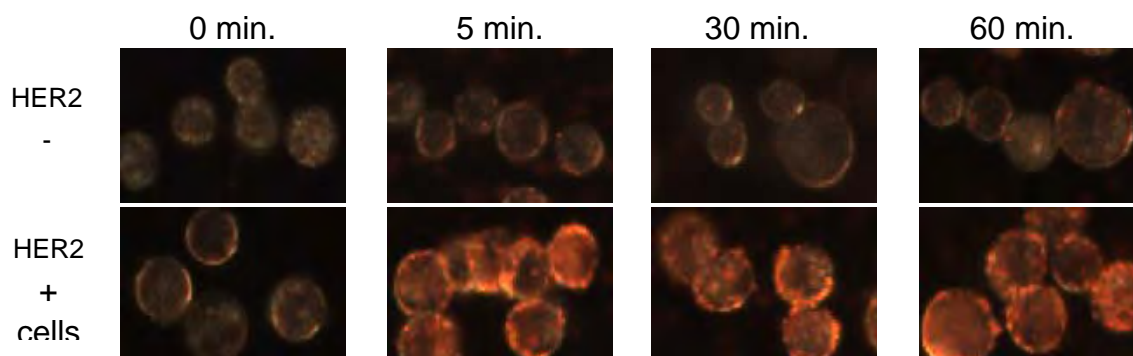

Figure 2.7 Immunotargeted gold nanoshells can produce statistically significant optical contrast in HER2+ cells within 5 minutes of incubation. Due to the patient being anesthetized while tumor margin results are pending, it is essential to minimize the amount of time spent processing the specimens.

In addition to being able to quantify binding, it is also critical we understand the time course of binding events. We ultimately would like to use these particles in clinical applications requiring rapid imaging. Almost all published protocols involving targeted nanomaterials require an incubation period of ~1 hour. This is not feasible for clinical applications which would require a read out in fifteen to twenty minutes. Thus, we conducted a study, which was recently published in *Nanobiotechnology* online and will appear in an upcoming print issue of the journal, to assess the time course of antiHER2 gold nanoparticle cellular binding (Figure 2.7). We determined we could obtain substantially equivalent results to those obtained using conventional protocols after only five minutes which greatly expands the types of clinical applications possible. While completing this study, we observed two photon luminescence from layered gold

nanoparticles which had not been reported in the literature at this time we made this observation. We reported this work in a second paper in 2008 in *Nanotechnology* demonstrating for the first time the use of two photon microscopy for imaging immunotargeted (antiHER2) nanoshells. We believe using two photon imaging approaches may greatly aid in understanding biodistribution of gold nanoparticles in vivo by allowing 3D visualization of AuNPs within and surrounding tumors. Nuclear activation analysis (NAA) can provide high quality quantification of AuNPs in tissue but this is a destructive, bulk measurement method and does not allow visualization of AuNP location and distributions.

Project 3: Measurement of Radiation Dose Enabled by Nanoparticles

Project 3 is the most high risk/high yield project we proposed. The goal of the project is to investigate a strategy for real-time monitoring of delivered radiation dose rather than relying on computational modeling. Our task in Year 1 was to conduct a proof-of-principle study to assess whether our idea would work. We generated promising results concerning the potential of the overall idea: to leverage radiation breaking select bonds to cause loss of attached nanoparticles (and therefore, a measureable optical signal.) However, currently the strategy requires higher radiation dose than that used in clinical practice to work effectively. We will be conducting further experiments to determine whether it is possible to accomplish the same idea at clinically relevant radiation levels over the next year.

Adjuvant radiation (RT) therapy in breast cancer patients is effective in reducing local-regional recurrence, and in some patients, it can improve survival. Currently, RT dose given during treatment is calculated using computer modeling which have assumptions and at times differs from actual dose delivered. Therefore, it is crucial to measure the actual dose delivered to the tumor targets to ensure proper coverage. Measuring actual dose to surrounding normal tissue is also very important to determine risk of radiation-induced toxicities, such as secondary cancers. The ability to measure RT dose delivered to breast cancer and normal tissue in vivo with high 3-dimentional spatial resolution is currently unavailable and will greatly improve current techniques used in radiation therapy.

Megavoltage ionizing RT has been shown to fragment proteins, carbohydrates, and polymers by ionization and breakage of molecular bonds directly and through free radicals generated in aqueous solution indirectly. Studies on radioisotope-conjugated antibodies also observed loss of antibody binding due to ionizing RT in dose and time dependent manner. Therefore, we use nanoparticles conjugated to antibodies through radiation-sensitive linkers and measure RT dose delivered to the tissue by measuring the release of nanoparticles caused by RT-induced breakage of the conjugation. The general concept is that since nanoparticles conjugated with disease-specific antibody can be targeted to tumor cells with great efficiency, when we link the nanoparticle with antibodies through a radiation-sensitive linker and apply these immunotargeted nanoparticle to cancer cells or tumor tissue, we would expect to observe the release of

nanoparticles caused by loss of antibody binding after applying RT dose. We hope that by measuring the difference in concentration of nanoparticle binding and linker breakage, we can find some correlations between the releases of nanoparticles caused by radiation treatment to RT dose. We will also develop algorithms based on our experiments to accurately assess RT dose by measuring the optical signal and concentration of nanoparticles.

In year one of this project, we conducted in vitro studies and explored the applicability of using nanoparticle bioconjugates for RT dose measurement. We developed gold nanoshell probes conjugated with anti-HER2 antibody that specifically target HER2 overexpressed breast cancer cells. We also developed an IgG antigen and antibody based model to investigate the effects of RT treatment. By this method, we expect to relate the concentrations of nanoparticle released by RT treatment to the RT dose applied to the cells and develop algorithms to calculate the RT dose based on our experiments. Preliminary data in Figure 3.1 shows that there is obvious nanoshell loss after RT treatment of both 50Gy and 100Gy. The bright spots in the after-RT pictures of 100Gy are nanoshell aggregates due to the detachment of nanoparticles from the slides.   In contrast, for the no-RT control, the pre- and after- RT treatment images are quite similar to each other.

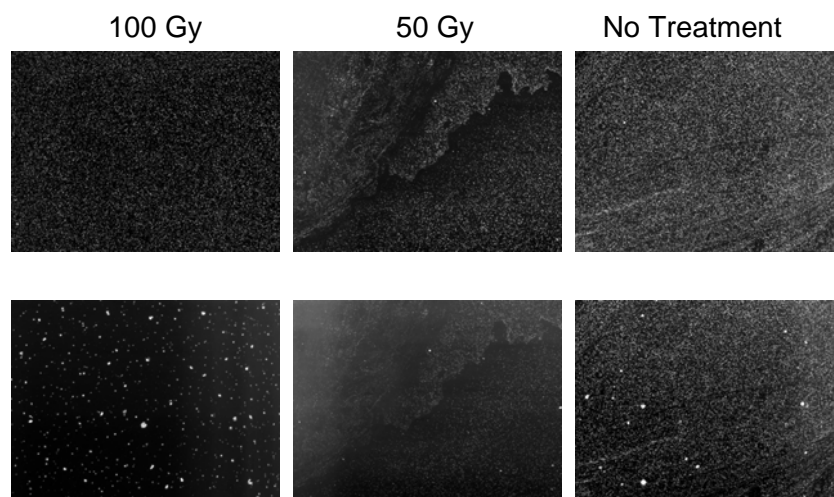| 100 Gy | 50 Gy | No Treatment |

Figure 3.1.   Darkfield images of IgG antigen treated slides incubated with gold nanoparticle and anti-IgG antibody conjugates, pre- (top row) and after- RT treatment (bottom row).   See text for explanation of results.

KEY RESEACH ACCOMPLISHMENTS

- Design of needle-based fiber optic imaging system completed and development of first generation system is ahead of schedule (Project 1)
- Demonstrated micron level resolution imaging using needle-compatible system (Project 1)
- Demonstrated system has the resolution and contrast to image individual cells (Project 1)
- Developed cadmium-free NIR qdots and demonstrated imaging benefits compared to conventional emissive nanomaterials (Project 2)
- Developed a synthesis method including scale up for gold nanorods (Project 2)
- Developed and published a method for quantifying gold nanomaterial cellular binding which will be broadly useful for evaluating gold materials developed in this project)
- Investigated how quickly we can achieve image contrast using antiHER2 gold nanomaterials and published these results (Project 2) demonstrating a 5 minute read out period is highly feasible (compared to the 60 minute read out used currently which is too long to be clinically feasible)
- Demonstrated two photon luminescence provides a potential contrast mechanism for targeted gold nanomaterials (Project 2) and published these results
- Demonstrated feasibility of nanotechnology-based optical scattering approach to radiation therapy direct dosimetry measurements although currently the level of radiation required for the approach to work is beyond what would be clinically feasible (Project 3)
- Worked with breast oncologists, surgeons, and pathologists to refine clinical applications and develop a process to move forward towards translation much work quickly than anticipated in the original SOW; in Year 2, we will request approval to changes in SOW so that additional tissue studies and, if possible, in vivo clinical trials can be completed during the time frame of the award
- Participated in the Breast Optical Imaging Working Group at MD Anderson Cancer Center to refine clinical strategies and will be attending this year's full Baylor College of Medicine Breast Cancer retreat as an invited speaker on the Era of Hope project to develop additional breast cancer collaborations to facilitate future clinical work
- First papers on work conducted as a part of this award have been published including joint work with the MD Anderson Cancer Center collaborators involved in the project

Reportable Outcomes

Journal Articles (acknowledging DOD Era of Hope Scholar support)

- Sun, J., Fu, F., Zhu, MQ, Bickford, L., Post, E., and <u>Drezek, R.</u> "Near-Infrared Quantum Dot Contrast Agents for Fluorescence Tissue Imaging: A Phantom Study." *Current Nanoscience.* Submitted. July 2008.

- Bickford, L., Chang, J., Fu, K., Sun, J., Hu, Y., Gobin, A., <u>Yu, TK</u>, and <u>Drezek, R.</u> "Evaluation of Immunotargeted Gold Nanoshells as Rapid Diagnostic Imaging Agents for HER2-Overexpressing Breast Cancer Cells: A Time-Based Analysis." *Nanobiotechnology.* Published online (5/13/2008). Print issue in press.

- Bickford, L., Sun, J., Fu, K., Lewinski, N., Nammalvar, V., Chang, J., <u>Drezek, R.</u> "Enhanced Multi-Spectral Imaging of Live Breast Cancer Cells Using Immunotargeted Gold Nanoshells and Two-Photon Excitation Microscopy." *Nanotechnology.* 19: 315102 (6pp) doi: 10.1088/0957-4484/19/31/315102 (2008).

- Fu, K., Sun, J., Bickford, L., Lin, A., Halas, N., <u>Yu, TK</u>, and <u>Drezek, R.</u> "Measurement of Immunotargeted Plasmonic Nanoparticle Cellular Binding: A Key Factor in Optimizing Diagnostic Efficacy." *Nanotechnology.* 19: 045103 (2008).

Abstracts

- Sun, J., Fu, F., Zhu, M-Q., Bickford, L., Post, E., and <u>Drezek, R.</u> "PbS Quantum Dots for Near-infrared Fluorescence Imaging." OSA 2008 Frontiers in Optics (FiO)/Laser Science XXIV Conference. Rochester, NY. 2008.
- <u>Drezek, R.</u> "Nanotechnology-Enabled Optical Molecular Imaging of Cancer." Department of Defense Breast Cancer Research Program Era of Hope Conference. Baltimore, MD. June 2008.
- Bickford, L., Chang, J., Fu, K., Sun, J., Hu, Y., <u>Yu, T.K.</u>, <u>Drezek R</u>. "Immunotargeted Nanoshells for Point of Care Diagnostic Applications." Biomedical Optics. St. Petersburg, FL. March 2008.

Invited Presentations

- Nanotechnology-Enabled Optical Molecular Imaging of Breast Cancer. Baylor College of Medicine Breast Center Annual Retreat. 2008.
- Nanotechnology-Enabled Optical Molecular Imaging of Cancer. Department Seminar. Duke University Fitzpatrick Optics Institute. 2008-2009 seminar series.
- Rice/Texas Medical Center Translational Research in Optical Molecular Imaging of Cancer. Rice University President's House "Something New for Lunch" Lecture. 2008.

- Nanotechnology-Enabled Optical Molecular Imaging of Cancer. Department Seminar. University of Rochester. 2008-2009 seminar series.
- Applications of Gold Nanoparticles in Cancer Diagnostics. IEEE LEOS Summer Topical Conference: Advances in Nanobiophotonics. Mexico. July 2008.
- Applications of Gold Nanoparticles in Cancer Diagnostics. American Society of Photobiology Annual Meeting. June 2008.
- Optically Activated Nanoparticles for Imaging and Therapy of Cancer. Department Seminar. Beckman Laser Institute, University of California at Irvine. March 2008.
- Optically Activated Nanoparticles for Imaging and Therapy of Cancer. Department Seminar. Rutgers Department of Bioengineering. March 2008.
- Optically Activated Nanoparticles for Imaging and Therapy of Cancer. Department Seminar. University of Washington. Nanotechnology Seminar Series. February 2008.
- Optically Activated Nanoparticles for Imaging and Therapy of Cancer. Department Seminar. MD Anderson Cancer Center Radiology Department. February 2008.
- Hot Topic Nanomedicine Workshop. SPIE Photonics West. San Jose, CA. January 2008.
- Biomedical Applications of Quantum Dots. SPIE Photonics West. San Jose, CA. January 2008.
- Nanotechnology Enabled Optical Imaging of Cancer. The Materials/Biology Interface. Material Research Society (MRS) Annual Meeting. Boston, MA. November 2007.
- Needle Compatible Fiber Probe for Optical Imaging of Cancer. Department of Interventional Radiology. November 2007.
- Nanotechnology Enabled Molecular Targeted Optical Imaging of Cancer. Department Seminar. University of Texas at Austin. October 2007.
- Nanotechnology Enabled Optical Imaging of Cancer. United States/France Nanomedicine Symposium. October 2007.

Conclusion

Over the first twelve months of the award, we have initiated work on all three projects described in the Statement of Work. All tasks slated for Year 1 have been completed on time or ahead of schedule. Our work in Year 1 has focused on laying the foundations for the more clinically directed efforts which will occur in future years. We have designed and constructed our first prototype imaging system for in vivo imaging of breast cancer with micron resolution, a technology we believe will offer an important complementary approach to conventional macroscopic imaging methods. We have begun work on the two new classes of nanomaterials we will work pursue and continued work on an existing class of gold nanostructures. We have conducted initial experiments to examine feasibility of a high risk/ high gain strategy for monitoring radiation therapy.

The breast cancer clinical community has been extremely encouraging of the technologies we are developing. We have been working closely with closely with breast oncologists, pathologists, and surgeons at MD Anderson Cancer Center to more carefully define the specific clinical applications to be pursued. Based on their recommendations and insights gained at this year's Era of Hope meeting, we will seek approval over the next year for specific changes to the Statement of Work which will enable the project to move forward more rapidly towards translational applications including, if possible, a clinical trial. This will be possible because we are substantially ahead of schedule in system development. Because I was relatively new to breast cancer research at the time I submitted the proposal, a number of general ideas were put forward in the initial proposal regarding how the type of technologies we are developing might influence breast cancer clinical care. We have now established three specific clinical applications. This will require approval of changes to our Statement of Work as well as regulatory approvals of the necessary tissue/clinical protocols. In anticipation of this process, we have already submitted and gained approval through both the Rice University and MDACC IRBs for our work. Our next step will be submitting a modified Statement of Work for approval, and, if approved, submitting to DOD our regulatory paperwork. If not possible, we will continue as scheduled with our current SOW. The specific clinical applications of our technologies we intend to pursue are as follows:

- use of the needle-based fiber optic probe to aid in biopsy site selection and lymph node assessment (building on Project 1 in current SOW)
- intraoperative tumor margin evaluation of HER2+ patients using immunotargeted gold nanoparticles (building on imaging agents under development in Project 2 of current SOW)
- monitoring efficacy of radiation treatment of inflammatory breast cancer using a non-contact optical imaging system (building on Project 3 goal to monitor radiation therapy)

We are presently continuing our work based on the SOW as now specified but will determine which direction modifications may be possible this fall.

References

[1] Sausville, Edward A. and Longo, Dan L.: Principles of Cancer Treatment: Surgery, Chemotherapy, and Biologic Therapy in [Harrison's Principles of Internal Medicine](), 16th Ed. Kaspar, Dennis L. et al., editors. p.446 (2005)

[2] Ward, DE and Sapecki, R. "Innocent Bystanders or Partners in Crime." Ohio State University Frontiers Magazine Archive 2005; accessed online. http://www.jamesline.com/news/publications/frontiers/archives/?ID=1570&CID=0

[4] Ross MH, Romrell LJ, Kaye GI. Histology A Text and Atlas. Third ed. Baltimore: Williams & Wilkins, 1995.

[3] Bancroft JD, Gamble M, editors. Theory and Practice of Histological Techniques, 5th edition. Edinburgh: Churchill Livingstone, 2002.

[5] Parker SH, Lovin JD, Jobe WE, et al. Stereo-tactic breast biopsy with a biopsy gun. Radiology 1990; 176:741-747.

[6] Parker SH, Jobe WE, Dennis MA, et al. US-guided automated large-core biopsy. Radiology 1993; 187:507-511.

[7] Schueller G, Jaromi S, Ponhold L, et al. US-guided 14-gauge core-needle breast biopsy: results of a validation study in 1352 cases. Radiology 2008; 248(2); 406-413.

[8] Dowlatshahi K, Jokich PM, Schmidt R, Bibbo M, Dawson PJ. Cytologic diagnosis of occult breast lesions using steriotaxic needle aspiration. Arch. Surg. 1987; 122: 1343-1346.

[9] The Uniform Approach to Breast Fine-Needle Aspiration Biopsy (adopted from proceedings of a NCI sponsored conference in 1996). Am. J. Surg. 1997; 174: 371-385.

[10] Barra A, Gobbi H, Rezende CA, et al. A Comparison of Aspiration Cytology and Core Needle Biopsy According to Tumor Size of Suspicious Breast Lesions. Diagn. Cytopathol. 2007; 36(1): 26-31.

[11] Dowlatshahi K, Yaremko ML, Kluskens LF, and Jokich PM. Nonpalpable Breast Lesions: Findings of Stereotaxic Needle-Core Biopsy and Fine-Needle Aspiration Cytology. Radiology 1991: 181:745-750.

[12] Spaner SJ and Warnock GL. A brief history of endoscopy, laparoscopy, and laparoscopic surgery. J Laparoendosc Adv Surg Tech A. 1997 Dec;7(6):369-373.

[13] Flusberg BA, Cocker ED, Piyawattanametha WP, Jung JC, Cheung ELM, and Schnitzer MJ. Fiber-optic fluorescence imaging. Nat. Methods 2005;2:941-950.

[14] Kimura S and Wilson T. Confocal scanning optical miscroscope using single-mode fiber for signal detection. Appl. Opt. 1991;30:2143-2150

[15] Delaney PM, Harris MR, and King RG. Fibre-optic laser scanning confocal microscope suitable for fluorescence imaging. Appl. Opt. 1994;33:573-577.

[16] Dickensheets DL and Kino GS. Micromachined scanning confocal optical microscope. Electron Lett 1991;27:724-726

[17] Liu JTC, Mandella MJ, Ra H, Wong LK et al. Miniature near-infrared dual-axes confocal microscope utilizing a two-dimensional microelectromechanical systems scanner. Opt Lett. 2007;32:256-258.

[18] Shin HJ, Pierce MC, Lee D, Ra H, Solgaard O, and Richard-Kortum R. Fiber-optic confocal microscope using a MEMS scanner and miniature objective lens. Opt Express 2007;15:9113-9122.

[19] Seibel EJ and Smithwick QYJ. Unique Features of Optical Scanning, Single Fiber Endoscopy. Lasers Surg Med 2002;30:177-183

[20] Polglase AL, McLaren WJ, Skinner SA, Kiesslich R, Neurath MF, and Delaney PM. Fluorescence confocal endomicroscope for in vivo microscopy of the upper and lower gastrointestinal tract. Gastrointest Endosc 2005;62:686-695.

[21] Kiesslich R, Goetz M, Vieth M, Galle PR, and Neurath MF. Technology Insight: confocal laser endoscopy for in vivo diagnosis of colorectal cancer. Nat Clin Pract Oncol 2007;4:480-490.

[22] Harris MR. UK patent 2001:GB2340332B.

[23] Yelin D, Rizvi I, White WM et al. Three-dimensional miniature endoscopy. Nature 2006;443:765.

[24] Gmitro AF and Aziz DJ. Confocal microscopy through a fiber-optic imaging bundle. Opt. Lett. 1993;18:565-567.

[25] Sumitomo Electric. Silica Image Guide for Fiberscope. Proprietary Technical Document 2008.

[26] Juskaitis R, Wilson T, and Watson TF. "Real-time white light reflection confocal microscopy using a fibre-optic bundle" Scanning 1997;19:15-19.

[27] Liang C, Descour M, Sun KB, and Richards-Kortum R. Fiber confocal reflectance microscope (FCRM) for in-vivo imaging. Opt. Express 2001;9:821-830.

[28] Jean F, Bourg-Heckly G, and Viellerobe B. Fibered confocal spectroscopy and multicolor imaging system for in vivo fluorescence analysis. Opt. Express 2007;15:4008-4017.

[29] Dubaj V, Mazzolini A, Wood A, and Harris M. Optic fibre bundle contact imaging probe employing a laser scanning confocal microscope. J. Microsc. 2002;207:108-117.

[30] Sabharwal YS, Rouse AR, Donaldson L, Hopkins MF, and Gmitro AF. Slit-Scanning Confocal Microendoscope for high-Resolution In Vivo Imaging. Appl. Opt. 1999;38:7133-7144.

[31] Muldoon TJ, Pierce MC, Nida DL, Williams MD, Gillenwater A, and Richards-Kortum R. Subcellular-resolution molecular imaging within living tissue by fiber microendoscopy. Opt. Express 2007;15(25):16413-16423.

[32] Oppenheim AV, Wilsky AS, and Hamid S. Signals and Systems, 2nd Ed. New Jersey: Prentice Hall; 1996.

[33] Oppenheim AV, Schafer RW, and Buck JR. Discrete-Time Signal Processing, 2nd Ed. New Jersey: Prentice Hall 1999.

[34] Laemmel E, Genet M, Le Goualher G, Perchant A, Le Gargasson JF, and Vicaut E. Fibered confocal fluorescence microscopy (Cell-viZio) facilitates extended imaging in the field of microcirculation.   A comparison with intravital microscopy.   J. Vasc. Res. 2004;41:400-411.

[35] Delaney P and Harris M. Handbook of Biological Confocal Microscopy, 3rd Ed. New York: Springer 2007.

[36] Wahlby C, Sintorn IM, Erlandsson F, and Bengtsson E. Combining intensity, edge and shape information for 2D and 3D segmentation of cell nuclei in tissue sections.   J Microsc

2004;215:67-76.

[37] Sahoo PK, Soltani S, Wong AKC, and Chen YC. A survey of thresholding techniques. Comp. Vision, Graphics Image Proc. 1988;41:233-260.

[38] Krtolic A, Ortiz de Solorzano C., Lockett S, and Campisi J. Quantification of epithelial cells in coculture with fibroblasts by fluorescence image analysis. Cytometry 2002;49:73-82.

[39] Lindblad J and Bengtsson E. A comparison of methods for estimation of intensity nonuniformities in 2D and 3D microscope images of fluorescence stained cells. Proceedings of the 12th Scandinavian Conference on Image Anlysis (SCIA), Norway. NOBIM;264-271.

[40] Ortiz de Solorzano C, Garcia Rodriguez E, Jones A et al. Segmentation of confocal microscope images of cell nuclei in thick tissue sections. J Microsc 1999;193:212-226.

[41] Beucher S and Lanteujoul CH. Use of watersheds in contour detection. Int. Workshop on Image Processing: Real-Time and Motion Detection/Estimation, Rennes, France. IRISA Report 1979;132.

[42] Meyer F and Beucher S. Morphological Segmentation. J Vis Comm Image Report 1990;1:21-46.

[43] Vincent L. Morphological grayscale reconstruction in image analysis: applications and efficient algorithms. IEEE Trans. Image Processing 1993;2:176-201.

[44] Beucher S. The watershed transformation applied to image segmentation. Scanning Microsc 1992;6:299-314

[45] Lockett SJ, Sudar D, Thompson CT, Pinkel D, and Gray JW. Efficient, interactive, and three-dimensional segmentation of cell nuclei in thick tissue sections. Cytometry 1998;31:275-286.

[46] Stoev SL and Straaer W. Extracting regions of interest applying local watershed transformation. Proceedings of IEEE Visualization 2000, Salt Lake City;21-29.

[47] Landini G and Othman IE. Estimation of tissue layer level by sequential morphological reconstruction. J Microsc 2003;209:118-125.

[48] Baggett D, Nakaya M, McAuliffe M, Yamaguchi T, and Lockett S. Whole Cell Segmentation in Solid Tissue Sections. Cytometry Part A 2005;67(A):137-143

[49] Dreyfus S. Richard Bellman on the birth of dynamic programming. Operations Research 2002;50(1):48-51.

[50] Bellman R, 1957, *Dynamic Programming*, Princeton University Press. Dover paperback edition (2003),

[51] Bertsekas, D. P., 2000. *Dynamic Programming and Optimal Control, Vols. 1 & 2*, 2nd ed. Athena Scientific.

[52] Montanari U. On the optimal detection of curves in noisy pictures. Commun ACM 1971;14:335-345.

[53] Verwer BJH, Verbeek PW, and Dekker ST. An efficient uniform cost algorithm applied to distance transforms. IEE Trans Pattern Anal Mach Intell 1989;11:425-429.

[54] Geusebroek J-M, Smeulders AWM, and Geerts H. A minimum cost approach for segmenting networks of lines.   Int J Comput Vis 2001;43:99-111.

[55] Kampe T and Kober R. Nonparametric Image segmentation. Pattern Anal Appl

1998;1:145-154.

[56] Zeng A, Staib LH, Schultz RT, Tagare H, Win L, and Duncan JS. A new approach to 3D sulcal ribbon finding from MR images. Medical image computing and computer-assisted intervention, MICCAI'99 Proc. Lect Notes Comput Sci 1999;1679:148-157.

[57] McCullough DP, Gudla PR, Harris BS et al. Segmentation of whole cells and cell nuclei from 3-D optical microscope images using dynamic programming. IEEE Transactions on Medical Imaging 2008;27(5):723-734.

[58] Duda RO and Hart PE. Use of the Hough Transformation to Detect Lines and Curves in Pictures. Comm. ACM 1972;15:11-15.

[59] Shapiro L and Stockman G. Computer Vision. New Jersey: Prentice Hall; 2001.

[60] Mouroutis T, Roberts SJ, and Bharath AA. Robust cell nuclei segmentation using statistical modeling. Bioimaging 1998;6(2):79-91.

[61] Uchino E, Yamakawa T, and Hirakawa K. Effective detection of nucleus in cytodiagnosis by employing combinatorial fuzzy hough transform. J Intell Fussy Syst 1997;5(4):333-343.

[62] Garrido A and de la Blanca NP. Applying deformable templates for cell image segmentation. Pattern Recognition 2000;33(5):821-832.

Near-Infrared Quantum Dot Contrast Agents for Fluorescence Tissue Imaging: A Phantom Study

Running title: NIR quantum dots for fluorescence tissue imaging: a phantom study

Jiantang Sun[1, 3], Kun Fu[2, 3], Ming-Qiang Zhu[1], Lissett Bickford[1],

Eric Post[4], and Rebekah Drezek[1, 2, *]

[1]*Departments of Bioengineering,* [2]*Electrical and Computer Engineering and* [3]*Rice Quantum*

Institute,

Rice University, 6100 Main Street, Houston, TX 77005, USA

[4]*Biomedical Engineering,*

Louisiana Tech University, 818 Nelson Avenue, Ruston, LA 71270, USA

Email: drezek@rice.edu

(713) 348-3011 (office)

(713) 348-5877 (fax)

Abstract

Due to their small size and red-shifted excitation and emission bands, lead sulfide (PbS) near-infrared (NIR) quantum dots (QDs) possess promising enhancements to *in vivo* tumor optical imaging applications. In this phantom-based study, we correlated PbS NIR QD concentrations to feasible imaging depths. A fluorescence imaging system (FIS) was used to acquire images of QD-filled tumor models, which were embedded in liquid tissue phantoms. For the lowest tested concentration of 200 nM, PbS-QD-filled tumor models could be imaged at a tissue phantom depth of 15 mm. In addition, the FIS was used to compare the imaging potential of PbS QDs to quantum dots that fluoresce in the visible spectral range. Results indicated that tumor models with photons emitted in the NIR region can be imaged with less distortion than those with photons emitted in the visible spectrum. As the phantom thickness over the tumors was increased from 0 to 1.75 mm, the half-intensity widths of normalized fluorescence images produced by red QDs (acquired peak at ~645 nm) increased by ~300%; for NIR QDs (acquired peak at ~880 nm), the widths increased by ~140%. Due to the decreased scattering effect of the tissue phantoms in the NIR spectral range, the margins of PbS QD images were better defined than those of the corresponding red images.

Key Words: Near-infrared, quantum dot, fluorescence, optical imaging, phantom

Abbreviations

PbS: lead sulfide; NIR: near-infrared; QDs: quantum dots; FIS: fluorescence imaging system; TEM: transmission electron microscopy; UV: ultraviolet; PBS: phosphate buffered saline; TBR: tumor-to-background ratio; Em: emission; Ex: excitation

1. Introduction

A "therapeutic window" exists in the spectral region of 700 to 1200 nm which allows near-infrared (NIR) light to penetrate several centimeters into human tissue [1-4]. Recently, the development of various NIR fluorescence contrast agents has greatly promoted the application of NIR fluorescence biomedical imaging techniques [4-6]. Among those strategies employing fluorescence contrast agents, the use of lead sulfide (PbS) NIR quantum dots (QDs) is expected to yield promising results for *in vivo* imaging applications. PbS QDs are nanometer-size, core-shell semiconductor structures that possess a strong emission peak in the NIR region [6-8]. With specific surface-modification, the water solubility and biocompatibility of PbS QDs can be greatly enhanced [9]. Since the emission peak of these quantum dots can be easily tuned to the desired wavelength by tailoring the particle size, PbS QDs can provide great emission band flexibility for *in vivo* NIR tissue imaging applications [5-7, 9, 10].

Since the introduction of quantum dots in the late 1970s, numerous reports have been published that examine the use of these nanoparticles as fluorescence imaging contrast agents [6, 8, 11-13]. Compared to quantum dots that fluoresce in the visible spectral range, PbS NIR QDs have their own unique properties for *in vivo* deep tissue fluorescence imaging applications [2, 6-8, 14]. As reported in previous publications, for PbS QDs that have an emission peak at ~1010 nm, the average particle size is ~4 to 5 nm before surface modification; after surface modification, particles show no significant increase in size when observed by transmission electron microscopy (TEM) [9]. Therefore, it is believed that the relatively small size of PbS QDs will facilitate body clearance of these particles during clinical trials [15]. Additionally, the corresponding

excitation spectrum of these QDs spans the range from visible to NIR [7, 9, 10], and the emission peak of PbS QDs can be systematically tuned in the near-infrared spectral range. Thus, both the relatively red-shifted emission peak and wide excitation band provide flexibility in the choice of proper working wavelength regions; this will, in turn, avoid most of the effects of tissue autofluorescence [16, 17].

A bandpass excitation filter of 671 to 705 nm was selected for the depth-resolved tissue phantom experiments discussed below. This range avoids the major absorption peaks of intrinsic auto-fluorophores, and therefore permits improved illumination into the samples [16-19]. In this experiment, the fluorescence spectrum of the excited PbS QDs peaks at a wavelength of ~880 nm when acquired with a Maestro imaging system (CRi, Woburn, MA). Under these conditions, the NIR quantum dot signal can be easily distinguished from tissue autofluorescence background [16] and images with improved contrast can then be obtained. Furthermore, in comparison with visible QDs, the minimum absorption and scattering coefficients of tissue samples in the NIR region allow photons emitted from PbS QDs to propagate deeper into tissue [1, 2]. Also, images of PbS-QD-filled tumor models embedded in tissue phantoms exhibit little blurring at tumor margins due to the reduced scattering effect.

A previous publication has shown the possibility of using bioconjugated PbS QDs as NIR contrast agents for specifically targeted molecular imaging applications [20]. As a step towards *in vivo* tissue fluorescence screening using PbS NIR quantum dots and the Maestro imaging system, a tissue phantom study was carried out to identify and evaluate the imaging potentials of these NIR nanocrystals and to acquire a basic understanding of the contrast agent concentrations required to obtain clear and acceptable images.

Moreover, the imaging advantages of NIR QDs have been assessed against QDs that fluoresce in the visible spectral range.

2. Methods

2.1. NIR quantum dot fabrication and surface modification

The lead sulfide NIR QDs used in this study were synthesized [7, 9, 10] and surface modified in accordance with methods presented in previous publications [6, 8, 9]. The NIR fluorescence peak of these PbS quantum dots can be tailored to the desired imaging wavelength range and optimized for the imaging system employed [7, 9].

2.2. Tissue phantom and tumor models

Human tissue is a highly turbid media with strong absorption and scattering effects in the ultraviolet (UV) and visible spectral regions [1, 16, 21]. However, it is within the NIR wavelength region of 700 to 1200 nm where most biomolecular absorption coefficients reach their minimum values [1, 2, 5, 16, 22]. To study light propagation and distribution in human tissue, various phantoms have previously been developed that simulate tissue optical properties within the visible and NIR spectral regions [21, 23]. In the following experiments, tissue phantoms composed of 1% Liposyn solutions (Abbot Labs, North Chicago, IL) were used to mimic the absorption and scattering properties of human breast tissue [21, 23-25].

Two types of experimental phantom setups were employed. First, different concentrations of PbS-QD filled cylindrical 20 × 8 mm glass vials were embedded in a 1% Liposyn phantom. By changing the volume of the Liposyn solution, tumors with different QD concentrations can be imaged at various phantom thicknesses (Figure 1). This procedure was used to provide insight into the possibility of using PbS QDs for deep

5

tissue imaging, as well as impart a fundamental understanding of the contrast agent concentrations required for sufficient tumor image acquisition at various depths.

Second, a phantom-filled transparent container was placed above a 384-well microplate (Greiner Bio-one North America, Inc.) which has 3.7×3.7 mm square wells that were used to house quantum dot suspensions (see Figure 2). Two adjacent wells were filled, respectively, with CdSe/CdS red quantum dots and PbS NIR quantum dots of the same concentration (~1 μM) and same volume (100 μL/well). Using the Maestro imaging system, fluorescence images of tumor models with both the red QDs (acquired emission peak at ~645 nm) and the NIR QDs (acquired emission peak at ~880 nm) were analyzed. This procedure was used to obtain specific data about the blurring effect associated with using the tumor margin model for each type of QD, which was assessed by varying phantom thickness (Figure 2).

The second phantom setup was used to simulate relatively small tumor tissue embedded close to the superficial skin. To simultaneously image visible and NIR QDs, an excitation band of lower wavelengths was necessary. As a result of using lower wavelengths, the excitation photons could not penetrate deep into the tissue phantom. In addition, a strong autofluorescence background was associated with this excitation band. To minimize the influences of the excitation light, a superficial phantom setup was needed. Moreover, the 384-well microplate provided well-defined square geometries and sharp edges, which were necessary for the blurring-effect component of the study.

2.3. Fluorescence image acquisition and processing

A Maestro imaging system equipped with proper filter sets (CRi, Woburn, MA) was used to acquire all the fluorescence images in this report. The working wavelength ranges of all the filters used were provided by the Maestro imaging system if not specified. Table 1

summarizes the filter sets that were used in the study. With the advantages of multispectral acquisition and quantitative data analysis, this system can provide improved imaging flexibility and sensitivity [26]. Therefore, the fluorescence signals from phantom autofluorescence, red QDs, and NIR QDs can be effectively separated from the stack of wavelength-resolved fluorescence images. To further evaluate the dimensions of the image of each square well of QDs, as described in the previous section (Figure 2), post-acquisition image processing was performed using MatLab codes.

3. Results

Four cylindrical 20×8 mm glass vials were filled with 0.2 μM, 0.4 μM, 1 μM, and 2 μM PbS quantum dots suspended in phosphate buffered saline (PBS), respectively. For the condition in which there was no phantom above these vials (see Figure 1), fluorescence images of all four samples were obtained under the exact same acquisition conditions using the fluorescence imaging system. The average signal intensity of the acquired images of each vial of QDs was then extracted using the Maestro image processing program. To assess the influences of acquisition time and quantum dot concentration on the average signal intensities, NIR fluorescence images were taken in a series and then processed. As shown in Figures 3a and 3b, the average QD image intensity increased linearly as the QD concentration increased. Additionally, the slope also increased linearly as the acquisition time increased for images obtained with acquisition times of 100 ms, 200 ms, and 300 ms. The imaging results show that these same quantum dot image intensities can be affected by the particular applied excitation band [9]. Specifically, Figures 3a and 3b show the differences that result from their excitation bands, since the same 700 nm longpass emission filter was utilized. An excitation band from 615 to 665 nm was used for Figure 3a, whereas the corresponding excitation band for Figure 3b ranged from 575 to 605 nm.

To evaluate the PbS QD concentration needed for an acceptable image at different tissue depths, the thickness of the phantom above each NIR tumor model was systematically varied (Figure 1). For the visible and near-infrared spectral ranges, the wavelength-dependent reduced scattering coefficient of the 1% Liposyn tissue phantom, as shown in Figure 4, was obtained from previous literature [24, 25, 27-29]. The corresponding absorption coefficient was dominated by water absorption, which varies from 0.001 to 0.3 cm^{-1} [24, 27, 30]. To demonstrate potential *in vivo* tissue diagnostic applications, the imaging process was optimized by using a bandpass excitation filter of 671 to 705 nm (deep-red excitation filter) coupled with a 750 nm longpass emission filter (deep-red emission filter) to acquire the fluorescence images of PbS-QD-filled tumor models. The average QD image intensity and quality both decreased with increasing phantom thickness. To assess image quality, the tumor-to-background ratio (TBR) was evaluated; similar to that described by Adams et al. [31], TBR is defined as the ratio of the average tumor region intensity to the average background region intensity. A TBR threshold value of 1.22 was used to distinguish acceptable images from unacceptable ones. Clear fluorescence images (TBR>1.22) of both 1 μM and 2 μM quantum dot suspensions were obtained at a phantom thickness of 25 mm with an acquisition time of 900 ms. However, even with the same imaging conditions, a clear QD image (TBR>1.22) could only be acquired at a phantom thickness of less than 20 mm for the 0.4 μM quantum dots. As for the 0.2 μM QD tumor model, reasonable images could not be obtained when the phantom was thicker than 15 mm. The normalized average QD image intensities at various concentrations are shown in Figure 5. These normalized average image intensities were obtained by subtracting the average background region intensities from the average tumor region intensities. Although the maximum imaging depths for different concentrations of QDs vary considerably, their normalized average image

intensities have the same decreasing trend when plotted as a function of phantom thickness (Figure 5).

To compare the imaging properties of visible quantum dots and near-infrared quantum dots, the second experimental phantom setup (see Figure 2), as described in the methods section, was employed. The normalized fluorescence spectra of both CdSe/CdS (red) and PbS (NIR) quantum dots obtained under the same excitation and imaging conditions are shown in Figure 6. A green bandpass excitation filter of 503 to 555 nm and a 600 nm longpass filter were used in tandem to simultaneously obtain the fluorescence images of both types of quantum dots. After spectral unmixing [26], CdSe/CdS (red) and PbS (NIR) quantum dot images can be isolated from each other as well as from the phantom autofluorescence. A series of fluorescence images, after the spectral unmixing processing for both the red and the NIR Qds, is shown in Figure 7. Initially, when there are no phantoms above the QDs, clear images of the square wells can be acquired, and the image size of these wells is almost exactly the same for both kinds of QDs. As the phantom thickness gradually increased, the average intensities decreased for both kinds of quantum dot fluorescence images, a finding which agrees with previous results. Notably, the images of the red QDs are larger and less distinct than those of the NIR QDs, even though they are obtained under the same conditions. To compare the enlarging and blurring effects of these two different types of QDs as a function of the phantom thickness, a section line was drawn for each fluorescence square well in Figure 7. This section line goes directly through the center of every square well image and splits it into two equal rectangular parts. The normalized fluorescence intensity along the section line was plotted as a function of pixel position. Based on the data in Figure 8, it can be observed that when the phantom thickness increased from 0 to 1.75 mm, the half-intensity widths of the red-QD-filled wells expanded by ~300%, while those of the NIR-

QD-filled wells expanded by only ~140%. Moreover, the margins of the NIR-QD-filled wells were better defined than the margins of the red-QD-filled wells.

4. Discussion and Conclusions

The phantom results indicate that lead sulfide NIR quantum dots possess essential properties for fluorescence imaging applications. Increasing either the concentration of QDs used or the image acquisition time can enhance collected image intensities. When PbS QDs are directly excited with yellow or red light and imaged with the Maestro system, clear fluorescence images can be obtained with the lowest tested concentration of 200 nM and the lowest tested acquisition time of 100 ms. In addition to these two factors, PbS QD fluorescence image intensity is also influenced by the excitation light band used (Figure 3). Since tissue absorption and scattering effects are heavily wavelength-dependent [2, 16, 21], an optimized excitation band should be carefully chosen before PbS QDs are used for NIR tissue imaging applications.

For the results shown in Figure 5, clear NIR images were obtained with the lowest tested PbS QD concentration of 200 nM at the phantom depth of 15 mm when imaged with an acquisition time of 900 ms and deep-red excitation and emission filter sets. The red-shifted excitation band of 671 to 705 nm maximizes the illumination penetration depth into the tissue phantom, and the 750 nm longpass emission filter eliminates most phantom autofluorescence. Both factors improved image quality at relatively deep tissue sites. The optimal excitation and emission wavelengths for PbS QD fluorescence imaging were determined using a step-by-step approach. First, the emission wavelengths were selected to be in the NIR region. This region was selected because both tissue absorption and scattering coefficients are minimal in the NIR. For our imaging system, and with the use of PbS QD contrast agents, the optimal emission band of 750 to 950 nm was chosen.

Then the optimal excitation wavelengths were selected based on the aforementioned emission band. There were three excitation filters available: one with an excitation band of 575 to 605 nm, a second with 615 to 665 nm, and a third with 671 to 705 nm. The 575 to 605 nm filter was eliminated because it induced a strong autofluorescence background. Although tissue phantom autofluorescence induced by the 615 to 665 and 671 to 705 nm filters were similar to each other, the 671 to 705 nm excitation band resulted in less tissue scattering. The optimal excitation wavelength range of 671 to 705 nm was finally chosen in conjunction with the optimal emission band of 750 to 950 nm. As shown in Figure 5, although the QD concentration and the imaging depth vary over a wide region, the normalized average image intensity for each assessed concentration possesses the same variable trend with respect to the corresponding increase in tissue phantom depth.

Another advantage of using PbS QDs for tissue imaging applications is their red-shifted emission wavelengths in the NIR region. As previously reported, tissue absorbs and scatters NIR light less than UV or visible light [2, 24, 32]. Therefore, most of the NIR emission photons from PbS QDs will pass through the phantom with only a few scattering events and be detected by the camera [1, 17, 33]. This reduced scattering effect will potentially result in an important property of NIR QD imaging: improved margin delineation.

The ability to obtain better-confined tumor images significantly impacts both cancer diagnosis and surgery [34-37]. Currently, surgeons excise both the suspected malignant tumor tissue and the benign tissue surrounding the tumor site to ensure elimination of cancer cells. Aside from causing the patient pain and suffering, this procedure requires extensive recovery time [34-37]. However, if the tumor could be imaged with improved

clarity during surgery, for example, with the potential help of bioconjugated PbS NIR QDs, the required tissue excision would be greatly reduced, with promising benefits for both patients and physicians [34-37].

As shown in Figure 7, as the phantom thickness increases, the images of the NIR-QD-filled square wells demonstrate better-defined margins than those of the red-QD-filled wells. In addition, the images of the red wells with a 1.75 mm phantom are much larger than their initial images taken without a phantom, even though both were obtained under the same imaging conditions. In contrast, the corresponding images of the NIR wells are similar in size regardless of phantom presence. It is believed that the wavelength-dependent phantom optical properties may be one of the most important factors that result in these different red and NIR images.

Although the experimental results shown in Figure 7 are promising, there may be concerns about the green excitation band (503 to 555 nm) used and the maximum imaging depth achieved. A green filter is used for excitation only because we wanted to simultaneously excite both the red and NIR QDs and compare the images obtained under the same conditions. With the fluorescence imaging system, a red (615 to 665 nm) or deep-red (671 to 705 nm) excitation band is typically recommended for deep tissue PbS NIR QD imaging because this band maximizes illumination penetration and, simultaneously, avoids the excitation of most tissue autofluorescence. The maximum phantom depth of 1.75 mm was applied in the above experiments because we can obtain reasonable images from both the red and NIR QDs at that depth.

In conclusion, a phantom study in which PbS QDs are used as contrast agents for fluorescence imaging applications is reported. The experiments show that lead sulfide

NIR quantum dots possess enhanced fluorescence imaging properties. When collected with the deep-red excitation and emission filter set, adequate NIR QD fluorescence images were obtained with a maximum tissue phantom thickness of 15 mm at a particle concentration of 200 nM and an acquisition time of 900 ms. Moreover, the greatly improved tumor margin confinement images obtained from PbS QD contrast agents, as explained above, are indicative of their promising surgical applications for future *in vivo* tumor detection.

Acknowledgements

References

[1] Wilson, B.C.; Jacques, S.L. *IEEE J. Quantum Electron.*, **1990**, *26*, 2186.

[2] Cheong, W.F.; Prahl, S.A.; Welch, A.J. *IEEE J. Quantum Electron.*, **1990**, *26*, 2166.

[3] Pogue, B.W.; Geimer, S.; McBride, T.O.; Jiang, S.; Osterberg, U.L.; Paulsen, K.D. *Appl. Opt.*, **2001**, *40,* 588.

[4] Kim, S.; Lim, Y.T.; Soltesz, E.G.; De Grand, A.M.; Lee, J.; Nakayama, A.; Parker, J.A.; Mihaljevic, T.; Laurence, R.G.; Dor, D.M.; Cohn, L.H.; Bawendi, M.G.; Frangioni, J.V. *Nature Biotechnol.*, **2004**, *22,* 93.

[5] Cai, W.; Shin, D.-W.; Chen, K.; Gheysens, O.; Cao, Q.; Wang, S.X.; Gambhir, S.S.; Chen, X. *Nano Lett.*, **2006**, *6*, 669.

[6] Michalet, X.; Pinaud, F.F.; Bentolila, L.A.; Tsay, J.M.; Doose, S.; Li, J.J.; Sundaresan, G.; Wu, A.M.; Gambhir, S.S.; Weiss, S. *Science*, **2005**, *307*, 538.

[7] Hines, M.A.; Scholes, G.D. *Adv. Mater.*, **2003**, *15*, 1844.

[8] Medintz, I.L.; Uyeda, H.T.; Goldman, E.R.; Mattoussi, H. *Nature Mater.*, **2005**, 435.

[9] Zhu, M.-Q.; Chang, E.; Sun, J.; Drezek, R.A. *J. Mater. Chem.*, **2007**, *17*, 800.

[10] Bakueva, L.; Gorelikov, I.; Musikhin, S.; Zhao, X.S.; Sargent, E.H.; Kumacheva, E. *Adv. Mater.*, **2004**, *16*, 926.

[11] Clapp, A.R.; Medintz, I.L.; Mauro, M.; Fisher, B.R.; Bawendi, M.G.; Mattoussi, H. *J. Am. Chem. Soc.*, **2004**, *126*, 301.

[12] Bruchez, M.J.; Moronne, M.; Gin, P.; Weiss, S.; Alivisatos, A.P. *Science*, **1998**, *281*, 2013.

[13] Medintz, I.L.; Clapp, A.R.; Mattoussi, H.; Goldman, E.R.; Fisher, B.; Mauro, J.M. *Nature Mater.*, **2003**, *2*, 630.

[14] Choi, J.; Wolf, M.; Toronov, V.; Wolf, U.; Polzonetti, C.; Hueber, D.; Safonova, L.P.; Gupta, R.; Michalos, A.; Mantulin, W.; Gratton, E. *J. Biomed. Opt.*, **2004**, *9*, 221.

[15] Zimmer, J.P.; Kim, S.-W.; Ohnishi, S.; Tanaka, E.; Frangioni, J.V.; Bawendi, M.G. *J. Am. Chem. Soc.*, **2006**, *128*, 2526.

[16] Richards-Kortum, R.; Sevick-Muraca, E. *Annu. Rev. Phys. Chem.*, **1996**, *47*, 555.

[17] Mycek, M.-A.; Pogue, B.W. Marcel Dekker, Inc. New York. Basel: **2003.**

[18] Drezek, R.; Sokolov, K.; Utzinger, U.; Boiko, I.; Malpica, A.; Follen, M.; Richards-Kortum, R. *J. Biomed. Opt.*, **2001**, *6*, 385.

[19] Georgakoudi, I.; Jacobson, B.C.; Mueller, M.G.; Sheets, E.E.; Badizadegan, K.; Carr-Locke, D.L.; Crum, C.P.; Boone, C.W.; Dasari, R.R.; Van Dam, J.; Feld, M.S. *Cancer Res.*, **2002**, *62*, 682.

[20] Sun, J.; Zhu, M.-Q.; Fu, K.; Lewinski, N.; Drezek, R.A. *Int. J Nanomedicine*, **2007**, 2, 235.

[21] Pogue, B.W.; Patterson, M.S. *J. Biomed. Opt.*, **2006**, *11*, 041102.

[22] Torricelli, A.; Pifferi, A.; Taroni, P.; Giambattistelli, E.; Cubeddu, R. *Phys. Med. Biol.*, **2001**, *46*, 2227.

[23] Joshi, A.; Bangerth, W.; Sevick-Muraca, E.M. *Opt. Express*, **2006**.

[24] Jacques, S. *Oregon Medical Laser Center, Portland, OR. Available at: http://omlc.ogi.edu/spectra/intralipid,* **1998**.

[25] Hebden, J.C.; Veenstra, H.; Dehghani, H.; Hillman, E.M.C.; Schweiger, M.; Arridge, S.R.; Delpy, D.T. *Appl. Opt.*, **2001**, *40*, 3278.

[26] *User manual for Maestro 2.2 (CRi)*, **2006**.

[27] Xu, H.; Patterson, M.S. *Opt. Express*, **2006**, *14*, 6485.

[28] Godavarty, A.; Eppstein, M.J.; Zhang, C.; Theru, A.; Thompson, A.B.; Gurfinkel, M.; Sevick-Muraca, E.M. *Phys. Med. Biol.*, **2003**, *48*, 1701.

[29] van Staveren, H.J.; Moes, C.J.M.; van Marle, J.; Prahl, S.A.; van Gemert, M.J.C. *Appl. Opt.*, **1991**, *30*, 4507.

[30] Palmer, K.F.; Williams, D. *J. Opt. Soc. Am.*, **1974**, *64*, 1107.

[31] Adams, K.E.; Ke, S.; Kwon, S.; Liang, F.; Fan, Z.; Lu, Y.; Hirschi, K.; Mawad, M.E.; Barry, M.A.; Sevick-Muraca, E.M. *J. Biomed. Opt.*, **2007**, *12*, 024017.

[32] Qu, J.; MacAulay, C.; Lam, S.; Palcic, B. *Appl. Opt.*, **1994**, *33*, 7397.

[33] Wang, L.-H.; Jacques, S.L.; Zheng, L.-Q. *Comput. Meth. Prog. Bio.*, **1995**, *47*, 131.

[34] Kappas, A.M.; Roukos, D.H. *Ann. Surg. Oncol.*, **2002**, *9*, 828.

[35] Haka, A.S.; Volynskaya, Z.; Gardecki, J.A.; Nazemi, J.; Lyons, J.; Hicks, D.; Fitzmaurice, M.; Dasari, R.; Crowe, J.P.; Feld, M.S. *Cancer Res.*, **2006**, *66*, 3317.

[36] Haglund, M.M.; Hochman, D.W.; Spence, A.M.; Berger, M.S. *Neurosurgery*, **1994**, *35*, 930.

[37] McDougal, W.S. *Nat. Clin. Pract. Oncol.*, **2006**, *3*, 132.

Figure 1 Experimental tissue phantom setup (I)

Figure 2 Experimental tissue phantom setup (II)
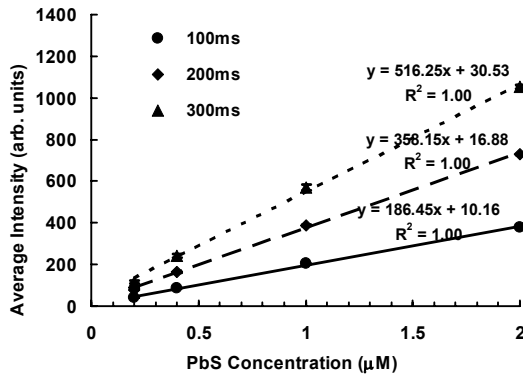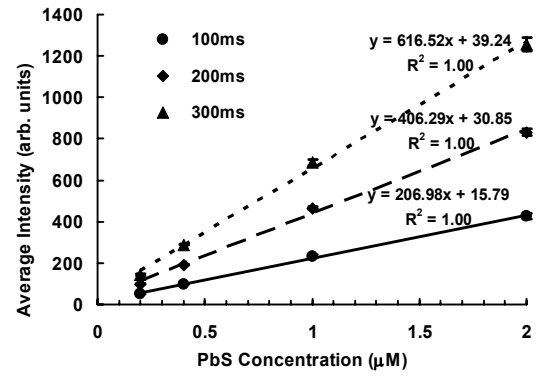
Figure 3 Average image intensities of PbS NIR QDs acquired with no phantom and a 700 nm longpass emission (Em) filter (a) Ex (excitation): 615–665 nm (b) Ex: 575–605 nm. (n=3)

Figure 4 Reduced scattering coefficient of 1% Liposyn tissue phantom
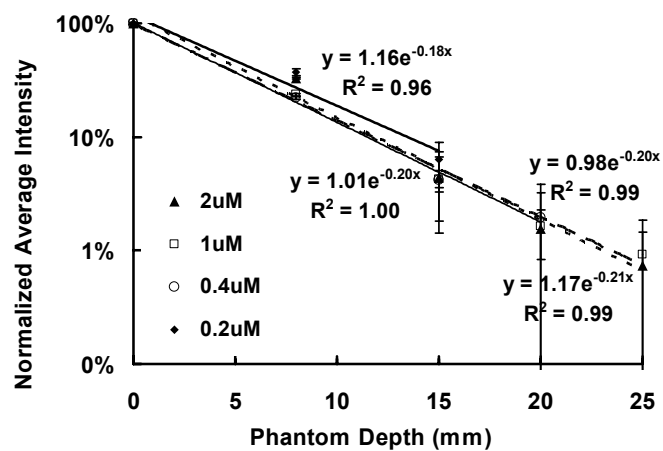
Figure 5 Normalized average intensities of different concentrations of PbS NIR QDs versus phantom thickness (obtained with a bandpass excitation filter of 671 to 705 nm coupled with a 750 nm longpass emission filter, acquisition time: 900 ms) (n=3)
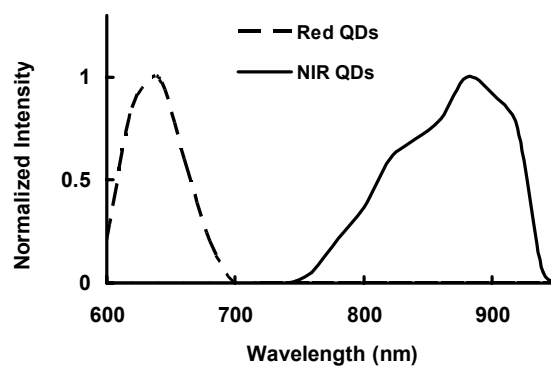
Figure 6 Normalized fluorescence spectra of CdSe/CdS (red) and PbS (NIR) quantum dots (obtained with Maestro Imaging System)
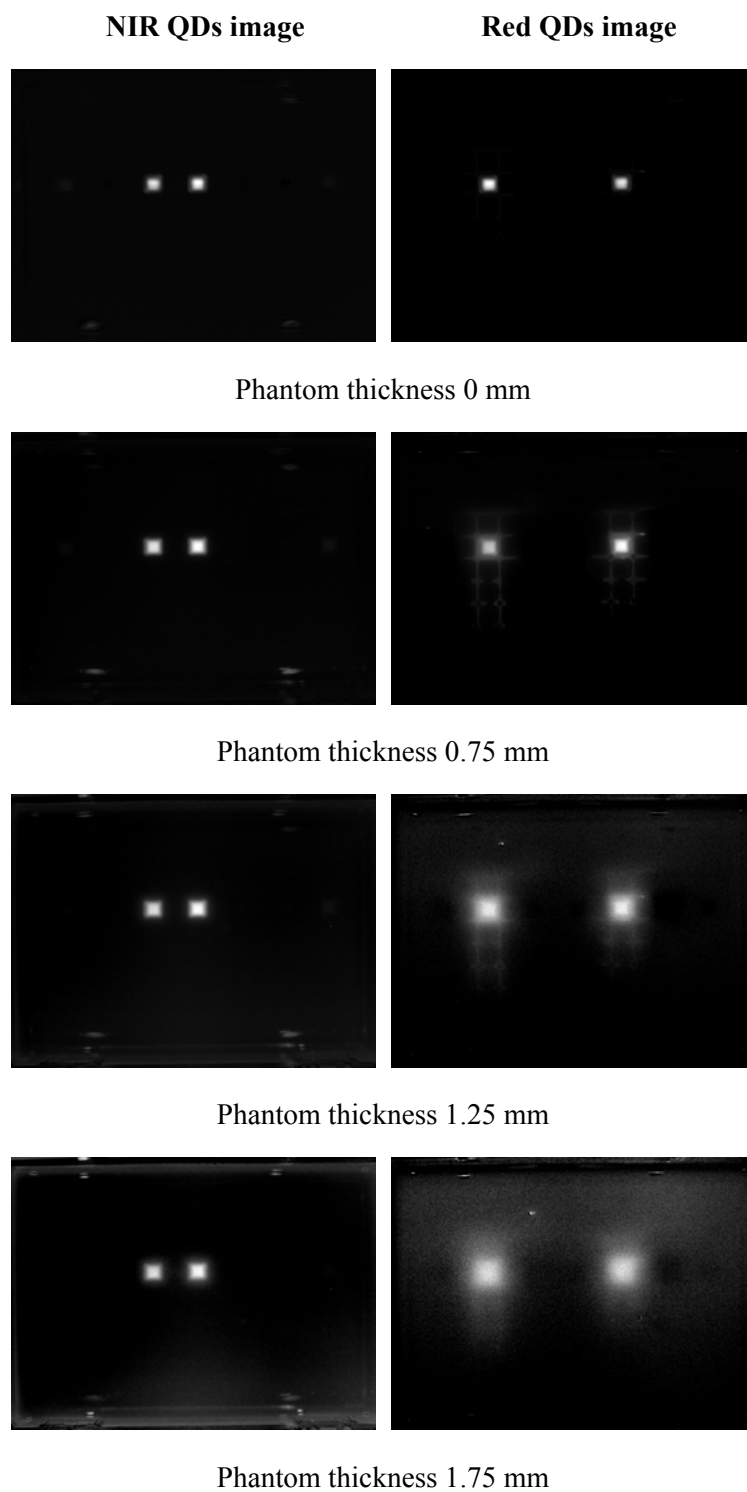
Figure 7 Phantom thickness-resolved florescence images of NIR QDs (spectral unmixed, left column) and red QDs (spectral unmixed, right column)
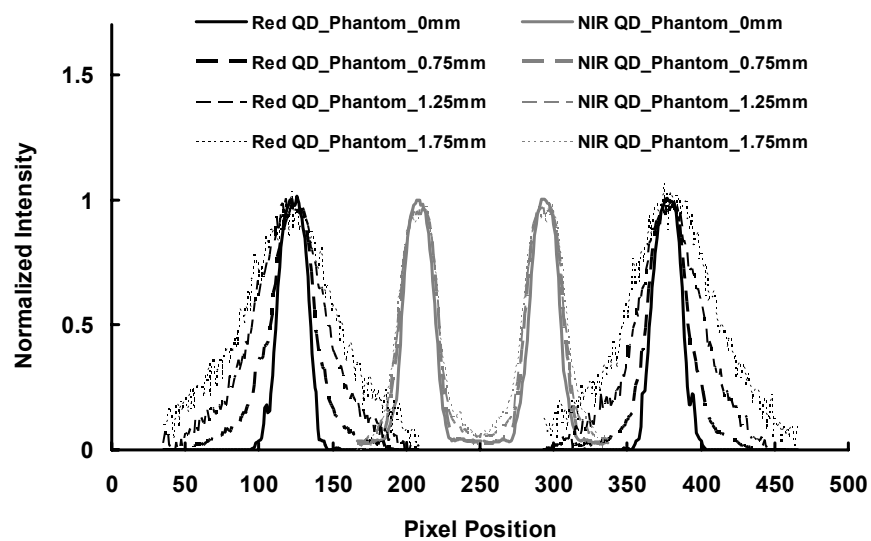
Figure 8 Normalized fluorescence intensity of red and NIR QDs at various phantom depths versus pixel position along section line

Table 1 Filter sets used in study

Detector

Phantom

Sample

Figure 1. Experimental tissue phantom setup (I)

Detector

Phantom

Sample

Figure 2. Experimental tissue phantom setup (II)

Figure 3. Average image intensities of PbS NIR QDs acquired with no phantom and a 700 nm longpass emission (Em) filter (a) Ex (excitation): 615−665 nm (b) Ex: 575−605 nm. (n=3)

Figure 4. Reduced scattering coefficient of 1% Liposyn tissue phantom

Figure 5. Normalized average intensities of different concentrations of PbS NIR QDs versus phantom thickness (obtained with a bandpass excitation filter of 671 to 705 nm coupled with a 750 nm longpass emission filter, acquisition time: 900 ms) (n=3)

Figure 6. Normalized fluorescence spectra of CdSe/CdS (red) and PbS (NIR) quantum dots (obtained with Maestro Imaging System)

NIR QDs image   **Red QDs image**

Phantom thickness 0 mm

Phantom thickness 0.75 mm

Phantom thickness 1.25 mm

Phantom thickness 1.75 mm

Figure 7. Phantom thickness-resolved florescence images of NIR QDs (spectral unmixed, left column), and red QDs (spectral unmixed, right column)

Figure 8. Normalized fluorescence intensity of red and NIR QDs at various phantom depths versus pixel position along section line

Table 1 Filter sets used in study

	Set 1	Set 2	Set 3
Excitation Filter	575−605 nm	671−705 nm	503−555 nm
	615−665 nm		
Emission Filter	700 nm longpass	750 nm longpass	600 nm longpass

Evaluation of Immunotargeted Gold Nanoshells as Rapid Diagnostic Imaging Agents for HER2-Overexpressing Breast Cancer Cells: A Time-based Analysis

**Lissett R. Bickford · Joseph Chang · Kun Fu ·
Jiantang Sun · Ying Hu · André Gobin · Tse-Kuan Yu ·
Rebekah A. Drezek**

Abstract Biomedical nanotechnology offers superior potential for diagnostic imaging of malignancy at the microscopic level. In addition to current research focused on dual-imaging and therapeutic applications in vivo, these novel particles may also prove useful for obtaining immediate diagnostic results in vitro at the patient bedside. However, translating the use of nanoparticles for cancer detection to point-of-care applications requires that conditions be optimized such that minimal time is needed for diagnostic results to become available. Thus far, no reports have been published on minimizing the time needed to achieve acceptable optical contrast of cancer cells incubated with nanoparticles. In this study, we demonstrate the use of gold nanoshells targeted to anti-HER2 antibodies that produce sufficient optical contrast with HER2-overexpressing SK-BR-3 breast cancer cells in only 5 min. This work validates the proof of concept that nanoshells targeted to extracellular biomarkers can be used to enhance cancer diagnostic imaging for use in point-of-care applications.

Keywords nanoshells · point-of-care diagnostics · optical imaging · cancer diagnosis

T.-K. Yu and R.A. Drezek contributed equally to this work.

L. R. Bickford · J. Chang · K. Fu · J. Sun · Y. Hu ·
R. A. Drezek (✉)
Department of Bioengineering, Rice University,
6100 Main St., MS-142,
Houston, TX 77005, USA
e-mail: drezek@rice.edu

K. Fu · T.-K. Yu
Department of Radiation Oncology,
The University of Texas M.D. Anderson Cancer Center,
Houston, TX 77030, USA

A. Gobin
Department of Bioengineering, University of Louisville,
Louisville, KY 40292, USA

R. A. Drezek
Department of Electrical and Computer Engineering,
Rice University,
Houston, TX 77005, USA

Introduction

Several nanoparticles have been explored for potential applications in cancer diagnosis, including nanoshells [1–4], gold colloid [5, 6], quantum dots [7, 8], carbon dots [9], nanorods [10–12], and nanocrystals [13]. For in vivo applications, several steps will need to be taken to ensure the safe delivery of nanoparticles before they can be used in a clinical setting. However, several opportunities still exist for in vitro applications in which the cytotoxicity of nanoparticles is immaterial. Numerous in vitro technologies that have shown promise for point-of-care diagnostic testing may allow clinicians to provide user-friendly, cost-effective, and rapid results at the patient bedside. Currently, these technologies involve analyzing biological fluids to detect DNA or protein amplification through the use of microarrays or biochip devices [14–16]. In addition to fluid-based modalities, these microscopic advancements can also be used to analyze larger biological components, such as excised tumor specimens, for cancer screening and diagnosis. One particular area of application is the diagnosis of cancer from biopsy samples. For example, after a breast biopsy, the specimen is sent to a pathology laboratory where it is processed and examined microscopically for morphological abnormalities and sometimes analyzed for the presence of molecular biomarkers of

disease, such as hormone receptor expression [17]. This process can take up to several days, during which the patient must cope with the fear of an unknown diagnosis and the potential of treatment delay. Mojica et al. [18] showed that delays between initial breast cancer symptoms and treatment are associated with lower survival rates. Consequently, delays in breast cancer diagnosis top the list of liability claims made against physicians [19].

Another area of opportunity for advancement in point-of-care microscopic analysis of tumor specimens involves the assessment of intraoperative tumor margins. During a lumpectomy, for instance, the surgeon removes the suspected cancerous lesion with a margin of normal tissue. Judgment of the width of this margin is largely based on tactile sensation and visible, macroscopic abnormalities. In advanced hospital systems, the sample is excised and immediately subjected to pathologic analysis to ensure the surgical margins are tumor-free before the procedure is completed. The need to achieve negative margins is critical in minimizing cancer recurrence and progression, particularly for patients undergoing breast conservation therapy [20]. The presence of a positive surgical margin has been associated with lower rates in patient survival [18]. Due to residual cancer cells being left in many patients that undergo breast conservation therapy, as many as 40% of patients have experienced local breast cancer recurrence near the site of the original tumor [21]. Positive margins in a surgical specimen, therefore, necessitate the resection of additional tissue until the margins do not contain tumor. Even if the specimens are examined immediately, this extends the period of anesthesia and hence increases both the cost and risk to the patient. Furthermore, many county hospitals must, by necessity, process tissue samples after the surgery is completed. In that case, the identification of positive surgical margins requires that the patient undergo another surgical procedure to excise the remaining tissue, which further delays the start of adjuvant treatment and increases the risk of cancer recurrence and subsequent patient mortality.

With the expansion of nanotechnology-driven research, opportunities for the use of fast and accurate diagnostic tests outside of the hospital laboratory are likely to increase. To realistically use nanoparticles as a point-of-care tool for the immediate assessment of key cancer gene signatures in excised tissue samples, the time needed to achieve optical contrast must be minimized. Thus far, few published reports have focused on minimizing the time needed to achieve suitable contrast of cancer cells incubated with nanoparticles. Previous studies demonstrating the effectiveness of using gold-based nanoparticles targeted to extracellular cancer biomarkers have involved incubation times ranging from 30 to 90 min [1, 3, 5, 6, 10–12]. The objective of this study was to demonstrate the feasibility of using gold nanoshells targeted to anti-HER2 antibodies to achieve sufficient optical contrast in a HER2-overexpressing breast cancer cell line (SK-BR-3) after a series of incubation times. Overexpression of the HER2 receptor is associated with greater cancer progression and is seen in approximately 15–25% of all breast cancer cases [17]. The nanoshells, made of dielectric silica particles covered with a thin gold shell, were fabricated to scatter strongly in the near-infrared spectrum through manipulation of the silica core/gold shell ratio. We compared the contrast that could be achieved by incubating the nanoshells with both normal and cancerous cells. Our results demonstrate that gold nanoshells targeted to this cell-surface marker can produce enhanced contrast after only 5 min of incubation. This proof of concept supports the initial feasibility of using gold nanoshells for potential point-of-care diagnostic applications.

Materials and Methods

Nanoshell Fabrication

Nanoshells were developed and bioconjugated by using previously reported procedures [22]. First, silica cores were prepared with the Stöber method [23], in which tetraethyl orthosilicate (Sigma Aldrich) is reduced in ammonium hydroxide and pure ethanol. Next, aminopropyltriethoxysilane was used to functionalize the particles by terminating the silica core surface with amine groups. The silica particles were then measured by scanning electron microscopy (SEM) to obtain the average silica core diameter of 254 nm.

To create the gold shell overlap for the silica cores, gold colloid of 1–3 nm in diameter was fabricated based on procedures documented by Duff et al. [24]. The gold colloid solution was stored at 4 °C for 2 weeks and subsequently concentrated with a Rotovap. After aging and concentration, the gold colloid solution was added to the aforementioned functionalized silica particles, forming 'seeds' in which the gold colloid is adsorbed to the amine groups of the silica cores. To complete nanoshell fabrication, a cocktail of hydrogen tetrachloroaurate trihydrate ($HAuCl_4$) and potassium carbonate was added to the seeds along with formaldehyde to catalyze the formation of the shells. The spectrum of the completed nanoshells was analyzed with a UV-vis spectrophotometer (Varian Cary 300). The relationship between the extinction spectrum obtained by UV-vis spectroscopy and that obtained by application of the Mie scattering theory can be used to approximate the size of the nanoparticles in solution (Fig. 1). Subsequently, Mie Theory can be used to derive the absorption, scattering, and extinction coefficients for nanoparticles of a specific size, and a standard known
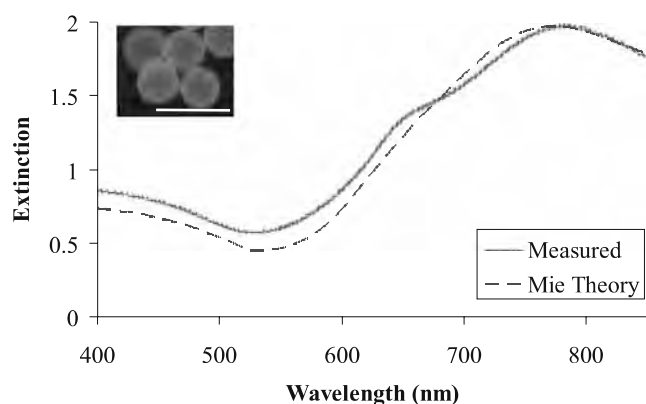
Fig. 1 Measured spectra of nanoshells (core radius, 127 nm; shell thickness, 19 nm) as compared with that estimated using the Mie scattering theory; the *insert* depicts the corresponding image from scanning electron microscopy. *Scale bar* represents 500 nm.

concentration can be acquired for a particular optical density. In addition to using Mie scattering theory for multilayer spheres, we also used SEM to confirm the size of the nanoshells. The nanoshells used in this study had an average diameter of 292 nm, a peak surface plasmon resonance at 778 nm and a concentration of approximately 1.6×10^9 particles/ml.

Nanoshell Surface Modification

To target the prepared nanoparticles to molecular markers associated with HER2-overexpression, antibodies were first prepared by methods previously described by Hirsch et al. [22]. Briefly, anti-HER2 antibodies (C-erbB-2/HER-2/*neu* Ab-4, Lab Vision Corporation) were conjugated to the heterobifunctionalized polyethylene glycol linker orthopyr-idyl-disulfide-PEG-*N*-hydroxysuccinimide ester (OPSS-PEG-NHS, MW=2 kD, CreativeBiochem Laboratories) by reaction at a molar ratio of 1:3 in sodium bicarbonate (100 mM, pH 8.5) overnight on ice. Aliquots were stored at −80 °C. The amidohydroxysuccinimide group (NHS) enables conjugation of the PEG linker to the antibodies through amide linkages; the remaining end of the PEG linker, OPSS, allows binding to the nanoshell gold surfaces through sulfur groups. The nanoshells (1.6×10^9 particles/ml) were incubated with the prepared anti-HER2-PEG solution (0.4 mg/ml) for 1 h at 4 °C. The newly conjugated nanoshells were subsequently incubated with a 10 μM polyethylene glycol-thiol solution (PEG-SH, MW=5 kD, Nektar) for 2 additional hours at 4 °C, which stabilized the nanoshells by blocking any unoccupied adsorption sites. The nanoshells were then centrifuged to remove unbound antibodies, resuspended in ultrapure water, and stored at room temperature until use. Before being incubated with cells, the nanoshell solution was supplemented with bovine serum albumin and phosphate-buffered saline (PBS) at final concentrations of 1% each.

Preparation of Cells

Two cell types were analyzed for this study: the HER2-overexpressing epithelial breast cancer cell line SK-BR-3 and the normal mammary epithelial cell line MCF10A (American Type Culture Collection). The SK-BR-3 cells were grown in McCoy's 5A medium supplemented with 10% fetal bovine serum and 1% penicillin-streptomycin and maintained at 37 °C in a 5% CO_2 atmosphere. The MCF10A cells were cultured in Mammary Epithelial Basal Medium (MEBM) supplemented with a BulletKit (Clonetics) and also maintained at 37 °C in 5% CO_2. Both cell lines were grown in 25-cm^2 culture flasks until confluent. At that time, cells were rinsed once with 1× PBS and incubated with trypsin-ethylenediaminetetraacetic acid for 5 min at 37 °C to detach the cells from the substrate, after which trypsin was neutralized with the appropriate medium and the cells were counted. Approximately 6×10^5 cells were placed in each of four conical tubes per cell line for each time point under investigation. The cells were then centrifuged at 115×g for 3 min. For each cell line and each time point of interest, three cell pellets were resuspended in the bioconjugated nanoshell solution, and one was resuspended in an equal amount of PBS as a control. The nanoshell–cell suspensions and controls were then incubated in a hybridization chamber (VWR International) at 37 °C and a motor speed of 7 rpm for 5, 10, 30, or 60 min. After incubation, the suspensions were centrifuged at 115×g for 3 min, and the unbound nanoshells were collected with a pipette. Cells were then rinsed once with 1× PBS, centrifuged, and the unbound nanoshells were again collected. A small volume (5 μl) of 10% glucose mixed with PBS was added to the remaining cell pellets to prevent cell death during imaging. Approximately 7 μl of each pellet was placed on a glass slide and coverslipped for immediate microscopic analysis.

Darkfield Imaging and Processing

Images of the two cell types incubated with nanoshells were obtained with a Zeiss Axioskop 2 darkfield microscope outfitted with a color camera (Zeiss AxioCam MRc5). Darkfield microscopy depends on light scattering to achieve contrast. All images were taken under the same lighting conditions and magnification (×20). Optical intensity was quantified by using a Matlab code. Based on this code, an image with a value of 0 was designated pure black and that with a value of 255 pure white. An increase in intensity, therefore, corresponded to an image with a higher numerical value. Average intensity values for each time point and each cell line were calculated from ten independent cell samples that were devoid of scattering influences from neighboring cells and unbound nanoshells. Sample normality was assessed by using Minitab to evaluate the error

Fig. 2 Darkfield images
of MCF10A and SK-BR-3 cells
incubated with bioconjugated
nanoshells for the indicated
times. Images were obtained
at ×20. *Scale bar* represents
125 μm.

MCF10A   SK-BR-3

0 min.

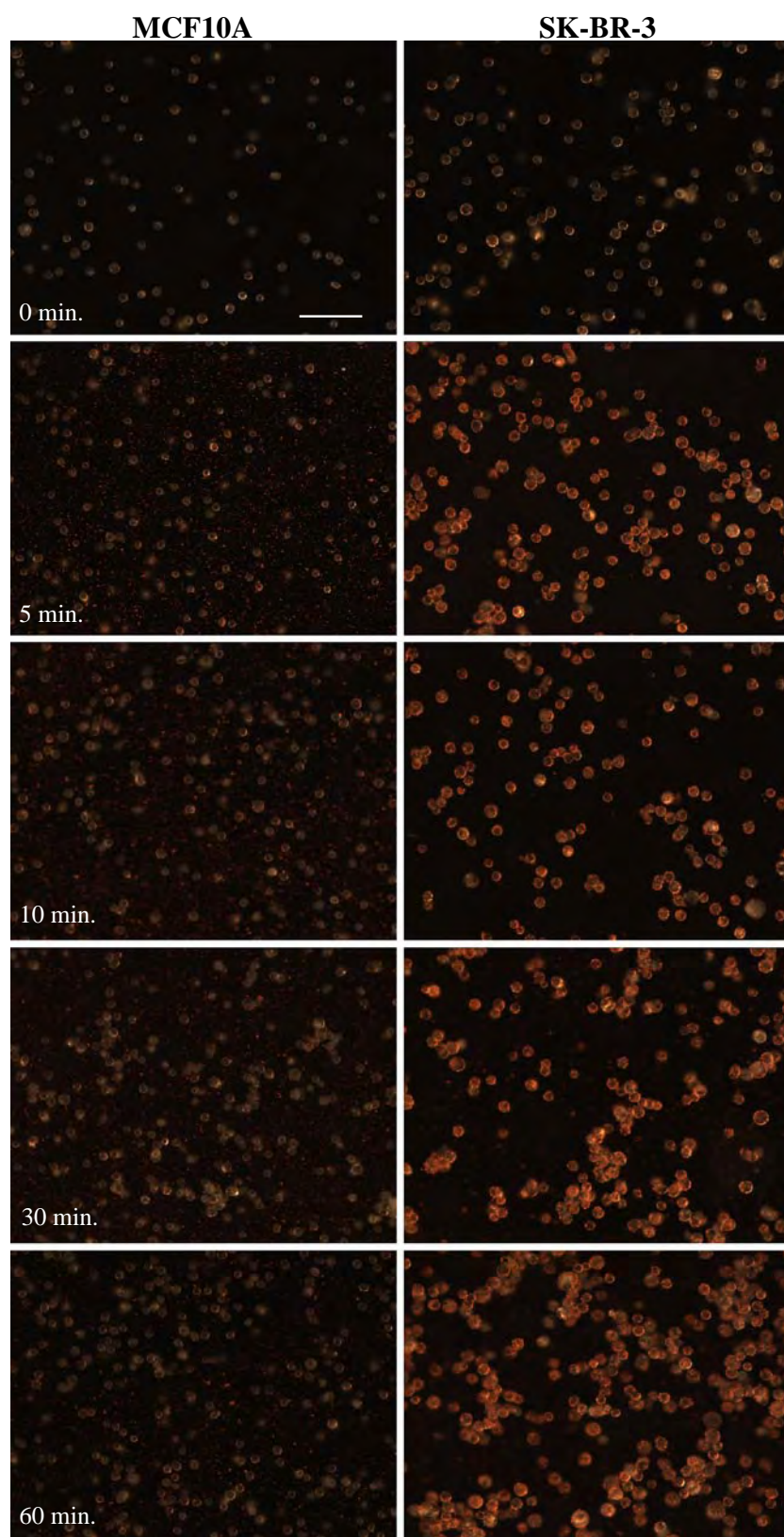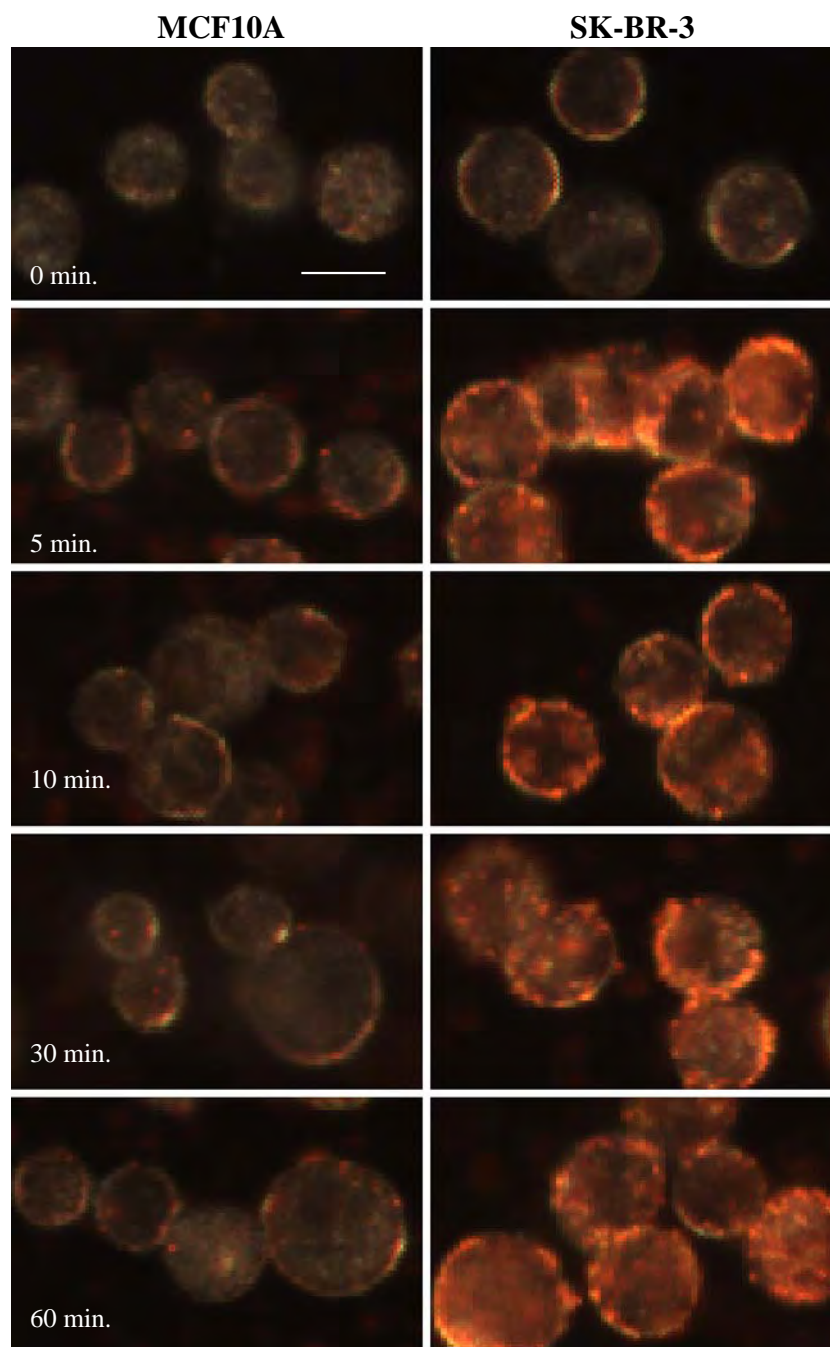5 min.

10 min.

30 min.

60 min.

Fig. 3 Enlarged darkfield images of MCF10A and SK-BR-3 cells incubated with the bioconjugated nanoshells for the indicated times. Original images taken at ×20. *Scale bar* represents 20 μm.

distribution for all data points. A normal probability plot of the residuals verified that the samples followed a normal distribution (data not shown). F tests were also used to determine the equality of variance before applying two-tailed paired Student's t tests to evaluate significance.

Derivation of Bound Nanoshell Concentration using Spectroscopy

According to the Beer–Lambert law, the absorbance of particles in solution is directly related to the concentration of those particles in that solution. To validate the ability of spectroscopy to predict the concentration of a solution of nanoshells of known size, we used linear regression analysis. Nanoshells of known concentration, based on the Mie Theory calculations, were serially diluted and, the corresponding peak absorbance values were measured. We considered a concentration of approximately 2.0×10^9 particles/ml (optical density=2.4) as a 100× concentration. From this analysis, an equation relating the peak absorbance (independent variable) to each known nanoshell concentration (dependent variable) was used to approxi-
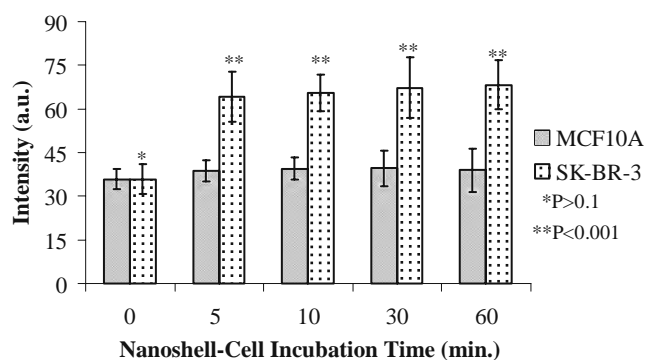
Fig. 4 Mean quantitative intensity values for samples of MCF10A and SKBR3 cells incubated with nanoshells for the indicated times. Differences between cell types incubated without nanoshells were not statistically significant ($P>0.1$, $n=10$). Differences between cell types incubated with nanoshells were statistically significant at all time points ($P<0.001$, $n=10$). *Error bars* indicate standard deviations.

mate the number of nanoparticles in subsequent solutions of unknown concentration. This derivation was necessary to calculate the approximate number of bound nanoparticles per cell at the different time points.

To determine and compare the number of nanoshells bound after 5 min and 60 min of incubation, the collected unbound nanoshells were centrifuged at $255\times g$ for 20 min, resuspended in ultrapure water, transferred to cuvettes and sonicated briefly before being measured with a UV-vis spectrophotometer. The spectrum was recorded and the
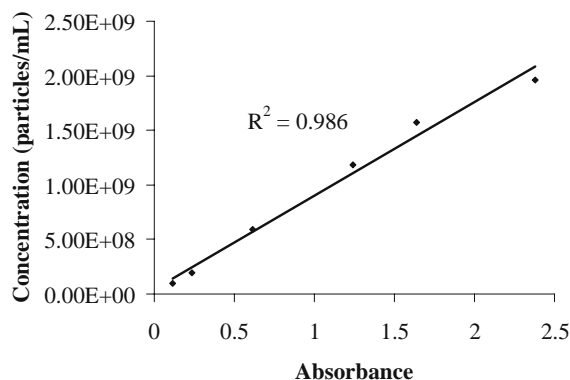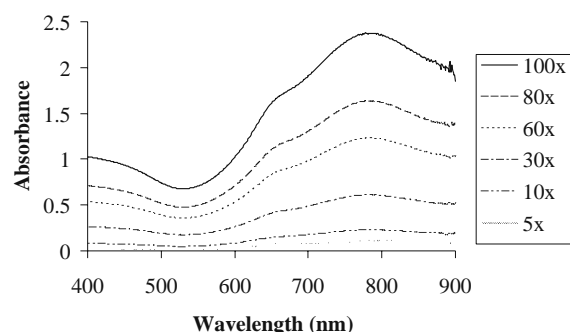
Fig. 5 *Top* Spectra of serial dilutions of known nanoshells concentrations in suspension. *Bottom* Linear regression analysis of known nanoshell concentrations vs. the corresponding peak absorbance values.

peak absorbance documented for each sample. Based on the original concentration of nanoshells, the number of cells used, and the concentration of the collected unbound nanoshells, the approximate number of nanoshells bound to each cancer cell was derived. An F test was also used to determine the equality of variance before applying a two-tailed paired Student's t test to evaluate significance.

Results/Discussion

We evaluated the contrast that could be achieved by incubating nanoshells targeted to HER2 receptors with normal breast epithelial cells (MCF10A) or breast cancer cells (SK-BR-3) for four intervals: 5, 10, 30, and 60 min. All procedures were done with triplicate samples and included a control condition (cells to which no nanoshells had been added). Figures 2 and 3 illustrate original and enlarged images obtained at all four time points for both cells lines and for cells incubated without nanoshells (designated as 0 min). Because the optical peak resonance for the fabricated nanoparticles occurred at 778 nm, the nanoshells scattered strongly in the near-infrared range and could be visualized under darkfield illumination as red particles. Qualitative assessment of the imaging results revealed that the MCF10A cells showed little enhanced scattering at any period of incubation with the bioconjugate–nanoshell solution compared with both controls or the cancer cells. However, the SK-BR-3 cancer cells showed enhanced contrast after as little as 5 min of incubation. Typically, SK-BR-3 cells express about 8×10^5 receptors per cell and normal MCF10A cells about 1×10^4 [25, 26]. The targeted bioconjugated nanoshells apparently bound to cell surface receptors on both cell types; however, because the cancer cells had higher numbers of receptors, the contrast that could be achieved was considerably greater with those HER2-overexpressing cells. Other evidence of the superior contrast achieved with the SK-BR-3 cells was apparent from the difference in the numbers of unbound nanoshells between the two cell types. In the images of the
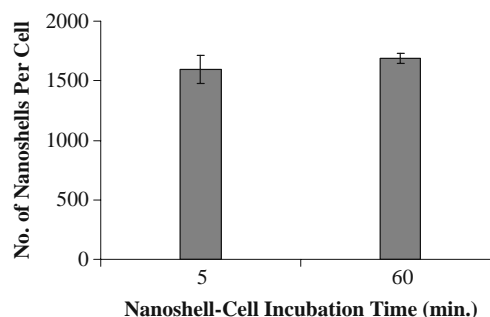

Fig. 6 Number of nanoshells bound per SK-BR-3 cell after 5 and 60 min of incubation. Values shown are the means of triplicate measurements. *Error bars* indicate standard deviations.

MCF10A cells, several unbound nanoshells could be seen between cells despite our attempts at removing unbound nanoshells by rinsing the cells. Considerably fewer such nanoshells were present in the SK-BR-3-nanoshell images (Fig. 2).

To quantitatively assess the increase in contrast between the normal and cancerous cells at each time point, we used a Matlab code to evaluate the average intensity of ten cells from each condition; an intensity value of 0 was considered pure black and 255 pure white. Statistical analyses indicated no difference between either cell type incubated with only PBS (the control condition; $P>0.1$). However, differences between the MCF10A cells and the SK-BR-3 cells were significant at all four incubation times ($P<0.001$; Fig. 4). An additional analysis of variance showed no differences in the mean intensity of the SK-BR-3 cells at any of the four incubation times ($P>0.5$).

To further compare the differences between contrast that could be achieved at 5 and 60 min for the SK-BR-3 cells, we examined the number of bound nanoshells at both time points. To do so, we first developed a simple UV-vis spectroscopy method to determine the concentration of nanoshells in solution. On the basis of dilutions of known nanoshell concentrations, we used linear regression to estimate the concentration of nanoshells in a given solution (Fig. 5). We confirmed the existence of a linear relationship between absorbance and corresponding concentration of nanoshells for concentrations ranging from 9.8×10^{7} to 2.0×10^{9} particles/ml. With a goodness-of-fit (R^2) value of 0.986, we concluded that the absorbance accurately predicts the concentration of an unknown suspension of nanoparticles that falls within this range.

We next used this relationship between absorbance and concentration to measure the absorbance of unbound nanoshells collected after incubation and cell rinsing and subsequently resuspended in a volume of water equal to that of the diluted samples of known concentration. Knowing the initial number of nanoshells and cells, we could derive the approximate number of nanoshells bound to each cell, which we did for the triplicate samples of nanoshells plus cells after 5 and 60 min of incubation. At 5 min of incubation, $1{,}593\pm121$ nanoshells were bound per cell; at 60 min, the range was $1{,}686\pm40$ nanoshells per cell ($P>0.1$, not significant; Fig. 6). Thus, roughly 95% of the binding noted at 60 min had occurred within the first 5 min of incubation. Our imaging results suggest that this 5% difference did not seem to affect contrast.

Conclusions

Our findings support the proof of concept that optical contrast of HER2-overexpressing breast cancer cells can be achieved by brief periods of incubating those cells with nanoshells. Although the ability to detect malignancy by such means is critical for in vivo applications and for in vitro applications associated with biological fluids, other opportunities exist for using such techniques to diagnose solid tumor specimens in vitro. The time between diagnosis and treatment could be drastically shortened by the use of microscopic evaluations of excised tissue samples that provide rapid and reliable results. We have shown both qualitatively and quantitatively that nanoshells can be used to achieve discernible contrast between cancerous and normal breast cells in 5 min. These results suggest that gold nanoshells can be designed and optimized to enhance the scattering signatures of cancer cells at minimal incubation times necessary for potential applications in point-of-care cancer diagnostic imaging. Future studies are underway to extend these findings from the cellular level to tumor specimen models.

References

1. Loo C, Lowery A, Halas N, West J, Drezek R. Nano Lett 2005;5(4):709–11.
2. Loo C, Hirsch L, Lee M-H, Chang E, West J, Halas N, Drezek R. Optics Lett 2005;30:1012–4.
3. Lowery A, Gobin A, et al. Int J Nanomed 2006;1:149–54.
4. Gobin AM, Lee MH, Halas NJ, James WD, Drezek RA, West JL. Nano Lett 2007;7:1929–34.
5. Sokolov K, Follen M, Aaron J, Pavlova I, Malpica A, Lotan R, et al. Cancer Res 2003;63:1999–2004.
6. El-Sayed IH, Huang X, El-Sayed MA. Nano Lett 2005;5(5):829–34.
7. Sun J, Zhu MQ, Fu K, Lewinski N, Drezek R. Int J Nanomed 2007;2(2):235–40.
8. Gao X, Cui Y, Levenson RM, Chung LW, Nie S. Nat Biotechnol 2004;22(8):969–76.
9. Cao L, et al. J Am Chem Soc 2007;129:11318–9.
10. Huang X, El-Sayed IH, Qian W, El-Sayed MA. J Am Chem Soc 2006;128:2115–20.
11. Durr NJ, Larson T, Smith DK, Korgel BA, Sokolov K, Ben-Yakar A. Nano Lett 2007;7:941–5.
12. Yu C, Nakshatri H, Irudayaraj J. Nano Lett 2007;7(8):2300–6.
13. Sukhanova A, Devy J, Venteo L, Kaplan H, et al. Anal Biochem 2004;324:60–7.
14. Zajac A, Song D, Qian W, Zhukov T. Colloids Surf B Biointerfaces 2007;58:309–14.
15. Weigum SE, Floriano PN, Christodoulides N, McDevitt JT. Lab Chip 2007;7(8):995–1003.

16. Culha M, Stokes DL, Griffin GD, Vo-Dinh T. JBO 2004;9 (3):439–43.
17. National Comprehensive Cancer Network. Breast cancer treatment guidelines for patients. Version IX. 2007.
18. Mojica CM, Bastani R, Boscardin WJ, Ponce NA. Cancer Control 2007;14(2):176–82.
19. Guthrie TH. Breast J 1995;1(6):376–9.
20. Klimberg VS, Harms S, Korourian S. Surg Oncol 1999;8:77–84.
21. Fisher B, Anderson S, Bryant J, Margolese RG, Deutsch M, Fisher ER, Jeong JH, Wolmark N. NEJM 2002;347:1233–41.
22. Hirsch LR, Halas NJ, West JL. Methods Mol Biol 2005;303:101–11.
23. Stöber W, Fink A, et al. J Colloid Interface Sci 1968;26:62–9.
24. Duff DG, Baiker A, Edwards PP. Langmuir 1993;9:2301–9.
25. Hayes DF, Walker TM, et al. Int J Oncol 2002;21(5):1111–7.
26. Kornilova ES, Taverna D, et al. Oncogene 1992;7(3):511–9.

Enhanced multi-spectral imaging of live breast cancer cells using immunotargeted gold nanoshells and two-photon excitation microscopy

Lissett Bickford[1,3]**, Jiantang Sun**[1,3]**, Kun Fu**[1,2]**,
Nastassja Lewinski**[1]**, Vengadesan Nammalvar**[1]**,
Joseph Chang**[1] **and Rebekah Drezek**[1,2,4]

[1] Department of Bioengineering, Rice University, Houston, TX 77005, USA
[2] Department of Electrical and Computer Engineering, Rice University, Houston,
TX 77005, USA

E-mail: drezek@rice.edu

Abstract
We demonstrate the capability of using immunotargeted gold nanoshells as contrast agents for
in vitro two-photon microscopy. The two-photon luminescence properties of different-sized
gold nanoshells are first validated using near-infrared excitation at 780 nm. The utility of
two-photon microscopy as a tool for imaging live HER2-overexpressing breast cancer cells
labeled with anti-HER2-conjugated nanoshells is then explored and imaging results are
compared to normal breast cells. Five different imaging channels are simultaneously examined
within the emission wavelength range of 451–644 nm. Our results indicate that under
near-infrared excitation, superior contrast of SK-BR-3 cancer cells labeled with
immunotargeted nanoshells occurs at an emission wavelength ranging from 590 to 644 nm.
Luminescence from labeled normal breast cells and autofluorescence from unlabeled cancer and
normal cells remain imperceptible under the same conditions.

(Some figures in this article are in colour only in the electronic version)

1. Introduction

Accurate cancer diagnosis through its multi-stage progression is critical for developing effective and selective cancer treatments. In order to provide clinicians with functional diagnostic results, knowledge of the molecular signatures of carcinogenesis is necessary. Due to their overexpression during the development of cancer, several biomarkers have been identified as a biological means of characterizing these signatures [1]. Although the acquisition of molecular-specific data is typically associated with gene arrays and

proteomics [2], there is an opportunity to use such biomarkers as tools for both *in vitro* and *in vivo* diagnostic evaluations of tissue specimens, such as during surgery, in order to identify malignant cells among heterogeneous tissue.

Silica-based gold nanoshells, which are advantageous for several biological applications due to their unique optical tunability and potential as multi-modal agents, have previously demonstrated enhanced diagnostic imaging potential of carcinogenesis at the microscopic scale through the use of extracellular biomarkers [3–6]. By manipulation of the size of their silica cores and gold outer shells, nanoshells can be optically tuned to absorb or scatter light from wavelengths ranging from the visible to the near-infrared, allowing for both imaging and therapy applications [7]. Achieving optimal contrast of gold nanoshells for biological diagnostics includes

---

[3] These authors contributed equally to this work, listed alphabetically by last name.
[4] Address for correspondence: Department of Bioengineering, Rice University, 6100 Main Street, MS-142, Houston, TX 77005, USA.

a combination of developing nanoshells that are tuned to scatter or absorb light in the near-infrared (NIR), where biological chromophores absorb minimal light, and the use of NIR-based imaging systems.

Although several optical devices have been used to validate applications of gold nanoshells as viable contrast agents [3–15], none have focused on evaluating the effectiveness of using immunotargeted nanoshells as contrast agents for cell surface biomarkers using nonlinear excitation microscopy. Nonlinear optics has been used extensively for analyzing fluorescent signals in animal models and tissue samples [16–20]. By using a femtosecond pulsed laser, two photons can be used simultaneously to excite tissue molecules similar to the excitation generated by a single photon, but with twice the energy. Only the molecules at the focus of the femtosecond laser will be excited, resulting in greater resolution than that achievable with single-photon systems, such as conventional confocal microscopy. Additionally, unlike conventional confocal microscopy, a pinhole is not required to reject out-of-focus light and the inherent excitation at only the focal plane means that biological tissue undergoes less photodamage [20]. Although multi-photon microscopy has frequently been used for enhancing fluorescent signals [16, 20], studies have demonstrated that metal particles display photoluminescence as a result of excitation by such multi-photon systems [21, 22]. This photoluminescence is induced by a significant field enhancement that occurs upon multi-photon excitation of the metallic molecules [21]. Thus far in the literature, metallic nanoparticles analyzed for two-photon imaging potential have included gold colloid spheres [23, 24], gold nanorods [25–29], and gold nanoshells [14]. A recent publication on the use of two-photon microscopy for evaluating nanoshell contrast focused on potential dual imaging and therapy applications where unlabeled nanoshells were delivered to murine tumors through extravasations due to the presence of leaky vasculature [14]. However, since nanoshell dimensions are fundamentally variable [7], it is important to further elucidate and confirm the two-photon properties of these highly tunable nanoparticles despite differences in size. Furthermore, since cancer undergoes a multi-stage progression, the ability to track molecular signatures through the overexpression of biomarkers is crucial in obtaining functional and accurate diagnostic results. Therefore, the goal of our study was to demonstrate the nonlinear properties of very different-sized nanoshells and validate the proof of concept that immunotargeted nanoshells can be used to enhance the contrast of malignant human cells *in vitro* through nonlinear excitation prior to our evaluation of this system in excised tissue specimens. Additionally, through the use of two-photon excitation and multi-spectral imaging, the simultaneous acquisition of images at different emission wavelengths was obtained to ascertain the optimal imaging parameters for this system.

We demonstrate the two-photon luminescence properties of two different sizes of gold nanoshell designed with a similar plasmon resonance in the near-infrared. We evaluate the enhanced contrast by comparing HER2-overexpressing
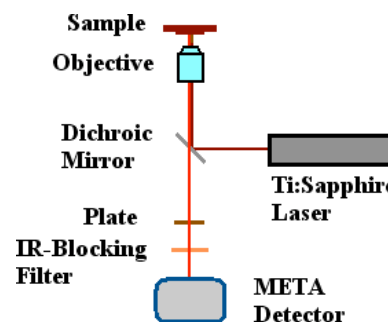

Figure 1. Schematic of Zeiss LSM 510 META multi-photon system configuration.

breast cancer cells to normal breast cells with and without targeted anti-HER2-bioconjugated gold nanoshells at five different emission wavelength ranges: 451–483, 483–515, 515–547, 558–579, and 590–644 nm. By evaluating imaging results under different ranges, we explore the broad emission properties of silica-based gold nanoshells under two-photon induced luminescence. The anti-HER2 antibody was selected as a model for surface tumor targeting due to the association of HER2-overexpression with more aggressive breast cancers seen in 15–25% of all breast cancer cases [30]. Additionally, studies in our laboratory have previously demonstrated the effectiveness of using immunotargeted nanoshells as diagnostic imaging agents for HER2-overexpressing cancer cells [3, 5, 6, 13]. We show that for immunotargeted nanoshells with a silica core diameter of 254 nm and a gold shell thickness of 19 nm imaged with our specific system, the optimal emission wavelength for observing enhanced contrast of HER2-overexpressing breast cancer cells occurs between 590 and 644 nm at 10% of maximum excitation power. Under similar conditions, normal breast cells are not detectable.

2. Method

2.1. Multi-photon imaging system

A Zeiss laser scanning microscope (LSM) 510 META multi-photon system was used in conjunction with a Coherent Chameleon femtosecond mode-locked Ti:sapphire laser to collect two-photon data (figure 1). The wavelength of the polarized output laser beam was tunable between 720 and 950 nm with pulse width of 140 fs at a repetition rate of 90 MHz. A short-pass dichroic mirror (KP700/488, Zeiss) was used to reflect the incident NIR excitation light onto the sample through a 20× or 63× objective and to collect the two-photon-induced luminescence data. To further eliminate the background signal of the excitation light, a wave plate and an IR-blocking filter (BG39, Zeiss) were placed in front of the META detector. The Zeiss LSM META system allowed simultaneous multi-spectral imaging and recording of up to eight emission channels. The maximum output power of the Chameleon femtosecond laser was around 1640 mW for excitation at 780 nm. Based on data from the manufacturer, less than 10% of this power was incident on the sample. The excitation wavelength of 780 nm was chosen as it was within 10 nm of the extinction peak for both nanoshell sizes.

2.2. Nanoshell fabrication

Nanoshells were developed as described in previous publications [3–5]. First, the Stöber method was used to create silica cores by reducing tetraethyl orthosilicate (Sigma Aldrich) in ammonium hydroxide and pure ethanol [31]. Aminopropyltriethoxysilane (APTES) was then added in order to terminate the silica core surfaces with amine groups, which formed functionalized particles. The two different-sized groups of silica particles were measured by scanning electron microscopy (SEM) to obtain the average silica core diameters of 130 and 254 nm. The gold shell overlay on the silica cores was also created using previously described methods [3–5]. First, using procedures outlined by Duff *et al* [32], gold colloid of 1–3 nm in diameter was developed and then aged under refrigeration for two weeks. The colloid was then concentrated using a Rotovap and added to the functionalized silica particles mentioned above. By interacting with the functionalized amine group surfaces of the silica particles, the gold colloid was adsorbed, forming surfaces with partial gold coverage. Addition of more gold completed the formation of the shell through catalysis of formaldehyde with hydrogen tetrachloroaurate trihydrate ($HAuCl_4 3H_2O$) and potassium carbonate. Two groups of nanoshells were fabricated and both were spectrally analyzed using a Varian Cary 300 UV–vis spectrophotometer (figure 2). The final sizes of the nanoshells were determined using SEM imaging (figure 2, inset) and confirmed using Mie theory simulation for multi-layer spheres. The smaller nanoshells had an average gold shell thickness of 21 nm. The larger nanoshells had an average shell thickness of 19 nm. The nanoshells were stored in deionized water at 4 °C until further use.

2.3. Nanoshell surface modification and bioconjugation

For live cell imaging, the larger nanoshells were used and targeted to HER2-overexpressing cells through conjugations with anti-HER2 antibodies. In order to prepare the immunotargeted nanoshells, a heterobifunctionalized polyethylene glycol linker (orthopyridyl-disulfide-PEG-N-hydroxysuccinimide ester, OPSS-PEG-NHS, MW = 2 kD, CreativeBiochem Laboratories) was first conjugated to anti-HER2 antibodies (C-erbB-2/HER-2/neu Ab-4, Lab Vision Corporation) through amide linkages that joined the amidohydroxysuccinimide group (NHS) of the PEG linker to the antibodies. This reaction proceeded at a 3:1 molar ratio in sodium bicarbonate (100 mM, pH 8.5) on ice overnight. Aliquots of the 'PEGylated' antibodies, at a concentration of 0.4 mg ml^{-1}, were stored at −80 °C until use. Conjugation of the nanoshells to the PEGylated antibodies was then carried out through sulfur linkages between the gold nanoshell surfaces and the remaining OPSS group of the heterobifunctional PEG linker. This was performed by incubating the nanoshells, at a concentration of 1.6×10^9 particles ml^{-1}, with the PEGylated antibodies for 1 h under refrigeration (4 °C). In order to block vacant adsorption sites, the nanoshells were further incubated with a 10 μM polyethylene glycol-thiol cocktail (PEG-SH, MW = 5kD, Nektar) for two additional hours under refrigeration. Unbound antibodies were then removed by centrifugation and the immunotargeted nanoshells were then resuspended in
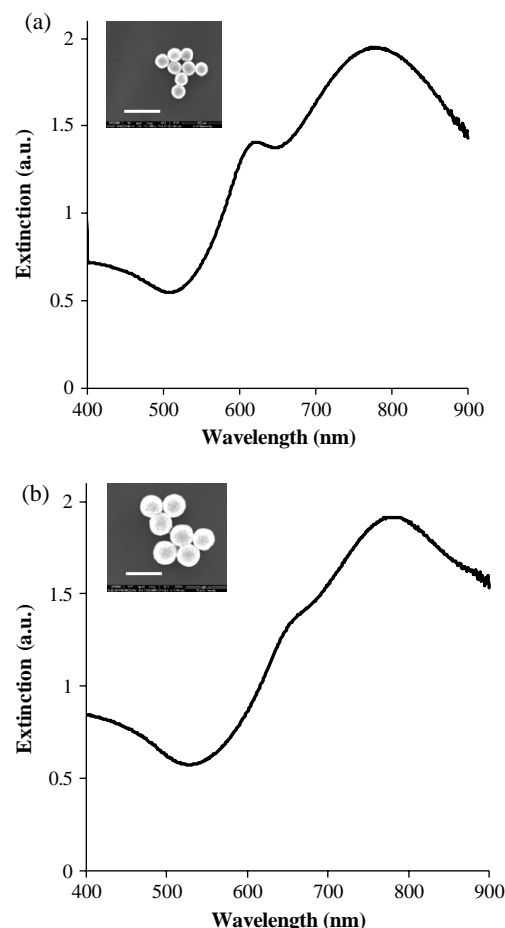

Figure 2. Measured extinction spectra of nanoshells. (a) Nanoshells of average core diameter 130 nm and average shell thickness of 21 nm. (b) Nanoshells of average core diameter 254 nm and average shell thickness of 19 nm. The insets depict corresponding images from scanning electron microscopy. Scale bars represent 450 nm.

deionized water. Prior to incubation with cells, the immunotargeted nanoshell solution was further modified by the addition of bovine serum albumin (BSA) and phosphate-buffered saline (PBS) to a final concentration of 1% each.

2.4. Cell preparation

SK-BR-3 cells (American Type Culture Collection, ATCC) were grown at 37 °C in a 5% CO_2 atmosphere using McCoy's 5A growth medium supplemented with 1% antibiotics and 10% fetal bovine serum (FBS). MCF10A cells (ATCC) were also grown at 37 °C in a 5% CO_2 atmosphere using Mammary Epithelial Basal Medium (MEBM) supplemented with a BulletKit (Clonetics) and 1% antibiotics. Both cell lines were grown in 25 cm^2 culture flasks until confluent, rinsed once with 1 × PBS, and incubated with trypsin-EDTA for 5 min at 37 °C in a 5% CO_2 atmosphere. The trypsin-EDTA was then neutralized with the appropriate culture medium and the cells were subsequently counted using a hemacytometer. For each cell line, an estimated 6×10^5 cells were placed in each of two 15 ml conical tubes and then centrifuged at 115 × *g* for 3 min. One cell pellet was resuspended in the immunotargeted
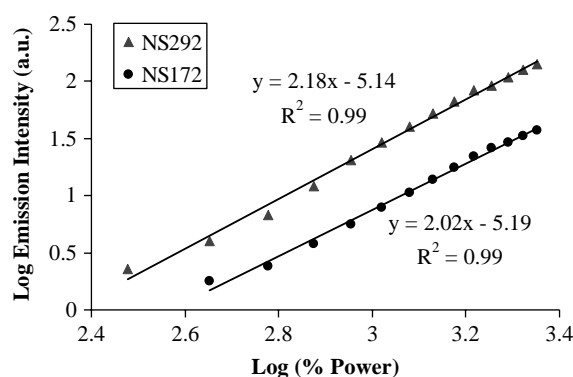
Figure 3. Quadratic dependence of luminescence intensity on excitation power at 780 nm for two different-sized nanoshells. Nanoshells of core diameter of 130 nm and shell thickness of 21 nm are designated as NS172. Nanoshells of core diameter of 254 nm and shell thickness of 19 nm are designated as NS292. Data were recorded with a 20× objective.

nanoshell solution and the other pellet was resuspended in an equal volume of 1 × PBS. The cells were then incubated at 37 °C in a hybridization chamber (VWR International) and rotated under a motor speed of 7 rpm for 10 min. Post incubation, the cells were centrifuged at 115 × *g* for 3 min, the supernatant was removed, and the cells were rinsed once with 1 × PBS. Following rinsing, the cells were resuspended in 10% glucose in 1 × PBS in order to maintain cell viability during imaging. The cell suspensions were then placed on chambered coverglasses (Fisher Scientific) prior to two-photon imaging.

3. Results and discussion

By manipulation of the core-to-shell ratio, nanoshells can be designed to strongly absorb or scatter light upon near-infrared excitation. In order to validate the two-photon characteristics of silica-based gold nanoshells, we designed two different sizes of nanoshell with a similar peak surface plasmon resonance in the near-infrared. After fabrication of two different-sized silica cores, their average diameters were confirmed through scanning electron microscopy (SEM) as 130 and 254 nm. Once the gold shell was added, the nanoshells were measured by SEM and their optical properties were assessed by UV–vis spectroscopy. The smaller nanoshells had an average diameter of 172 nm and a peak surface plasmon resonance at 772 nm; for the larger nanoshells, the average diameter was 292 nm, with a peak surface plasmon resonance occurring at 778 nm (both shown in figure 2). The two-photon luminescence properties of the gold nanoshells were then observed using a Zeiss LSM 510 META multi-photon system with the configuration shown in figure 1. The two-photon properties were verified by evaluating the dependence of increasing logarithmic emission intensity on increasing logarithmic excitation power. Aliquots of both sizes of bare nanoshell suspended in deionized water were well dispersed with sonication and separately placed on chambered coverglasses (Fisher Scientific). Data were recorded at an excitation wavelength of 780 nm, which corresponded to the peak plasmon resonance of the nanoshells for both sample

sizes. The excitation power was varied from 2% to 15% of the maximum laser power with a detection spectral band of 494–634 nm. By using the image processing software inherent in the LSM 510 META system, the average intensities of the nanoshell suspensions were obtained. The dependence of luminescence intensity on excitation power at 780 nm for both smaller- and larger-sized nanoshells was determined (figure 3). The slopes of the fitted linear curves are estimated as 2.02 and 2.18 for the smaller and larger nanoshells, respectively, in accordance with the characteristic two-photon-induced quadratic dependence of emission intensity on excitation power [14, 16, 20]. Specifically, Wang *et al* demonstrated that the dependence of luminescence intensity on excitation power for gold nanorods ranged from 1.97 to 2.17 [27]. This disparity was attributed to possible nanoparticle melting after increasing the power on the nanorod sample and, subsequently, decreasing the power on the same sample. However, in our study, since a difference in quadratic dependence exists for two sizes of gold nanoshell treated under the same conditions, we believe that the nanoshells may actually undergo photophysics which are not yet fully elucidated.

In order to demonstrate the enhanced two-photon optical signatures of breast cancer cells labeled with immunotargeted nanoshells, the HER2-overexpressing epithelial breast cancer cell line, SK-BR-3, was analyzed and compared to the normal breast epithelial cell line, MCF10A, which does not overexpress HER2. For this component of the study, the cells were incubated with the larger nanoshells which were conjugated to anti-HER2 antibodies. Images were taken of the SK-BR-3 cancer cells under three conditions: labeled with nanoshells at 10% of maximum laser power, unlabeled at 10% of maximum laser power, and unlabeled at 100% of maximum laser power. An excitation wavelength of 780 nm was used for all images and five different emission wavelength ranges were analyzed: 451–483, 483–515, 515–547, 558–579, and 590–644 nm. Additionally, images were taken of the MCF10A normal cells under the same labeling and imaging conditions. As shown in figure 4(a), bright two-photon luminescence signals from nanoshells targeted to cell surface receptors provided clear visualization of the SK-BR-3 cancer cells under only 10% of maximum laser power. However, under the same power, unlabeled cancer cells were not perceivable (data not shown due to lack of detectable signal). By increasing the laser power to 100%, the spectral-resolved two-photon-induced autofluorescence is evident at emission wavelengths ranging from 451 to 547 nm (figure 4(b)). However, this autofluorescence, which is only visible at the maximized power, cannot be discerned beyond an emission wavelength of 547 nm. With regard to the normal MCF10A cells labeled with immunotargeted nanoshells under 10% of maximum laser power, clear visualization of the cells is not possible and only a few targeted cell surface receptors can be distinguished (figure 4(c)). Due to the differences in HER2 cell surface receptor expression, which is approximately 8×10^5 receptors per SK-BR-3 cancer cell [33] and about 1×10^4 receptors per normal MCF10A cell [34], the contrast was dramatically increased in the cancer cells due to the overexpression of HER2. Similar to the unlabeled
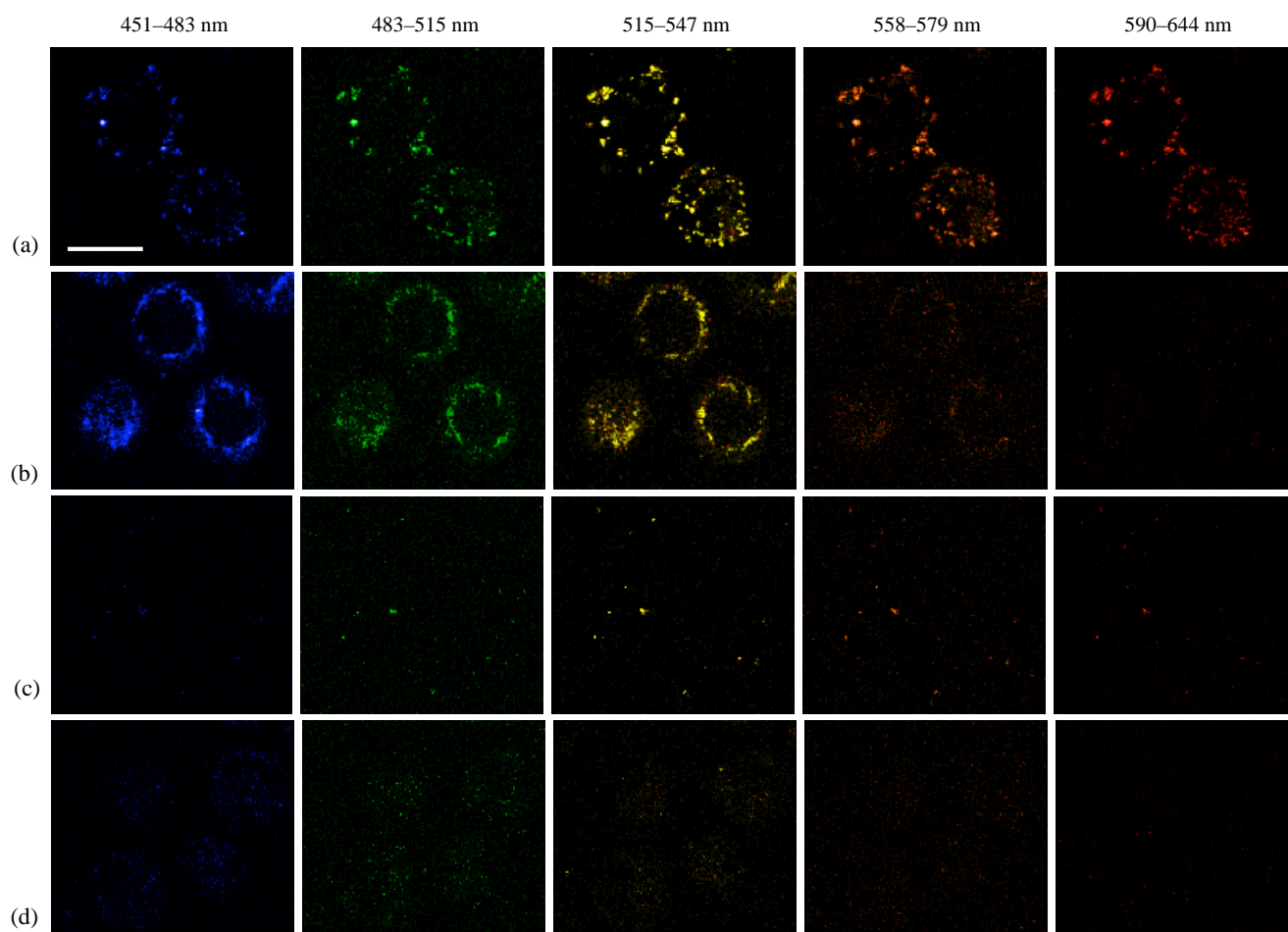
| 451–483 nm | 483–515 nm | 515–547 nm | 558–579 nm | 590–644 nm |

Figure 4. Two-photon images (pseudo color) of live SK-BR-3 cancer cells and MCF10A normal cells in suspension taken at different emission wavelengths. (a) Cancer cells labeled with larger nanoshells at 10% of maximum excitation power. (b) Unlabeled cancer cells at 100% of maximum excitation power. (c) Normal cells labeled with larger nanoshells at 10% of maximum excitation power. (d) Unlabeled normal cells at 100% of maximum excitation power. Images taken at 63×. The scale bar represents 20 μm.

SK-BR-3 cancer cells, unlabeled MCF10A cells imaged at 10% of maximum laser power were not detectable (data not shown due to lack of detectable signal). Furthermore, images collected at 100% of maximum laser power demonstrated that the MCF10A cells exhibited low levels of two-photon-induced autofluorescence (figure 4(d)). Wang *et al* [27] and Durr *et al* [29] have previously shown two-photon imaging results using gold nanorods. However, the images collected were taken over a single emission wavelength range from 400 nm to approximately 700 nm. Based on spectral-resolved image acquisition, however, the unique widely spanning luminescence properties of gold nanoshells demonstrate great flexibility in selecting the emission wavelengths necessary to minimize the influence of background autofluorescence. Photobleaching was also not observed under the two-photon-induced nanoshell luminescence. Based on a comparison of live cell bright-field images observed before and after laser exposure, morphological changes were not detected as a result of the aforementioned laser conditions and, in particular, all cell membranes remained visible and intact.

4. Conclusion

Two-photon microscopy is a powerful tool for diagnostic research applications. With advancements in gold-based contrast agent development and flexibility in two-photon excitation wavelength selection readily achieved through tunable laser sources, the potential to use multi-photon imaging for assessment of molecular signatures of malignancy is substantial. In this study, we demonstrate the first use of immunotargeted gold nanoshells as *in vitro* contrast agents for biomarkers of disease using two-photon microscopy. We additionally confirm broad luminescence from gold nanoshells using multi-spectral images to visualize the optical contrast provided by anti-HER2-nanoshells targeted to live HER2-overexpressing breast cancer cells. Our study identifies an additional application of immunotargeted nanoshells and suggests their potential future use as multi-functional probes for molecular imaging.

References

[1] Hawk E, Viner J L and Lawrence J A 2000 *Curr. Oncol. Rep.* **2** 242–50

[2] Weinberg R A 2007 *The Biology of CANCER* (New York: Taylor and Francis) pp 727–32

[3] Loo C, Hirsch L, Lee M H, Chang E, West J, Halas N and Drezek R 2005 *Opt. Lett.* **30** 1012–4

[4] Lowery A R, Gobin A M, Day E S, Halas N J and West J L 2006 *Int. J. Nanomed.* **1** 149–54

[5] Loo C, Lowery A, Halas N, West J and Drezek R 2005 *Nano Lett.* **5** 709–11

[6] Fu K, Sun J, Bickford L R, Lin A W H, Halas N J, Yu T K and Drezek R A 2008 *Nanotechnology* **19** 045103

[7] Hirsh L R, Gobin A M, Lowery A R, Tam F, Drezek R A, Halas N J and West J L 2006 *Ann. Biomed. Eng.* **34** 15–22

[8] Gobin A M, Lee M H, Halas N J, James W D, Drezek R A and West J L 2007 *Nano Lett.* **7** 1929–34

[9] Wu C, Liang X and Jiang H 2005 *Opt. Commun.* **253** 214–21

[10] Zaman R T *et al* 2007 *IEEE J. Sel. Top Quantum Electron.* **13** 1715–20

[11] Fournelle M, Maass K, Fonfara H, Welsch H J, Hewener H, Günther C and Lemor R 2007 *IEEE Ultrason. Symp.* **1051-0117/07** 2417–20

[12] Agrawal A, Huang S, Lin A W H, Lee M H, Barton J, Drezek R A and Pfefer T J 2006 *J. Biomed. Opt.* **11** 041121

[13] Loo C 2006 *PhD Thesis* Rice University, Houston, Texas

[14] Park J *et al* 2008 *Opt. Express* **16** 1590–9

[15] Wang Y, Xie X, Wang X, Ku G, Gill K L, O'Neal D P, Stoica G and Wang L 2004 *Nano Lett.* **4** 1689–92

[16] Zipfel W R, Williams R M and Webb W W 2003 *Nat. Biotechnol.* **21** 1369–77

[17] Denk W, Strickler J H and Webb W W 1990 *Science* **248** 73–6

[18] Hell S W, Booth M, Wilms S, Schnetter C M, Kirsch A K, Arndt-Jovin D J and Jovin T M 1998 *Opt. Lett.* **23** 1238–40

[19] Lewis M K, Wolanin P, Gafni A and Steel D G 1998 *Opt. Lett.* **23** 1111–3

[20] Piston D W 1999 *Cell Biol.* **9** 66–9

[21] Boyd G T, Yu Z H and Shen Y R 1986 *Phys. Rev.* B **33** 7923–36

[22] Mooradian A 1969 *Phys. Rev. Lett.* **22** 185–7

[23] Huang X, Qian W, El-Sayed I H and El-Sayed M A 2007 *Lasers Surg. Med.* **39** 747–53

[24] Nagesha D, Laevsky G S, Lampton P, Banyal R, Warner C, DiMarzio C and Sridhar S 2007 *Int. J. Nanomed.* **2** 813–9

[25] Bouhelier A, Bachelot R, Lerondel G, Kostcheev S, Royer P and Wiederrecht G P 2005 *Phys. Rev. Lett.* **95** 267405

[26] Imura K, Nagahara T and Okamoto H 2005 *J. Phys. Chem.* B **109** 13214–20

[27] Wang H, Huff T B, Zweifel D A, He W, Low P S, Wei A and Cheng J X 2005 *Proc. Natl Acad. Sci.* **102** 15752–6

[28] Huff T B, Hansen M N, Zhao Y, Cheng J X and Wei A 2007 *Langmuir* **23** 1596–9

[29] Durr N J, Larson T, Smith D K, Korgel B A, Sokolov K and Ben-Yakar A 2007 *Nano Lett.* **7** 941–5

[30] National Comprehensive Cancer Network 2007 *Breast Cancer Treatment Guidelines for Patients* Version IX http://www.nccn.org

[31] Stöber W, Fink A and Bohn E 1968 *J. Colloid Interface Sci.* **26** 62–9

[32] Duff D G, Baiker A and Edwards P P 1993 *Langmuir* **9** 2301–9

[33] Hayes D F, Walker T M, Singh B, Vitetta E S, Uhr J W, Gross S, Rao C, Doyle G V and Terstappen L W M M 2002 *Int. J. Oncol.* **21** 1111–7

[34] Kornilova E S, Taverna D, Hoeck W and Hynes N E 1992 *Oncogene* **7** 511–9

Measurement of immunotargeted plasmonic nanoparticles' cellular binding: a key factor in optimizing diagnostic efficacy

Kun Fu[1,3]**, Jiantang Sun**[1]**, Lissett R Bickford**[1]**, Alex W H Lin**[1]**, Naomi J Halas**[2]**, Tse-Kuan Yu**[3] **and Rebekah A Drezek**[1,2,4]

[1] Department of Bioengineering, Rice University, 6100 Main Street, MS-142, Houston, TX 77005, USA

[2] Department of Electrical and Computer Engineering, Rice University, 6100 Main Street, MS-142, Houston, TX 77005, USA

[3] Department of Radiation Oncology, University of Texas, M D Anderson Cancer Center, Box 1202, 1515 Holcombe Boulevard, Houston, TX 77030, USA

E-mail: drezek@rice.edu

Abstract

In this study, we use polarized light scattering to study immunotargeted plasmonic nanoparticles which bind to live SK-BR-3 human breast carcinoma cells. Gold nanoparticles can be conjugated to various biomolecules in order to target specific molecular signatures of disease. This specific targeting provides enhanced contrast in scattering-based optical imaging techniques. While there are papers which report the number of antibodies that bind per nanoparticle, there are almost no reports of the key factor which influences diagnostic or therapeutic efficacy using nanoparticles: the number of targeted nanoparticles that bind per cell. To achieve this goal, we have developed a 'negative' method of determining the binding concentration of those antibody/nanoparticle bioconjugates which are targeted specifically to breast cancer cells. Unlike previously reported methods, we collected unbound nanoparticle bioconjugates and measured the light scattering from dilute solutions of these particles so that quantitative binding information can be obtained. By following this process, the interaction effects of adjacent bound nanoparticles on the cell membrane can be avoided simply by measuring the light scattering from the unbound nanoparticles. Specifically, using nanoshells of two different sizes, we compared the binding concentrations of anti-HER2/nanoshell and anti-IgG/nanoshell bioconjugates targeted to HER2-positive SK-BR-3 breast cancer cells. The results indicate that, for anti-HER2/nanoshell bioconjugates, there are approximately 800–1600 nanoshells bound per cell; for anti-IgG/nanoshell bioconjugates, the binding concentration is significantly lower at nearly 100 nanoshells bound per cell. These results are also supported by dark-field microscopy images of the cells labeled with anti-HER2/nanoshell and anti-IgG/nanoshell bioconjugates.

1. Introduction

Scattering-based optical imaging techniques offer a new approach to noninvasive cancer diagnosis [1–3]. Targeted optical contrast agents are playing an increasingly significant role in these scattering-based techniques by enabling enhanced molecular-specific optical signals. In particular, gold nanoparticles are attractive for potential *in vivo* applications due to gold's inherent biocompatibility and

[4] Author to whom any correspondence should be addressed.

because the gold surface can be readily modified with various molecules. Numerous gold nanomaterials have been investigated as possible optical contrast agents, including colloidal gold nanoparticles [4–6], gold nanoshells [7–11], gold nanorods [12–14] and gold nanocages [15]. As an optical contrast agent for cancer imaging applications, gold nanoshells have shown considerable potential. This potential arises due to the optical tunability of nanoshells from the visible light spectrum through the near-infrared (NIR) region [16].

Previous studies have shown that colloidal gold nanoparticles which have been conjugated with anti-EGFR monoclonal antibodies provide enhanced signals in labeled human cervical tumor cancer (SiHa) cells, as shown in confocal reflectance images [4, 5]. Similar results, when using dark-field microscopy, have also been seen in anti-EGFR/gold nanoparticles' labeled HSC oral cancer cells [6]. Proof-of-concept studies show that gold nanoshells conjugated with anti-HER2 antibodies provide enhanced signals, specifically in labeled HER2-positive human breast cancer SK-BR-3 cells. These have been observed in reflectance confocal and dark-field microscopy images [8, 9]. Given the diagnostic potential of various nanoparticles and their *in vivo* applications, the ability to quantify nanoparticle bioconjugates that can be targeted to cancer cells is significant and critical for improved diagnostic and therapeutic results. Despite this potential, however, the key factor which influences diagnostic or therapeutic efficacy is not even reported: the number of targeted nanoparticles that bind per cell. Thus far in the literature, only Sokolov *et al* have reported $\sim 5 \times 10^4$ nanoparticle bioconjugates bound per cell for human cervical tumor (SiHa) cells labeled with anti-EGFR monoclonal antibodies–conjugated colloidal gold nanoparticles [4]. The method they used to acquire the binding number requires centrifugation of the mixture of labeled cells and nanoparticles, so that those nanoparticles which did not bind to the cell surfaces are separated out. This method may be limited by the size of the nanoparticles and the material from which they are made, i.e. it may not be effective to separate cells and nanoparticles of all varieties by centrifugation. Other people attempted to study the binding efficiency by using the direct measurement of optical signals from nanoparticles which were bound to cells. The limitation of this method is that multiple scattering can occur when nanoparticles are in close proximity to each other on the cell membrane. Due to the nonlinear effect introduced by this multiple scattering, the nanoparticle binding information cannot be accurately assessed. Additionally, measuring the optical signals of nanoparticles which bind to cells does not provide the quantitative information of the binding numbers. It is also difficult to directly count the number of particles that bind to cells. To achieve the binding information effectively and accurately, we have developed a novel method to semi-quantitatively characterize the binding concentration of gold nanoparticle bioconjugate-labeled HER2-positive SK-BR-3 breast cancer cells using polarized angular-dependent light scattering. We have called this method 'negative' quantification because we first obtain concentration information and light scattering spectra from nanoparticles that were originally added to the cells for incubation. We then collect unbound nanoparticles after the incubation period with the cells, and

measure the light scattering of these unbound nanoparticles. According to Mie theory, when a single-scattering criterion is satisfied, the intensity of scattered light is linearly proportional to the particle concentration [17, 18]. Under laboratory conditions, a simple way to demonstrate that single-scattering events predominate in a scattering media is to dilute the concentration of particles in the sample by a chosen factor and observe whether the scattered light intensities at all scattering angles also drop by this same factor. If this is true, single scattering predominates in this sample. Therefore, under single-scattering conditions, by comparing the light scattering spectra of the original and the unbound nanoparticles, the concentration of the unbound nanoparticles can effectively be obtained. Combined with cell counting data, the average number of nanoparticles bound per cell can be derived. By following this procedure, cells labeled with immunotargeted nanoparticles can be effectively separated from unbound nanoparticles, as will be discussed later in this paper. Furthermore, multiple light scattering, which may influence the accuracy in deriving the concentration of nanoparticles, can also be avoided simply by measuring light scattering from a diluted suspension of unbound nanoparticles.

2. Method

2.1. Gold–silica nanoshell fabrication

Detailed description of the fabrication of gold–silica nanoshells can be found in [19]. Generally, spherical SiO_2 nanoparticles are synthesized using the Stöber method [20] and functionalized by immersing and boiling the SiO_2 nanoparticles with aminopropyl-triethoxysilane (APTES). Gold colloid is prepared as reported by Duff *et al* [21]. The functionalized silica cores are then seeded with concentrated gold colloid, which adsorbs onto the amine groups on the silica surface, to facilitate the growth of the gold shell. Next, nanoshells are grown by mixing a stock solution of $HAuCl_4$ with the seed particles under formaldehyde catalysis. During this process, gold is reduced onto the adsorbed gold colloid on the seed particle and will eventually form a continuous shell over the SiO_2 core. The growth of nanoshells is monitored using a UV–vis spectrophotometer (Varian Cary 300) and also by comparing the measured extinction spectra with the calculations from Mie theory; the particle size is further confirmed by using a scanning electron microscope (SEM). Mie theory is used to determine the absorption, as well as scattering and extinction coefficients, of nanoshells with a specific core radius and shell thickness. The concentration of the nanoshells can then be determined by relating the calculated extinction coefficient to the measured extinction from the spectrophotometer. Figure 1 shows the SEM images and the measured extinction spectra of nanoshells used in this study. In this paper, we refer to the size of a gold nanoshell by the notation R r_1/r_2 nm, where r_1 is the core radius in nanometers (nm) and r_2 is the overall particle radius in nanometers (nm). Then $(r_2 - r_1)$ is the thickness of the gold shell. Two different sized nanoshells are used in this study. According to Mie theory calculations and SEM images, the smaller nanoshell is $r_1 = 86 \pm 7$ nm and $r_2 = 111 \pm 10$ nm, which is shown as $R86 \pm 7/111 \pm 10$ nm; while the larger one
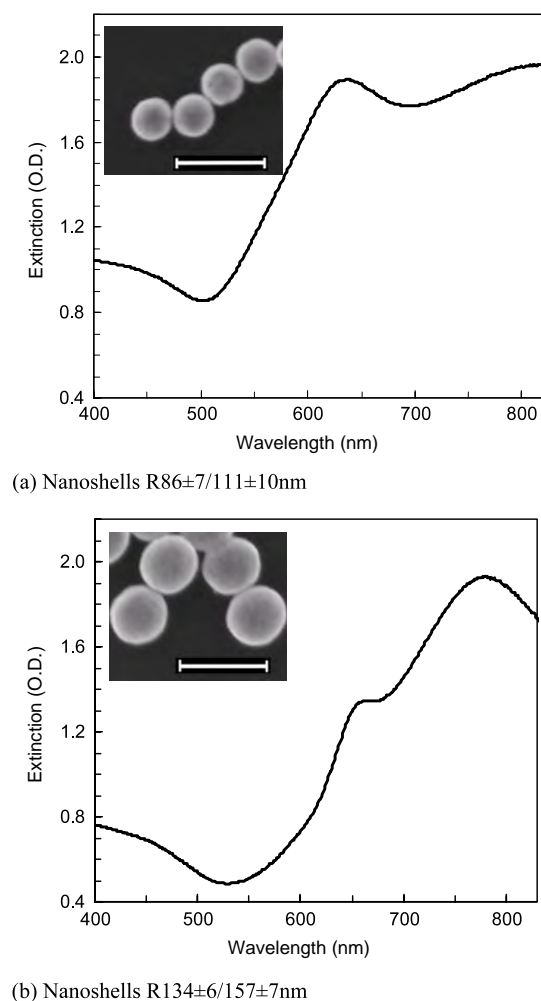
(a) Nanoshells R86±7/111±10nm

(b) Nanoshells R134±6/157±7nm

Figure 1. Measured extinction spectra of gold nanoshells. SEM images of the gold nanoshell are taken at $50\,000\times$ and the scale bar is 500 nm. (a) Nanoshells $R86 \pm 7/111 \pm 10$ nm. (b) Nanoshells $R134 \pm 6/157 \pm 7$ nm.

is $r_1 = 134 \pm 6$ nm and $r_2 = 157 \pm 7$ nm, which is displayed as $R134 \pm 6/157 \pm 7$ nm.

2.2. Preparation of OPSS-PEG-antibodies

Anti-HER2 (Labvision) or anti-IgG (Sigma) antibodies were tethered to nanoshell surfaces using bifunctional PEG linkers. Orthopyridyl disulfide-PEG-*n*-hydroxysuccinimide (MW 2000, OPSS-PEG-NHS, Shearwater Polymers, Nektar) was allowed to react with each antibody at 1:1 molar ratio in 100 mM sodium bicarbonate (pH 8.5) for 4–8 h, or overnight, on ice. The product was then dialyzed in 100 mM sodium bicarbonate for 2 h using a dialysis cassette with a molecular weight cutoff of 5000, to remove excess reagent. The product was then stored in frozen working aliquots at $-20\,^{\circ}$C [22, 23].

2.3. Nanoshell bioconjugation

The anti-HER2 (anti-IgG)/nanoshell conjugates were obtained by reacting the OPSS-PEG-antibodies with the nanoshells for 1 h at $4\,^{\circ}$C. Additional nonspecific adsorption sites on
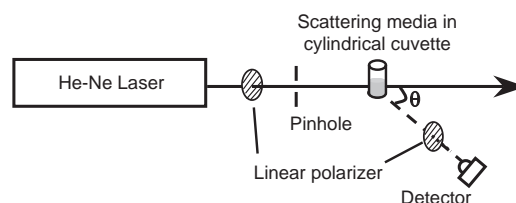

Figure 2. Schematic of experimental set-up of the goniometer for the angular-dependent light scattering study. The light from a 633 nm He–Ne laser is incident through the first polarizer onto a cylindrical cuvette containing the samples; the scattered light is then collected by a silicon detector rotating around the cuvette through the second polarizer.

the nanoshell surfaces were then blocked by reacting with PEG-SH (MW 5000) for an additional hour. The nanoshell bioconjugates were subsequently centrifuged so that excess reagent was removed. The nanoshell bioconjugates were then resuspended in phosphate buffered saline (PBS) to prepare for cell targeting. Concentration of nanoshell bioconjugates was determined to be $\sim$1–1.5 $\times$ 10^9 particles ml^{-1}, with peak optical density of the extinction spectra at around 2, depending on the size of the particle.

2.4. Cell culture and incubation with anti-HER2 (anti-IgG)/gold nanoshell bioconjugates of SK-BR-3 breast cancer cells

HER2-positive human breast epithelial carcinoma SK-BR-3 cells (ATCC) were cultured in McCoy 5A growth medium containing 10% fetal bovine serum (FBS) and 1% antibiotics at $37\,^{\circ}$C and 5% CO$_2$. The cells were grown in 25 cm^2 cell culture flasks to a concentration of $\sim$5–8 $\times$ 10^4 cells cm^{-2}. Following three washes with PBS, anti-HER2 (anti-IgG)/nanoshell bioconjugates suspended in PBS were added to the cell culture flask together with 1% Bovine Serum Albumin (BSA) as a blocker to eliminate nonspecific interactions. The cells were then incubated with the nanoshell bioconjugates for one hour. After incubation, additional unbound nanoshell conjugates were collected using a pipette. The cells were then rinsed with PBS three times to ensure that all the unbound nanoshells were removed and collected. The rinsing PBS and unbound nanoshells were collected for light scattering measurements. Finally, the labeled cells were removed from the cell culture flask using trypsin-EDTA and resuspended in McCoy 5A growth medium for dark-field imaging and cell counting.

2.5. Polarized angular-dependent light scattering measurement

A schematic of the experimental set-up for the light scattering study is shown in figure 2, and details about it can be found in our previous publication [24]. The polarized angular-dependent light scattering spectra of gold nanoshell bioconjugates were studied using an automated goniometer. Light scattering has been shown to be sensitive to both the size and concentration of small particles. Furthermore, it has been proven that light scattering from surface-modified
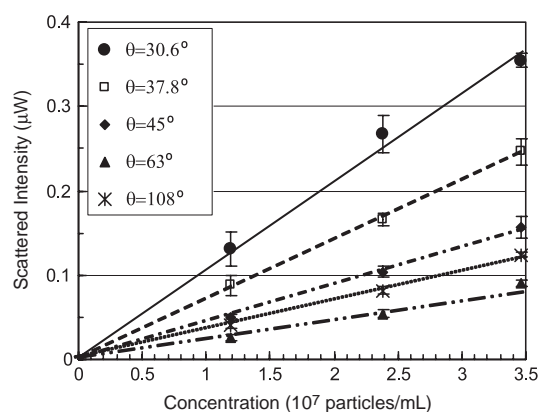
Figure 3. Scattered light intensity at different scattering angles showing a linear relationship between the light scattering signal and the concentration for nanoshell $R86 \pm 7/111 \pm 10$ nm. Error bars represent the standard deviation of three separate measurements.

nanoparticles can also be predicted by Mie theory [24–26]. Therefore, the concentration of gold nanoshell bioconjugates can be reliably derived from the light scattering phase function that we measured. We additionally conclude, for the aforementioned reasons, that the goniometer has effectively facilitated our semi-quantitative study and can thus be considered a promising tool with which to characterize the binding concentration of gold nanoshell bioconjugates to SK-BR-3 cells.

3. Results and discussion

To accomplish our goal of characterizing the number of nanoshells bound on each cancer cell, nanoshell bioconjugates with different concentrations were first prepared, and light scattering from these initial samples was compared. The light scattering study showed a significant linear relationship with the concentration for these samples, as shown in figure 3. This confirms the feasibility of using light scattering to characterize the concentration of unknown nanoshell bioconjugates. One of these diluted nanoshell samples, with known concentration, was then recorded as a standard reference, as shown in figures 4(a) and (b) (black solid curves). After cell targeting, the unbound nanoshell bioconjugates were collected and diluted for light scattering measurements. Once the polarized light scattering of both the unbound and reference nanoshell bioconjugates was obtained, the concentration of the unbound nanoshells could be derived by interpolating the scattered intensity between the lines in figure 3. Specifically, the total number of nanoshells bound to the cell could then be calculated using the volume and concentration data of the unbound nanoshells and the nanoshells originally added to the SK-BR-3 cells. After counting the cells, the number of nanoshells bound per cell could be determined, thus confirming the validity of our 'negative' approach, as referenced above. Figure 4 shows the parallel polarized light scattering from the reference and unbound gold nanoshells (anti-HER2 conjugated only) of different sizes. The number of anti-HER2 (anti-IgG)/nanoshells bound per cell is shown in table 1. The
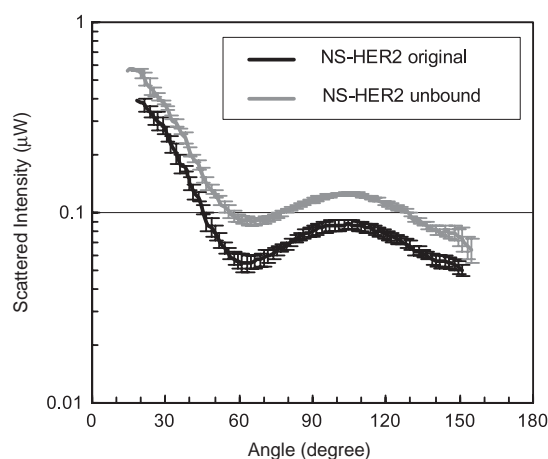
(a) Nanoshells R86±7/111±10nm
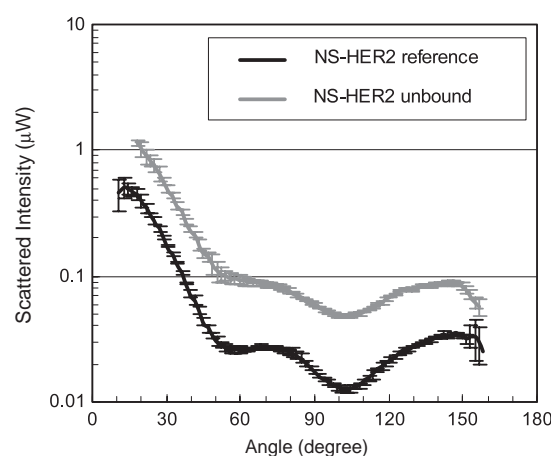
(b) Nanoshells R134±6/157±7nm

Figure 4. Parallel polarized angular-dependent light scattering measurements of reference and unbound anti-HER2/nanoshell bioconjugates: the concentration of unbound nanoshells can be derived by comparing the light scattering to that of the reference nanoshells. (a) NS $86 \pm 7/111 \pm 10$ nm. (b) NS $134 \pm 6/157 \pm 7$ nm. Error bars represent the standard deviation of three separate measurements for each sample.

errors in table 1 represent the standard deviations of three separate measurements which come from the summation of the individual errors generated in the light scattering measurements and from cell counting. This data is also supported by the results from a previous study on the use of gold nanoshells for molecular imaging [8]. In that study, Loo and colleagues used nanoshells of $R120/155$ nm for cell labeling, and compared the intensity of dark-field microscopy images taken from different nanoshell-labeled configurations. The author's histogram analysis of the resulting dark-field images shows that nanoshell targeting of the HER2 receptor resulted in significantly greater average contrast values in the anti-HER2 group (142 ± 16) compared with the anti-IgG group (48 ± 12) and with the group lacking nanoshells (26 ± 4) [8]. These results show an average of 5 times greater efficiency in anti-HER2 targeting than in anti-IgG targeting. This reinforces our semi-quantitative results of using the $R134 \pm 6/157 \pm$
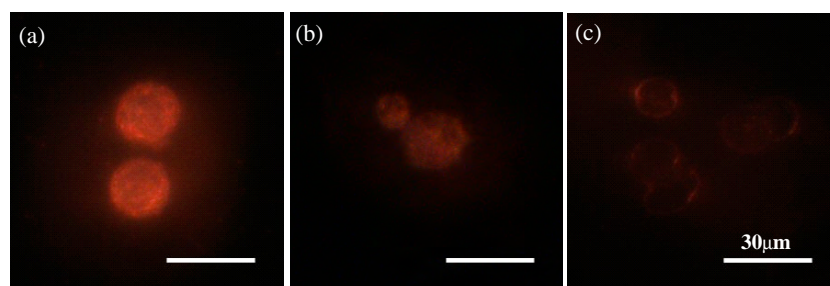
Figure 5. Dark-field microscopy images of SK-BR-3 cells with (a) anti-HER2/nanoshell targeting ($R86 \pm 7/111 \pm 10$ nm, specific), (b) anti-IgG/nanoshell targeting ($R86 \pm 7/111 \pm 10$ nm, nonspecific) and (c) without targeting. All images were taken under the same lighting conditions.
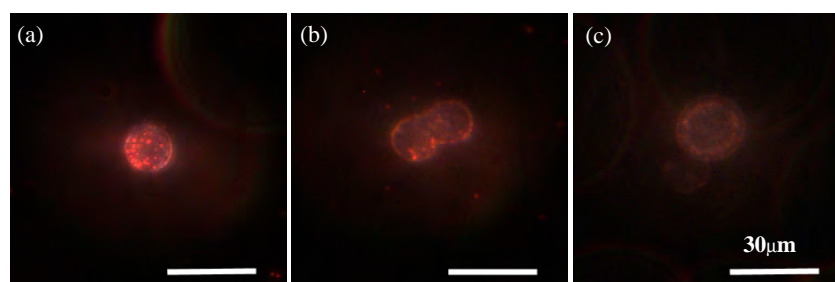

Figure 6. Dark-field microscopy images of SK-BR-3 cells with (a) anti-HER2/nanoshell targeting ($R134 \pm 6/157 \pm 7$ nm, specific), (b) anti-IgG/nanoshell targeting ($R134 \pm 6/157 \pm 7$ nm, nonspecific) and (c) without targeting. All images were taken under the same lighting conditions.

Table 1. Number of nanoshell bioconjugates bound per cell.

No. of nanoshells per cell	NS $R86 \pm 7/111 \pm 10$ nm	NS $R134 \pm 6/157 \pm 7$ nm
Anti-HER2/NS	1503 ± 204	883 ± 101
Anti-IgG/NS	90 ± 11	113 ± 16

7 nm nanoshells (which are similar in size as reported in [8]) to increase the nanoshell binding efficiency with anti-HER2 targeting. We have found that the anti-HER2 targeting is of the order of 5–9 times more efficient than the anti-IgG targeting for these specific nanoshells, as shown in table 1.

Images of anti-HER2 (anti-IgG)/gold nanoshell bioconjugate-targeted SK-BR-3 breast cancer cells were taken under dark-field microscopy, a type of imaging modality that is only sensitive to the scattered light of visualized objects. This makes dark-field microscopy very suitable for the imaging of biological cells and small particles, as well as for nanoparticle-labeled cells. Images were taken with a Zeiss Axioskop 2 Plus microscope equipped with a color CCD camera using a $40\times$ objective. All images were taken using the same lighting conditions; more specifically, all same-sized nanoshell labeling had images taken under the same conditions. Figures 5 and 6 show the dark-field microscopy images of SK-BR-3 breast cancer cells labeled with anti-HER2 (anti-IgG)/gold nanoshell bioconjugates, as well as SK-BR-3 cells without any labeling. Based on the dark-field images, we can clearly see the difference in both specific (anti-HER2/gold nanoshell) and nonspecific (anti-IgG/gold nanoshell) labeled cells, compared to those cells without any nanoshell labeling. The cells with specific labeling demonstrate greater contrast under dark-field microscopy, due to the increase in targeted nanoshells [8]. This also supports our results on the number of nanoshell bioconjugates bound per cell as shown in table 1.

4. Conclusion

In conclusion, we have developed a new technique to semi-quantitatively characterize the binding concentration of nanoparticles to living cancer cells. We have labeled HER2-positive SK-BR-3 human breast cancer cells with gold nanoshells of different sizes, and semi-quantitatively compared the differences in anti-HER2 and anti-IgG conjugated nanoshell labeling. We have provided an easy and reliable method for semi-quantitatively determining the amount of immunotargeted nanoparticles that can be targeted to SK-BR-3 breast cancer cells. Unlike the previous methods which measure cells labeled with nanoparticles, this method only requires the measurement of scattered light from nanoshell bioconjugates and provides accurate information on the number of nanoparticles that actually bind on the cell surfaces. Following this method, multiple scattering effects can be avoided simply by measuring light scattering from the dilute suspension of unbound nanoshells. This study provides important information on characterizing cell labeling with immunotargeted plasmonic nanoparticles for diagnosis and therapeutic applications. As a generalized methodology, it can also be easily applied to studies of other scattering nanoparticles targeted to cells that overexpress other biomarkers.

Acknowledgments

References

[1] Fujimoto J G 2003 *Nat. Biotechnol.* **21** 1361–7
[2] Lee T M, Oldenburg A L, Sitafalwalla S, Marks D L, Luo W, Toublan F J-J, Suslick K S and Boppart S A 2003 *Opt. Lett.* **28** 1546–8
[3] Palmer G M, Zhu C, Breslin T M, Xu F, Gilchrist K W and Ramanujam N 2003 *IEEE Trans. Biomed. Eng.* **50** 1233–42
[4] Sokolov K, Follen M, Aaron J, Pavlova I, Malpica A, Lotan R and Richartz-Kortum R 2003 *Cancer Res.* **63** 1999–2004
[5] Sokolov K *et al* 2003 *Technol. Cancer Res. Treatment* **2** 491–504
[6] El-Sayed I H, Huang X and El-Sayed M A 2005 *Nano Lett.* **5** 829–34
[7] Loo C, Lin A, Hirsch L, Lee M-H, Barton J, Halas N, West J and Drezek R 2004 *Technol. Cancer Res. Treatment* **3** 33–40
[8] Loo C, Hirsch L R, Lee M-H, Chang E, West J, Halas N and Drezek R 2005 *Opt. Lett.* **30** 1012–4
[9] Loo C, Lowery A, Halas N, West J and Drezek R 2005 *Nano Lett.* **5** 709–11
[10] Jackson J B, Westcott S L, Hirsch L R, West J L and Halas N J 2003 *Appl. Phys. Lett.* **82** 257–9
[11] Jackson J B and Halas N J 2004 *Proc. Natl Acad. Sci. USA* **101** 17930–5
[12] Huang X, El-Sayed I H, Qian W and El-Sayed M A 2006 *J. Am. Chem. Soc.* **128** 2115–20
[13] Stone J W, Sisco P N, Goldsmith E C, Baxter S C and Murphy C J 2007 *Nano Lett.* **7** 116–9
[14] Orendorff C J, Baxter S C, Goldsmith E C and Murphy C J 2005 *Nanotechnology* **16** 2601–5
[15] Chen J *et al* 2005 *Nano Lett.* **5** 473–7
[16] Weissleder R 2001 *Nat. Biotechnol.* **19** 316–7
[17] van de Hulst H C 1981 *Light Scattering by Small Particles* (New York: Dover) pp 5–6
[18] Bohren C and Huffman D R 1983 *Absorption and Scattering of Light by Small Particles* (New York: Wiley) p 9
[19] Oldenburg S J, Averitt R D, Westcott S L and Halas N J 1998 *Chem. Phys. Lett.* **288** 243–7
[20] Stober W and Fink A 1968 *J. Colloid Interface Sci.* **26** 62–6
[21] Duff D G and Baiker A 1993 *Langmuir* **9** 2301–9
[22] Hirsch L R, Jackson J B, Lee A, Halas N J and West J L 2003 *Anal. Chem.* **75** 2377–81
[23] Hirsch L R, Halas N J and West J L 2005 *Methods Mol. Biol.* **303** 101–12
[24] Fu K, Sun J, Lin A W H, Wang H, Halas N J and Drezek R A 2007 *Curr. Nanosci.* **3** 167–70
[25] Khlebtsov N G, Bogatyrev V A, Khlebtsov B N, Dykman L A and Englebienne P 2003 *Colloid. J.* **65** 622–35
[26] Khlebtsov N G 2004 *J. Quant. Spectrosc. Radiat. Transfer* **89** 143–53